universität innsbruck

Master Thesis

Towards a Transportable Antiproton Trap for Precision Metrology with Isomeric Highly Charged Ions

Sara Alfaro Campos

September 17, 2025

Supervised by Dr. Giovanni Cerchiari
Institute for Experimental Physics

Contents

Statutory declaration

Ich erkläre hiermit an Eides statt durch meine eigenhändige Unterschrift, dass ich die vorliegende Arbeit selbständig verfasst und keine anderen als die angegebenen Quellen und Hilfsmittel verwendet habe. Alle Stellen, die wörtlich oder inhaltlich den angegebenen Quellen entnommen wurden, sind als solche kenntlich gemacht.
Ich erkläre mich mit der Archivierung der vorliegenden Masterarbeit einverstanden.

Innsbruck, am September 17, 2025 Sara Alfaro Campos

Abstract

Antimatter research probes fundamental symmetries of the Standard Model of particle physics and tests its limitations. The research field of low-energy experiments on antiprotons is limited due to the scarcity of this experimental resource. Currently, low-energy antiprotons can only be experimented with at the Antimatter Factory located at the European Organization for Nuclear Research (CERN). The Extra Low Energy Antiproton ring (ELENA) is currently the only source worldwide of antiprotons at low energies suitable for capture in charged particle traps. This thesis presents proposed strategies for producing isomeric highly charged ions (HCIs) via annihilation with low-energy antiprotons in a trap and their application to precision metrology through nuclear transition frequency measurements. A thorough analysis of candidate species for these experiments and their potential for the field of metrology is provided. Furthermore, this work presents the development, construction, and characterization of a transportable linear Paul trap for antiproton transport. Experimental results demonstrate successful ion trapping and the transport capabilities, with measured storage times and optimized trapping parameters confirming the system's functionality. The methods of synthesis, trapping, and extraction of antiprotons for loading into the transportable trap are discussed. Preliminary experimental results of low-energy antiproton extraction from the Antihydrogen Experiment: Gravity, Interferometry, Spectroscopy (AEgIS) are presented.

1. Introduction

The theoretical prediction and experimental discovery of antiprotons remains a remarkable milestone in the field of particle physics. The existence of antimatter was first theoretically proposed by physicist Paul Dirac in 1928, when trying to describe electrons traveling at relativistic speeds [1]. His proposed equation for describing the motion yielded two separate solutions for the electron's energy, one being positive and the other being a negative solution. He interpreted these results to mean that paired to the electron, there must be a particle equivalent in mass to the electron but of opposite charge. Dirac's hypothesis was later confirmed when the positron was first experimentally discovered by Carl Anderson in 1933 [2]. The theory of antimatter extends beyond the electron, with all fundamental particles having a conjugate antiparticle [3].

The lack of naturally occurring antimatter in the universe continues to puzzle physicists to this day. Theories of the early universe suggest that antimatter and matter were initially created at equal rates via pair production from high-energy photons, in a process named baryogenesis. However, observations suggest that the visible universe has a perceived excess of baryons over antibaryons. Charge parity (CP) violation has been suggested as a possible explanation for this asymmetry; however, it is only able to partially explain the total asymmetry found [4]. This ongoing puzzle has led physicists to probe the Standard Model of particle physics by experimenting with antimatter.

Experiments on antimatter are routinely performed at the European Organization for Nuclear Research (CERN). These experiments include high-energy experiments performed at the Large Hadron Collider (LHC), such as recent findings by the LHC-beauty (LHCb) collaboration, which illustrate some key asymmetries between the decay of the beauty baryon and its conjugate antibaryon, marking the first measurement of CP violation in baryon decays [5]. Antimatter experiments are also performed at low energies inside CERN's Antimatter Factory facilities. There, a network of accelerators and decelerators allows for the production of antiproton beams at energies that allow for low-energy antiproton trapping and storage [6].

Experiments at CERN's Antimatter Factory largely focus on precision measurements, such as the measurements of the antiproton's lifetime [7] and magnetic moment [8] demonstrated by the Baryon Antibaryon Symmetry Experiment (BASE). Additionally, antimatter experiments at these facilities extend from antiprotons to more complex neutral antimatter systems. For example, the Antihydrogen Laser Physics Apparatus (ALPHA) is active in precision spectroscopy and gravity on antihydrogen [9, 10], which is the simplest possible antimatter nucleus composed of an antiproton and a positron. The Atomic Spectroscopy And Collisions Using Slow Antiprotons (ASACUSA) also investigates spectroscopy on antihydrogen and of antiprotonic Helium, which is an exotic matter-antimatter atom where an antiprotons substitute an electron in the He atom (or ion) [11]. The Gravitational Behaviour of Antimatter at Rest (GBAR) experiment aims at the measurement of gravity on antimatter via the synthesis of the antihydrogen positive ion, the antimatter counterpart of the hydrogen negative ion [12]. Finally, the host of this thesis, the Antihydrogen Antimatter Experiment: gravity, Interferometry, Spectroscopy (AEgIS), is an experiment dedicated to observing the force of gravity on antihydrogen via a ballistic measurement [13]. To reach this goal, the AEgIS experiment has been very active in laser spectroscopy and laser cooling of antimatter systems with particular emphasis on the Positronium (Ps) atom [14, 15].

Positronium is the bound state of an electron and a positron, and, in AEgIS, it is a key ingredient for the pulsed synthesis of antihydrogen to initiate the ballistic measurement [16].

The limiting environment where low-energy antiproton experiments are located has motivated the effort of developing a trap capable of transporting antiprotons outside of these facilities. The BASE-STEP (STEP: Symmetry Tests in Experiments with Portable antiprotons) [17] and the PUMA (antiProton Unstable Matter Annihilation) [18] devices are two cryogenic charged particle traps currently in development at the Antimatter Factory with this goal in mind. The primary limitation that the BASE-STEP experiment aims to solve is the noise for precision experiments and for PUMA, the access to less stable matter, as they would like to transport the antiprotons to CERN's ISOLDE (Isotope Separator On Line DEvice) facility. Recent results presented by the BASE-STEP experiment showed significant progress by presenting the first transport of protons in the device [19], marking an important benchmark in the ongoing efforts of transporting antiprotons.

This thesis presents the development of a linear Paul trap intended for transporting antiprotons at room temperature. In contrast to cryogenic traps such as BASE-STEP and PUMA, the device assembled in this work offers the advantage of portability, reduced operational complexity, and lower cost. While room-temperature operation limits the number of antiprotons that can be stored and their storage time, this simpler approach offers a proof-of-principle approach to addressing the trappability of antiprotons at room temperature. By testing the annihilation cross section of antiprotons with residual gas molecules for antiproton energies in the range of $10 - 100\,\mathrm{eV}$ in the trap, this trap aims to establish a foundation for future antimatter transport experiments.

Beyond the immediate goal of antiproton transport outside of the Antimatter Factory, this work explores the broader experimental prospects of utilizing trapped low-energy antiprotons that could be transported in such a device. In particular, antiproton annihilation-induced highly charged ion (HCI) formation offers a novel pathway towards experiments of precision metrology. Reduced sensitivity to the environment and enhanced hyperfine splitting make HCIs ideal candidates for future frequency standards and fundamental physics tests. Antiproton annihilation extends the accessible range over the conventionally used methods for producing HCIs. Controlled antiproton annihilation in ion traps offers access to exotic nuclear states that couldn't be generated easily via electron-beam traps [20, 21] or that require large accelerator facilities with storage rings [22], opening the possibility of precision measurements on isomeric transitions and applications such as optical atomic clocks [23].

This thesis, therefore, pursues two complementary objectives in the study of low-energy antiprotons. Namely, the exploration of the experimental potential of antiproton annihilation-induced HCI generation for precision metrology, and the development, assembly, and characterization of a room-temperature transportable linear Paul trap for antiprotons, shown to be capable of transporting ions. Together, both results set the stage for utilizing antiprotons away from large and often electromagnetically noisy facilities, such as at CERN. Thus, opening new opportunities at metrology institutes where antiprotons could serve as a tool to synthesize HCI on demand for precision studies [24–26].

The content of this thesis is divided into four chapters. Firstly, Chapter 2.3.3 outlines the theory and motivations behind the work of this thesis. It describes the fundamental principles of ion trapping in linear Paul traps, as well as methods of ion generation and detection in them. Furthermore, it outlines the methods of low-energy antiproton generation at CERN and trapping at the AEgIS facilities and illustrates how antiproton trapping at room temperature could be achieved. Lastly, it discusses the atomic structure characteristics of HCIs that make them ideal candidates for studies in the field of metrology and precision spectroscopy, as well as methods

of HCI formation, including via antiproton annihilation. Consequently, Chapter 3 outlines the work conducted during this thesis in contribution to the research article presented in Ref. [23]. It discusses potential species to be used in HCI formation via antiproton annihilation. Here, calculations and simulations to find suitable candidates for such an experiment are presented. Chapter 4.3.2 focuses on the experimental work conducted during this thesis, from the development and design of the trap, to results on optimal trapping parameters, storage time, and ion transport. Furthermore, it discusses the strategy of extraction of antiprotons to be performed from the AEgIS experiment to the trap and reports on preliminary measurements of the operation. Lastly, Chapter 5 provides a conclusion of the achievements of this work as well as an outlook on future experiments. It describes future improvements of the work presented and strategies for its growth.

2. Low Energy Antiprotons: Synthesis, Trapping and Applications

This chapter introduces the principles and motivations underlying the work conducted in this thesis. Here, the theoretical and experimental foundations of ion trapping needed to understand this work are presented. The methods for synthesizing and storing low-energy antiprotons are presented, along with the main motivations and challenges associated with developing a transportable trap for these particles. Moreover, the concept of highly-charged ions (HCI) and their applications is introduced. A particular emphasis is placed on how antimatter research may contribute to this field through HCI formation via annihilation with trapped low-energy antiprotons.

2.1. Ion Trapping Fundamentals

Charged particle traps have gone on to become powerful techniques employed in several fields of study, ranging from isotope separation for targeted cancer therapy [27] to quantum computing with trapped ions [28]. They offer a robust and well-understood method for confining charged particles for long periods of time. Antiproton studies especially benefit from this technology, as antiprotons are highly reactive, and interaction with matter leads to their annihilation. Antiprotons thus benefit from the controlled ultra-high-vacuum environment found in particle traps, allowing for precision tests on antimatter that would otherwise not be possible, such as studies on the electronic transitions of antihydrogen [29].

The field of charged particle trapping was pioneered in the late 1950s by Wolfgang Paul and Hans Dehmelt, who went on to receive a Nobel Prize in 1989 [30] for their independent work on the Paul and Penning traps, respectively. These two developments solved the long-standing problem of charged particle confinement and storage. Both found alternative solutions to deal with Earnshaw‘s theorem, which states that a charged particle cannot be confined with exclusively static electric fields. The Penning trap makes use of both static electric and magnetic fields to circumvent this issue, while the Paul trap makes use of an oscillating electric potential [31], the latter of the two traps being the focus of this section.

The Paul trap uses an oscillating quadrupole electric field to radially confine particles towards the center of the field. This potential is mass selective, which is why the Paul trap owes its origins to its initial development as a mass spectrum analyzer [32]. Additional direct current electrodes then limit the potential trapping volume to only a small region in the trap, where the ions sit. The standard Paul trap operates three-dimensionally, with ring-shaped electrodes, confining the particles in a spheroidal cloud shape. On the other hand, in the linear Paul trap, the quadrupole oscillating potential is achieved via four rod electrodes generating the radial confinement. In addition to the direct current field, this results in a one-dimensional chain of tightly confined ions.

The linear Paul trap offers some important advantages for many applications. Of particular importance in this work, its open geometry offers greater optical access, which is useful for loading ions via laser ablation and consequently laser cooling them in the trap. In this section, the physics principles behind the linear Paul trap are presented, and the trapping parameters and voltages

are described. Additionally, the methods of ion loading via laser ablation and imaging detection via a microchannel plate detector are presented to elaborate on the ion trapping methods and detection techniques presented in this thesis.

2.1.1. Principles of the Linear Paul Trap

As stated by Earnshaw's theorem, it is not possible to trap charged particles using only static electric fields [31]. A way to go around this problem is the employment of oscillating electric fields, as is done in the linear Paul trap. In it, charged particles are trapped by a time-dependent quadrupole electric potential generated by four parallel rods, two of which are connected to a radio-frequency voltage, as shown in Fig. 2.1. This quadrupole potential confines the particles radially, along xy-plane. An additional static (DC) potential confines their movement along the z-axis. The total potential in the trap is thus given by

$$\Phi(x, y, z, t) = \frac{V_{RF}}{2r_0}(x^2 - y^2)\cos(\Omega t) + \frac{U}{2z_0^2}\left[2z^2 - x^2 - y^2\right], \tag{2.1}$$

where the first term denotes the radio-frequency voltage oscillating with a angular frequency Ω and an amplitude V_{RF}. The second term denotes the axially confining direct current (DC) voltage with the amplitude U. The characteristic trap distance r_0 is the radial distance from the trap's center to the parallel rod electrodes. The total confining potential results in a linear area of confinement for the ions along the z-axis rather than a single point.

a)Schematic side view of a linear Paul trap. **b)**Schematic front view of a linear Paul trap.

Figure 2.1.: Side a) and front b) view of a linear Paul trap. Four parallel rods generate the radial confinement of the ions. The two black rods provide the radiofrequency potential voltage $\propto V_{RF} \cdot \cos(\Omega t)$, while the two white rods act as the radio frequency ground. The characteristic distance of the trap r_0 denotes half of the distance between two opposing rod electrodes, i.e. the radial distance for each of the rods from the center of the trap. Two additional electrodes on either side of the rods, the endcap electrodes (not pictured), provide axial confinement, keeping the charged particles trapped linearly along the z-axis. Figure taken from [33].

The equations of motion for a single ion in the trap can be solved by decoupling the motion in each of the spatial coordinates. For an ion with mass m and charge e, the equation of motion in the x-direction is given by [33]

$$\ddot{x} = -\frac{e}{m}\frac{\partial \Phi}{\partial x} = -\frac{e}{m}\left[\frac{V_{RF}}{r_0}\cos(\Omega t) - \frac{U}{r_0}\right]x. \tag{2.2}$$

By making the following substitutions

$$q_x = \frac{2eV_{RF}}{mr_0^2\Omega^2}, \quad a_x = \frac{4eU}{mr_0^2\Omega^2}, \quad \tau = \frac{\Omega t}{2}, \tag{2.3}$$

one can transform the original differential equation into the standard form of the Mathieu differential equations [33]

$$\frac{d^2x}{d\tau^2} + (a_x - 2q_x \cdot \cos(2\tau))x = 0. \tag{2.4}$$

The Mathieu differential equation comes from a wider class of differential equations for periodic coefficients. Solutions to the Mathieu equation follow the form

$$x(\tau) = Ae^{i\beta_x\tau} \sum_{n=-\infty}^{\infty} C_{2n}e^{12n\tau} + Be^{-\beta_x\tau} \sum_{n=-\infty}^{\infty} C_{2n}e^{-i2n\tau}, \tag{2.5}$$

where the coefficient C_{2n} and exponent factor β_x are real-valued characteristics, dependent on a_x and q_x. On the other hand A and B are simply arbitrary constants to satisfy particular boundary conditions or used for normalization.

The solution for the Mathieu equations in this context can be simplified by looking at the lowest-order approximation of the motion. The so-called secular approximation assumes a motion in the small q_x regime where $q_x \ll 1$, meaning the radio-frequency field is weak or rapid enough that the ion only experiences the time-average effect. This means that the fast-driven oscillative motions (micromotion) are small compared to the slower secular motion of the ion. This leads to an approximated solution for the exponent β_x given by [33]

$$\beta_x \approx \sqrt{\frac{a_x + q_x^2}{2}}. \tag{2.6}$$

This same process can be performed for the y and z directions of the ion. The only difference being the sign of the oscillation in the y axis and that there is no oscillating field on the z axis. This leads to the the relation between the parameters

$$q_y = -q_x, \quad q_z = 0. \tag{2.7}$$

A trapped charged particle in a linear Paul trap will thus be stable in all directions if

$$0 \leq \beta_i \leq 1, \quad \text{for all} \quad i \in \{x, y\}. \tag{2.8}$$

The stability diagram for such a trap is symmetric around the a_x axis, as seen in Fig. 2.2. The stability lines of the two directions β_x and β_y are mirrored images of each other.

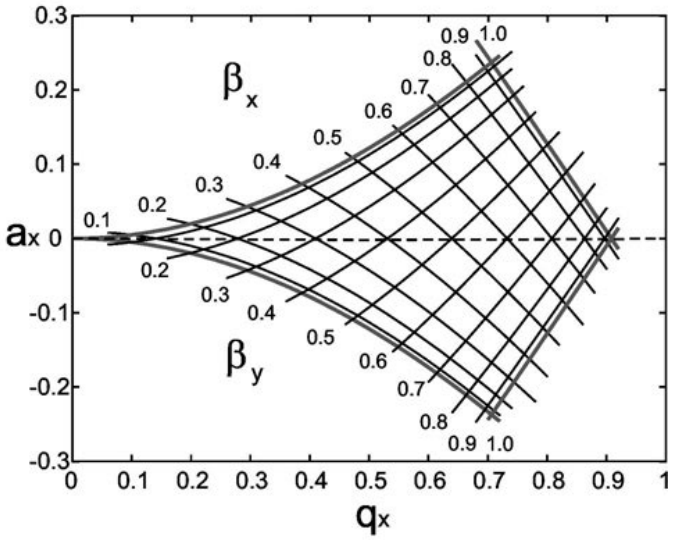

Figure 2.2.: Stability diagram for a linear Paul trap. The axis coefficients a_x and q_x depend on the trap's parameters and the DC and radio-frequency voltage amplitudes, respectively. The lines in the graph are solutions to the Mathieu equation coefficients β_x and β_y, which correspond to the movement of the trap in the x-axis and y-axis. The motion of the ion is thus bounded and stable for the entire region where $0 \leq \beta_x, \beta_y \leq 1$. Figure taken from [33].

2.1.2. Generation and Detection of Ions

This section gives an overview of the techniques used for generating the trapped ions inside a linear Paul trap, with a particular focus on laser ablation as a loading mechanism. It also aims to elaborate on the ion detection mechanism used. In the context of this work, a destructive detection mechanism, using a microchannel plate detector, is employed.

The development of a linear Paul trap involves the selection of a suitable technique for loading ions into it. This can be achieved by either generating ions outside the trap and consequently loading them, or by generating them already inside. Loading ions from an external source usually involves switching off the front electrode of the trap, letting ions into the center of the trap, and then switching it back on [34, 35]. As long as the ions don't have enough energy to escape, they will remain trapped. Alternatively, generating ions inside the trap has the important advantage that once ions are generated, they will be almost immediately trapped inside, given the proper trapping parameters are set [31].

Generating ions inside the trap can be done in a few different ways. This includes, for example, electron bombardment to ionize atoms from atomic ovens. This process is, however, not highly selective and can cause contamination of the trap. Laser ablation offers a more selective and material-efficient mechanism for ion generation inside the trapping volume. This is done by focusing an intense laser beam into a solid target inside the trap in short nanosecond pulses. The solid material, commonly a metal, strongly absorbs the energy from the laser light, rapidly heating up the surface of the material. The electrons at the surface rapidly thermalize, causing rapid heating of the material to the point that this surface layer vaporizes, ejecting neutral atoms, as well as electrons and ions, which consequently remain trapped in the potential well [36].

Once a suitable ion loading technique is chosen, a detection mechanism has to be employed to verify the presence of ions in the trap. In quantum information experiments that use linear Paul traps, ion detection typically relies on observing fluorescence from electronic transitions of

the ion. This is achieved by illuminating the ions with a laser that excites a transition, causing the ions to emit light [37]. Destructive detection mechanisms of ions are also possible and are employed in this work. Destructive detection can be performed by sending the trapped ion cloud to a charged particle detector, such as a microchannel plate detector (MCP).

Microchannel plate detectors can be used for detecting both ions and other charged particles, such as antiprotons. They consist of a round active area with a densely packed array of amplifying channels, which are typically a few micrometers wide and are coated with an electron-emitting material. The small channels are parallel to each other, yet tilted at an angle from the detector plane to maximize the detection efficiency. The matrix housing the channels is composed of a material such as lead glass, ensuring insulation between the channels. The front and back surfaces of the MCP are metal-coated, functioning as the input and output electrodes of the detector [38]. An additional phosphor screen in the back is then often added to image the charged particles. A schematic depiction of an MCP detector can be found in Fig. 2.3.

The detection of ions in a Paul trap is thus achieved by ejecting the trapped ions in the direction of the MCP detector, for example, by lowering the back endcap potential in the trap, as is done in this experiment. When the ion hits the front of the channel, one or a few electrons are released inside and are moved along the channel by the voltage difference applied between the input and output. These secondary electrons emerging from the primary impact hit the semiconductor electron-emissive layer of the channel, generating a cascade of secondary electrons in an avalanche-like manner, thus amplifying the signal. A schematic view of this process in a single channel can be seen in Fig. 2.4. Detection of the signal then follows, either by directly measuring the output signal of the anode or via imaging from the phosphor screen in the back. The phosphor screen is held at a positive voltage difference from the front and the anode of the detector, accelerating the electrons towards it. When the energetic electrons hit the phosphor layer, it absorbs the energy and re-emits it as visible light, an image of which can be captured by a CCD camera, shedding light into not only the quantity of ions but their spatial distribution as well [39].

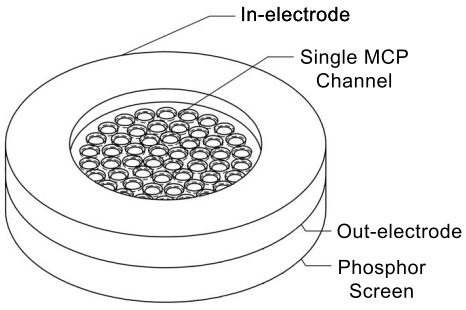

Figure 2.3.: Schematic diagram of an MCP detector. Ions hitting the in-electrode of the MCP generate electrons, which begin a cascade of secondary electrons inside the MCP channels. The amplified signal exits through the out-electrode and is converted into an image by the phosphor screen.

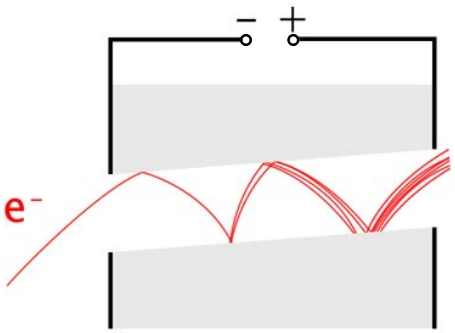

Figure 2.4.: Schematic depiction of a working single channel of the detector. It shows the incoming electron as well as the cascade of secondary electrons released into the channel.

2.2. Synthesis and Storage of Low-Energy Antiprotons

The vast network of accelerators at the European Organization for Nuclear Research (CERN) allows scientists to experiment with exotic matter that can't be produced without such facilities. This includes their largest and most well-known collider, the Large Hadron Collider (LHC), which is able to accelerate protons and heavy ions to energies in the order of a few TeV [40] to produce high-energy collisions between them. Studying these scattering events has enabled important discoveries, such as that of the Higgs Boson in 2012 [41], helping physicists better understand the Standard Model of particle physics.

Part of this network of accelerators and colliders is focused on the study of antimatter, another constituent of the Standard Model. The study of antimatter is of particular importance to particle physicists, as its existence is still an open question and not yet fully understood. This puzzle, known as the baryon asymmetry problem, stems from the generation of baryonic matter (baryogenesis) in the early universe with a resulting perceived excess of baryons over antibaryons in the current universe. The violation of charge and parity (CP) symmetry in reactions of the early universe allowed for a slight preference for matter over antimatter; however, this small disparity only partially explains the total asymmetry found [4]. Physicists have therefore been on the lookout, performing experiments with antimatter at both low and high energies to help explain this imbalance.

High-energy antimatter measurements routinely performed at CERN's LHC go hand in hand with low-energy antimatter experiments. For this reason, CERN has devoted a fraction of its facilities to the study of antimatter at low energies. This facility, known as the Antimatter Factory, is a network of accelerators and decelerators that produce antiprotons and then decelerate them down to energies that allow their trapping and storage in charged particle traps [42].

Experimental collaborations at CERN's Antimatter Factory, such as the Baryon Antibaryon Symmetry Experiment (BASE), have demonstrated exceptionally precise measurements of the antiproton's lifetime [7] and magnetic moment [8], further pushing the boundary of testing matter-antimatter asymmetries. Nevertheless, antimatter experiments at the Antimatter Factory extend beyond the simplest antimatter nucleus, the antiproton, to studies of anti-hydrogen, the simplest antimatter atom. These include, for example, Antihydrogen Antimatter Experiment: gravity, Interferometry, Spectroscopy (AEgIS), which aims to measure the force of gravity on these neutral antimatter atoms [13].

The main current limitation to low-energy antiproton experiments is their availability, as generating, slowing down, and storing cold antiprotons can currently only be done at CERN's Antimatter Factory facilities. Furthermore, experiments operating at the Antimatter Factory are limited in precision by the electromagnetic fields of surrounding experiments. For this reason, efforts to develop a transportable trap for antiprotons are currently underway. These include the BASE-STEP device [17] and the PUMA trap [18]. Both of these are transportable cryogenic Penning traps that aim to transport large numbers of cold antiprotons. In this work, a different approach to the problem of antiproton transfer is presented by pursuing the transport of antiprotons in a room-temperature device based on theoretical predictions for the cross-section of antiprotons.

This section aims to explain the process of low-energy antiproton production at the Antimatter Factory, as well as discuss how experiments at these facilities are able to trap and experiment with antiprotons and antimatter atoms. This will be further illustrated by the case study of the AEgIS experiment, whose apparatus will serve as the source of the antiprotons to be trapped in the transportable Paul trap developed during this thesis. Furthermore, the theoretical foundation behind the development of a room-temperature trap for antiprotons is discussed.

2.2.1. Synthesis of Low-Energy Antiproton at CERN

The Antimatter Factory at CERN is currently the only facility in the world that can produce low-energy antiprotons to be trapped in charged particle traps. This is enabled by CERN's complex of accelerators and decelerators, in particular the Antiproton Decelerator (AD) and Extra Low Energy Antiproton ring (ELENA), which in combination allow for slowing antiprotons down to an energy of 100 keV [6] allowing for trapping and experimentation. The section of the accelerator network involved with the production of low-energy antiprotons is presented in Fig. 2.5.

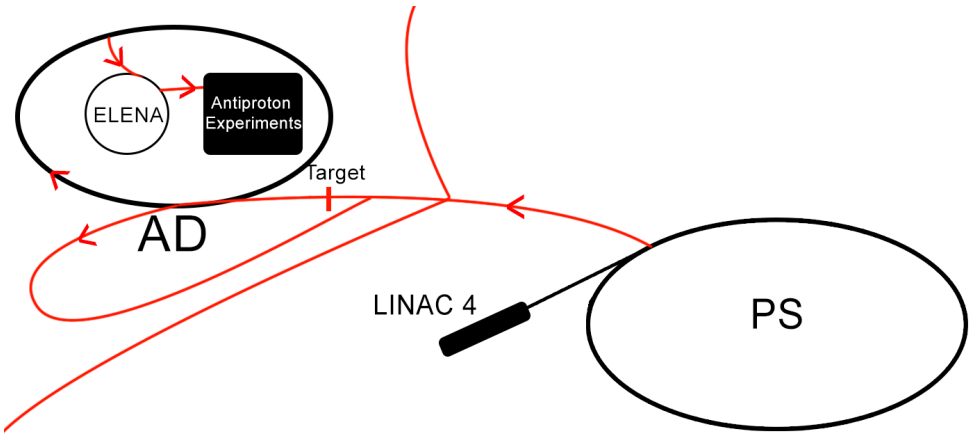

Figure 2.5.: Schematic layout of the section of CERN's accelerator complex focused on production and deceleration of antiprotons for low-energy experiments inside particle traps. Antiprotons are initially produced by collisions of protons produced by the linear accelerator (LINAC) 4 and accelerated to momenta of up to 26 GeV/c at the proton synchrotron (PS). By acceleration of the proton beam onto an Iridium target, a proton-antiproton pair of momenta p =3.6 GeV/c is produced. The produced antiprotons are bunched and cooled via a series of deceleration steps at the Antimatter Factory's two decelerating rings, the Antiproton Decelerator (AD) and the Extra Low Energy Antiproton ring (ELENA) until reaching momenta of 13.7 MeV/c, suitable for usage in trapping experiments.

The antiproton production chain begins at the high-energy proton source, the linear accelerator (LINAC) 4. At the LINAC 4, negative hydrogen ions (H^-) are generated by an ion source and are accelerated to energies of 160 MeV [43]. The protons are then sent to the Proton Synchrotron Booster (PSB) and Proton Synchrotron (PS), which, in conjunction, accelerate them up to momenta 26 GeV/c. The accelerated proton beam is sent to collide with an Iridium target found at the entrance of the AD, where a fraction of these collisions will generate antiprotons via pair production. The pair production reaction of the incoming antiproton beam with that of the stationary target is given by

$$\mathrm{p} + \mathrm{p} \rightarrow \mathrm{p} + \mathrm{p} + \bar{\mathrm{p}} + \bar{\mathrm{p}}\,; \tag{2.9}$$

where p denotes a proton and $\bar{\mathrm{p}}$ an antiproton. The threshold proton beam energy required to produce a proton-antiproton pair with momenta of $p_{\mathrm{p}} = p_{\bar{\mathrm{p}}} \approx 1\,\mathrm{GeV}/c$ is approximately 6 GeV/c. To increase the antiproton yield, however, much higher energies are used, as previously mentioned. The generated antiprotons thus have higher momenta of $p_{\bar{\mathrm{p}}} \approx 3.6\,\mathrm{GeV}$ [44].

Following pair production, antiprotons are electromagnetically filtered from the protons and are focused with a magnetic horn to go through the AD in bunches of about 5×10^7 $\bar{\mathrm{p}}$. The AD is a synchrotron of a 188 m circumference that functions as the first cooling stage for the antiprotons following their formation at high energies. Any unwanted particles in the beam are typically filtered out in the initial revolutions around the AD due to their charge-mass ratio difference with that of the antiprotons [44].

The beam deceleration through the AD takes a total time of about 100 s, undergoing a series of three deceleration phases during this time. The first cooling step in the AD is bunch rotation via radio-frequency (RF) fields. During this process, an RF cavity applies longitudinal electric fields to the bunches of antiprotons. These accelerate slower particles while decelerating faster ones, depending on their position in the bunch. The net effect of this process is the rotation of the antiproton distribution in phase space, making the energy spread narrower while their time spread becomes broader [44].

Following bunch rotation, two rounds of stochastic cooling are performed. Stochastic cooling is a technique that improves the beam by both improving its spatial confinement and momentum uniformity. In the AD, the stochastic cooling process is implemented using a pickup-kicker system found around the synchrotron. The 'pickup' part of the system involves detectors that detect small deviations in the momenta and transverse position of the beams relative to their mean. These small discrepancies are then used to correct the beam by 'kicking' via steering electrodes, converging the beam. The antiproton beam momentum after this cooling step is 2 GeV/c [44].

The last cooling step involves two stages of electron cooling of the antiproton beam. Electron cooling is a type of sympathetic cooling, i.e., cooling via Coulomb collisions, useful in the case of antiprotons due to the electron's negative charge, allowing for temporary co-trapping. For this cooling step the antiproton beam is allowed to merge with an electron beam for a 2 m segment of the AD. Velocities of both beams are matched so that, for the center of mass frame, antiprotons are colliding with a stationary electron cloud at a lower temperature. The Coulomb scattering of these two beams results in a loss of energy from the antiprotons by transfer to the electrons. A second round of electron cooling is then performed and the beam is rebunched, resulting in an antiproton beam of 100 MeV/c, corresponding to a kinetic energy of 5.3 MeV [44].

In the past, antiprotons leaving the AD were successfully captured by employing degrader foils used to slow the incoming antiprotons from the AD down to suitable trapping energies in the order of 10 keV. Although effective for decelerating antiprotons to suitable trapping energies, 99.9% of the antiprotons are annihilated in the foil [44]. A newer decelerating ring, the ELENA ring, was installed at the Antimatter Factory at CERN to function as a secondary deceleration system for low-energy antiproton delivery to the experiments [6]. This allows for the employment of thinner degrader foils, resulting in fewer particle losses.

The ELENA ring has a 30 m circumference, making it comparably smaller than the AD. It sits inside the AD ring waiting for incoming antiprotons to undergo their second deceleration stage. The entire cooling process consists of several cycles around the ELENA ring and takes approximately 20 s, the first couple of which are the injections of the antiprotons from the AD [6]. The cooling mechanisms employed during the cycle at the ELENA ring are similar to those of AD. Initially, the beam is injected into a so-called RF bucket. This is a region of stability in an oscillating electric field from an RF cavity found in the accelerator. This process leads to the first deceleration ramp in a cycle, accounting for a reduction of the antiproton beam momentum down to 35 MeV/c. The antiprotons undergo a secondary RF deceleration step in between two electron cooling stages until reaching a final extraction momentum of 13.7 MeV/c, equivalent to a kinetic energy of 100 keV [6].

Once slowed down, low-energy antiprotons are provided across the Antimatter Factory site to five separate collaborations, namely the Antihydrogen Laser PHysics Apparatus (ALPHA), the Atomic Spectroscopy And Collisions Using Slow Antiprotons (ASACUSA), the Baryon Antibaryon Symmetry Experiment (BASE), the Gravitational Behavior of Antimatter at Rest (GBAR), and lastly, the Antihydrogen Experiment: Gravity, Interferometry, Spectrometry (AEgIS). The last of these collaborations, the AegIS experiment and in particular their experimental apparatus, will be discussed in detail in the following section.

2.2.2. The AEgIS Experiment as a Source of Low-Energy Antiprotons

The Antihydrogen Experiment: Gravity, Interferometry, Spectroscopy (AEgIS) Collaboration at CERN is one of the experiments found inside the Antimatter Factory's facilities. This collaboration aims to study the effects of gravity in antimatter systems by studying the free fall of antihydrogen [13]. Antihydrogen is the simplest possible antimatter atom, composed of an antiproton and a positron. Its neutral charge makes it an ideal tool for studying the effects of gravity on antimatter, which, according to the weak equivalence principle, should be measured to be equivalent to that of matter [45].

The AEgIS collaboration's experimental apparatus is equipped to catch, trap, and accumulate incoming antiproton bunches from the ELENA storage ring. As seen in Fig. 2.6, the apparatus consists of two cryogenic Penning traps equipped with electromagnets that produce a magnetic field of 5 T and 1 T respectively. An additional positron accumulator trap system is also directed towards the trap, but is only in use for antihydrogen experiments. Antiprotons are directed towards the AEgIS apparatus via an extensive beamline coming from the ELENA ring. This beamline features several bender electrodes and quadrupole magnets that have been optimized by the AEgIS experiment to deliver the highest possible quality of beam, both in terms of density and spread [46]. This procedure of extracting antiprotons coming from ELENA and catching them can be repeated several times to accumulate antiprotons for subsequent experiments.

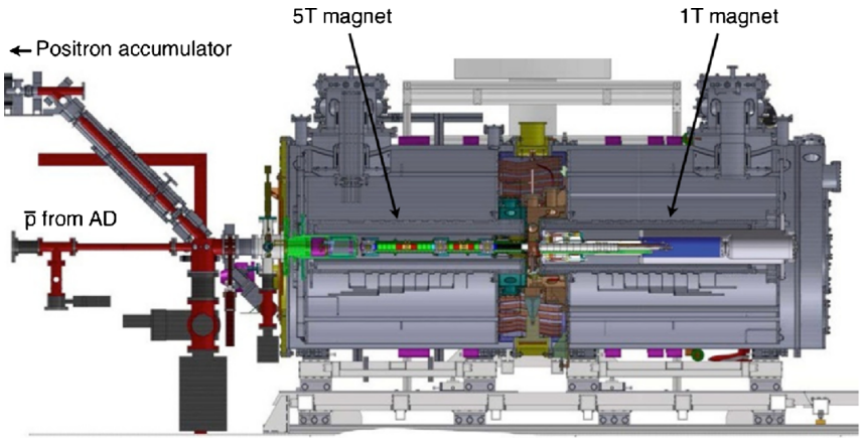

Figure 2.6.: Computer-aided design drawing of the AEgIS experimental apparatus. The apparatus consists of two Penning traps, each equipped with a superconducting electromagnet producing magnetic fields of 5 T and 1 T, respectively. Antiprotons coming from the ELENA ring are initially captured by the 5 T magnetic field Penning trap, which features three high-voltage electrodes designed for this operation. Here, they are electron-cooled and stored to proceed with either antihydrogen or extraction experiments. For antihydrogen experiments, antiprotons are shuffled to the 1 T magnet trap, where they are combined with positrons from the positron accumulator to produce antihydrogen. Alternatively, for the extraction operation of low-energy antiprotons, after electron cooling, they are reverse extracted back towards the beamline coming from the direction of the ELENA ring. This figure has been taken from [47].

Antiprotons caught by the AEgIS apparatus are consequently cooled via electron cooling, a form of sympathetic cooling involving proton-electron Coulomb collisions. This is done by preloading the 5 T catching trap with approximately 10^8 electrons that naturally cool down to 10 K by emitting cyclotron radiation. Upon capture, antiprotons interact with the cold electron, transferring their energy until reaching energies in the eV scale within approximately 50 s [48]. The resulting temperature of the electron-antiproton plasma can be measured from plasma diagnostics and centrifugal separation limits [49]. From this diagnostic, it is determined that both

species reach an estimated upper bound of tens of Kelvins, corresponding to an energy of a few millielectronvolts.

Following the thermalization of the plasma, a rotating-wall compression can be employed to further shrink and squeeze the electron-antiproton cloud on the axis of the Penning trap. This multi-step process is required to achieve a dense and compact antiproton cloud. The first step involves applying a rotating electric field to the trap, known as a rotating-wall drive. This field causes the plasma to rotate much faster, generating a stronger radial confinement due to the centrifugal force. This effect has a particularly strong effect on the electrons of the mixed-species plasma, making the electron cloud shrink inward. If done slowly and carefully, antiprotons follow suit due to their Coulomb coupling to the electrons. This process is repeated using higher rotating frequencies until the plasma radius is shrunk down from 1.6 mm to 0.17 mm, with a density increase of approximately 55 times [48].

Centrifugal separation of the mixed-species plasma then comes as a result of the confinement dynamics inside the Penning trap. Electrons and antiprotons oscillate inside the trap at the same magnetron frequency, which is defined by the voltage of the electrodes in the trap. For such a plasma where one species is much heavier than the other, this causes an almost complete separation of electrons at cryogenic temperatures. Once the antiproton and electron clouds are centrifugally separated, electrons can be kicked out by switching off the trapping voltage to 0 V for a short duration on the scale of less than a microsecond. If switched off long enough for the lighter electrons to escape, but not so long that the antiprotons are also ejected, the antiprotons will remain. This results in a single species dense plasma of cooled antiprotons [50].

Once antiprotons are densely confined in a single-species plasma, the whole process can be repeated to accumulate antiprotons inside the experimental apparatus. Extraction of antiprotons can then follow by ejecting the cooled antiprotons back into the beamline towards the direction of the ELENA ring. The AEgIS beamline has two extraction sites along it, one at 75° and one at 45° from the antiproton beam axis, as seen in Fig. 2.7. The extraction port used for antiproton extraction into the transportable Paul trap is the one located at 75°.

In addition to serving as antiproton extraction ports, the AEgIS experimental collaboration plans to utilize these as injection ports for injecting ions into the AEgIS apparatus. This makes this multipurpose beamline a flexible tool for different lines of antimatter research.

2.2.3. Low-Energy Antiproton Storage at Room Temperature

The current main limiting factor in the field of antimatter is the scarcity of antiprotons as an experimental resource. Vast networks of colliders, such as those at CERN's Antimatter Factory facilities, are required for the generation of an antiproton beam at energies low enough to be trapped in a cryogenic particle trap. Furthermore, the ability to transport antiprotons outside of CERN's Antimatter Factory facilities is a goal yet to be achieved. Currently, two cryogenic transportable antiproton Penning traps are being developed by collaborations at CERN's Antimatter Factory facilities, namely the PUMA [18] and BASE-STEP [8] devices. A cryogenic device is essential for the transport of large numbers of antiprotons, which can easily annihilate even under UHV conditions. In contrast, a transportable room-temperature device would not be able to reliably trap and transport such a high number of antiprotons.

The development of a room temperature trap for antiprotons relies on testing the annihilation cross-section of antiprotons trapped at higher energies than those habitually used in such experiments. This would have the drawback of not being suitable for transporting large numbers of antiprotons, with the upside of being a more portable and affordable device. The main premise of the development of a room temperature trap for transporting antiprotons comes from the

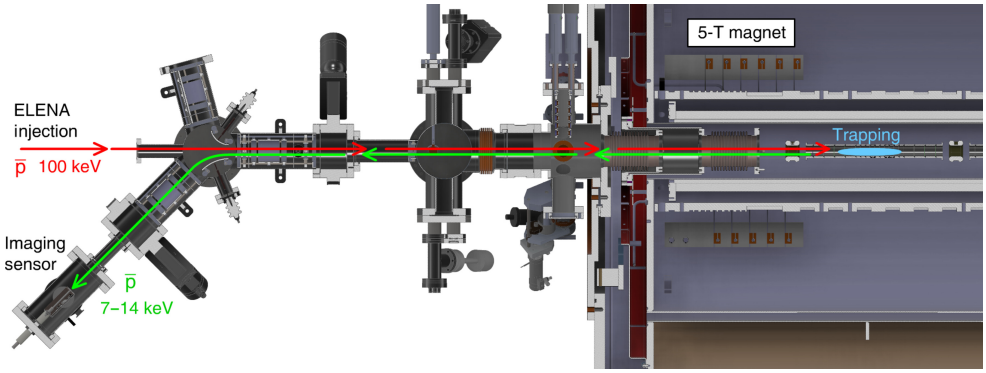

Figure 2.7.: Computer-aided design drawing of the AEgIS beamline. Antiprotons coming from the ELENA ring into the 5 T magnet trap are shown in red. Once in the trap, antiprotons are electron cooled and can be ejected for extraction in either of the two extraction ports along the beamline. The cold antiproton beam coming from the 5 T trap is shown in green. The first extraction port at 75° is to be used for injecting antiprotons into the transportable Paul trap. The second port at 45° is used for other antiproton experiments. Between the 5 T Penning trap and the bending electrode region of extraction, a gate valve (here GV1) is in place to separate the vacuum across the beamline. An additional gate valve is in place towards the ELENA ring (here GV ELENA), which again separates the vacuum of the AEgIS experiment from that of the main decelerator ring. Both of these gate valves can be controlled via the AEgIS control system. This figure has been taken and modified from [51].

calculations of the annihilation cross section of antiprotons presented in Ref. [52]. This article mainly focuses on the discussion of atomic-scale interactions that lead to the annihilation of antiprotons. Atomic-scale processes involve Coulomb forces and electromagnetic field interactions, in particular with residual hydrogen molecules inside the trap. These reactions play a significant role in determining the rate of antiproton annihilation in such an environment.

During these interactions, atomic-scale components in matter combine with antimatter to form bound states from which annihilation then occurs. These so-called rearrangement collisions can, under certain conditions, have a greater cross section than direct particle-antiparticle annihilation, thus playing a major role in antiparticle loss inside the trap's environment. The two main reactions considered in Ref. [52] to be considered here are the annihilation of antiprotons with hydrogen atoms (H) and hydrogen molecules (H_2) given by

$$\bar{p} + H \rightarrow Ps + e^-, \tag{2.10}$$

$$\bar{p} + H_2 \rightarrow Pn + e^- + (H \text{ or } p + e^-), \tag{2.11}$$

where Ps is the positronium bound state composed of an electron and a positron, and Pn denotes the protonium bound state composed of a proton and an antiproton, providing additional means for antiproton annihilation.

Under semiclassical considerations of the inelastic collision process in a 1 : 1 admixture of matter and antimatter, the annihilation cross sections for Eq. 2.10 and Eq. 2.11 are considerably dominant for antiprotons with energies lower than 10 eV [52]. For usual trapping temperatures in antimatter experiments of 4 K, with corresponding kinetic energies of $E \approx 10^{-5}$ eV, a rearrangement cross section of $\sigma_{\text{H-}\bar{p}} = 10^{-18}$ m^2 is expected.

The semiclassical model presented suggests that for antiprotons at energies between 10 eV−100 eV, the rearrangement collision cross section would be reduced by a factor of 10^4 to $\sigma_{\text{H-}\bar{p}} = 10^{-22}$ m^2 [52]. This indicates that by trapping antiprotons at energies higher than is currently done at the Antimatter Factory facilities, one would expect a drastic reduction of the annihilation cross section

stemming from rearrangement collisions with hydrogen. Testing the annihilation cross section of antiprotons at higher energies, namely in the tens of electronvolts, is the basis of operation for the room temperature transportable trap presented in this thesis.

2.3. Highly Charged Ions from Antiprotons: Pathways and Opportunities

The quantum two-body problem for the hydrogen atom, describing the Coulomb interaction between a proton and an electron, is the simplest and most well-understood atomic system in quantum theory. Its simplicity alongside deep theoretical understanding and precise experimental verification serves as a solid foundation for discussing more complex systems. Although the hydrogen atom itself is the primary example of this behavior, other atoms that exhibit a single orbiting electron are often referred to as hydrogen-like atoms. In this context, the following section will present a brief outline of the quantum mechanical description of the hydrogen atom, establishing the foundation to understand similar systems with a higher nuclear charge (Z). While this description can also apply to other hydrogen-like systems, the main focus of this section will be placed on hydrogen-like ions with a high nuclear charge. These are often referred to as highly charged ions (HCI)because they have a large positive net charge. Indeed, in the hydrogen-like case, the highly charged nucleus has only one electron orbiting around that is screening its charge towards the outside.~~, since they have a highly charged nucleus and only one electron orbiting around it.~~[gio]

Building on the concept of hydrogen-like ions, this chapter explores the energy level structure of highly charged hydrogen-like ions. Both the fine and hyperfine structure of the energy levels will be discussed, in particular, focusing on how they scale for higher nuclear charge (Z). As the nuclear charge increases, energy level separation becomes more pronounced, differing from the example of hydrogen.

After exploring the internal energy splitting, the focus will shift to discussing external fields and their role in influencing the energy level structure. External electromagnetic fields shift HCI differently than other nuclei, making them crucial for understanding the properties of their energy level scheme.

These distinct properties of HCI will then be discussed in the context of the opportunities they present for applications in the field of quantum sciences. Their large hyperfine level splitting, along with their coherence properties, make them particularly relevant in the field of metrology, where they offer the potential for highly accurate measurements of time and fundamental constants, as well as testing quantum electrodynamics (QED) and studying fundamental nuclear structures.

After reviewing their properties and applications, the focus will be placed on the generation of these highly charged two-level systems. Current methods of HCI generation will be presented. The innovative approach of producing HCI via interactions with antiprotons will be discussed and compared with conventional means. Finally, the feasibility of this method will be examined to assess application opportunities for future experiments.

2.3.1. Energy Level Structure of Hydrogen-like Ions

The solutions for the quantum two-body-problem of the hydrogen atom are given by solving the Schrödinger equation [53]

$$i\hbar\Psi(\vec{r},t) = \hat{H}\Psi(\vec{r},t) \tag{2.12}$$

for a system composed of a single proton and a single electron. Here, $\hbar$ and i refer to the Planck constant and imaginary unit respectively. The function $\Psi(\vec{r},t)$ is the wave function of the system, and $\hat{H}$ the Hamiltonian, which for the non-relativistic case is given by [53]

$$\hat{H} = \frac{\hbar^2}{2m_\mathrm{e}}\nabla^2 - \frac{\mathrm{Z}e^2}{2\pi\varepsilon_0|\vec{r}|}. \tag{2.13}$$

The first term describes the quantum analog to describe the kinetic energy of the system, where m_e is the mass of the electron and $p = -i\hbar\nabla$ is the momentum operator. The second term refers to the potential energy given by the Coulomb interaction of the nucleus with the electron, where Z is the nuclear charge, e the elementary charge of the electron, and ϵ_0 the vacuum permittivity.

The time-independent solution to this problem is given by transferring into spherical coordinates and separating the wave function into [53]

$$\Psi(\vec{r}) = R_{nl}(r)Y_{lm}(\vartheta,\varphi), \tag{2.14}$$

where $R_{nl}(r)$ denotes the radial wavefunction that only depends on the radial distance $|\vec{r}| = r$, and $Y_{lm}(\vartheta,\varphi)$ is known as the spherical harmonics. Solutions of this form describe stationary states of the Scrödinger equation with angular momentum quantum number l and energy E_n for the respective principal quantum number n. The magnetic quantum number m determines the z-component of the angular momentum. Following this approach, the energy levels of the system E_n are given by [53]

$$E_n = -\frac{1}{2}\left(\frac{e^2}{2\pi\epsilon_0}\right)^2 \frac{Z^2\mu}{n^2\hbar^2}, \tag{2.15}$$

meaning that the nonrelativistic energy levels depend solely on the principal quantum number n. In the case of $n = 1$ for hydrogen ($Z = 1$) the result is [53]

$$E_1 = \frac{m_e e^4}{8h^2\epsilon_0^2} = hcR_\infty, \tag{2.16}$$

where R_∞ is commonly referred to as the Rydberg constant.

Until now, only the ideal case without external or additional internal fields has been considered. However, when describing real systems, corrections to the aforementioned energy levels must be made. These corrections describe a splitting of the energy levels that increasingly scales with the nuclear charge, making them particularly relevant when discussing highly charged ions. Here, the most effects that scale with the nuclear charge Z will be discussed, namely the fine structure, the Lamb shift, and hyperfine splitting.

The first correction that needs to be applied results from the fine-splitting of the energy levels caused by the relativistic motion of the electron around the nucleus and the electron's spin. When not ignoring the relativistic motion of the electron and including the first-order relativistic correction term in the kinetic energy of the system, the Hamiltonian can be expressed as the familiar Hamiltonian from Eq. 2.13 with an additional perturbation of the form [53]

$$H_\mathrm{rel} = -\frac{p^4}{8m_e^3c^2}. \tag{2.17}$$

Applying first-order perturbation theory, the energy shift ΔE_rel caused by the relativistic motion of the electron can be determined to be [53]

$$\Delta E_\mathrm{rel} = -\frac{E_n^2}{2m_\mathrm{e}}\left(\frac{4n}{l+1/2} - 3\right), \tag{2.18}$$

which is in turn proportional to Z^4. It is important to note that this correction depends on both n and l, breaking the degeneracy between energy levels of states with the same n and different l quantum numbers, requiring a new quantum number, $j = l + s$, the total angular momentum. Similarly, the spin of the electron introduces an additional correction due to the spin-orbit interaction which results in another correction $\Delta E_{\text{so}} \propto Z^4$. These two corrections together result in what is known as the fine structure of the energy levels for hydrogen-like ions.

The Lamb shift, of the energy levels, on the other hand, is a purely non-relativistic effect resulting from the interaction of the electron with vacuum fluctuations of the electromagnetic field. This is a purely quantum electrodynamic effect that is much smaller than both the fine and hyperfine splittings but increasingly scales with the nuclear charge [54].

The hyperfine splitting of the energy levels, on the other hand, comes as a result of the interaction of the electron's magnetic moment with that of the nucleus. The coupling of the electron's total angular momentum J with the nuclear spin I results in new total angular momentum $F = I + J$. This coupling, in turn, introduces an energy shift [53]

$$\Delta E_{\text{hf}} = \frac{A_l}{2}\left[F(F+1) - J(J+1) - I(I+1)\right], \tag{2.19}$$

where A_l is a form factor depending on the angular momentum quantum number L. For single-electron hydrogen-like ions, the energy difference is given by [55]

$$\Delta E_{\text{HF}} = \alpha(\alpha Z)^3 \frac{m_e}{m_p}\frac{\mu}{\mu_N}\frac{2(2I+1)}{3I} \cdot m_e c^2 \left[A(1-\delta)(1-\epsilon)\right], \tag{2.20}$$

where α is the fine structure constant and μ/μ_N is the nuclear magnetic moment the nucleus in units of the nuclear magneton. The factors A, δ, and ϵ are the relativistic, nuclear charge distribution and nuclear magnetization (Bohr-Weisskopf) distribution correction factors, respectively.

The presence of external electric and magnetic fields perturb the previously discussed energy level structure of the atom. The splitting of energy levels due to a static electric field is known as the Stark effect and the response to magnetic fields is the Zeeman effect. Both of these effects will be discussed with a primary focus on their scaling for highly charged hydrogen-like ions.

The addition of an external static electric field perturbs the system with an additional potential term of the field. For single electron systems like Hydrogen-like atoms, first-order perturbation theory is sufficient to calculate the energy perturbation of the system. The solution to it is often expressed in parabolic coordinates and results in scaling with the nuclear charge of [53]

$$\Delta E_{\text{Stark}} \propto \frac{1}{Z}, \tag{2.21}$$

indicating a decrease in the effect for higher nuclear charges, as the electron is more tightly bound to the nucleus.

Similarly, static magnetic fields affect the atomic energy levels by an energy shift proportional to the strength of the magnetic field applied, a phenomenon known as the Zeeman effect. The fine and hyperfine structure splitting scale strongly with Z for highly charged hydrogen-like ions, meaning external magnetic fields need to be relatively strong to create a noticeable energy shift between the structure levels. When the magnetic interaction dominates over the spin-orbit coupling, the system enters the Paschen-Back regime. However, the spin-orbit coupling in highly charged hydrogen-like ions is significantly enhanced over that of neutral hydrogen, making it more resilient to static magnetic fields [53].

2.3.2. Applications of Highly Charged Ions

Certain properties of HCIs make them particularly suitable for precision experiments such as tests of quantum electrodynamics, fundamental physics, and metrology. Here, the focus is on HCIs that have a similar electronic structure to that of hydrogen but a higher nuclear charge. These are known as hydrogen-line HCIs. Their increased nuclear charge gives rise to distinct properties from those of hydrogen, for example, energy level splitting effects scale exponentially with Z, making them more pronounced in HCIs.

The inception of quantum electrodynamics (QED) came as a result of experimental observations, such as the previously discussed Lamb shift, that could not be explained through quantum theory alone. The theory of QED describes the fundamental interaction of photons with charged particles within quantum field theory. Tests of QED have historically focused on precision measurements of the Rydberg constant R_∞ [56]. This constant, previously defined in Eq 2.16 determines the highest possible photon energy in the hydrogen spectrum.

Small corrections to the maximal energy in the hydrogen spectrum arise due to the finite size of the proton; however, the size of the proton is not currently a well-defined property. This problem, commonly referred to as *"the proton radius puzzle"* refers to the discrepancy between different experimental techniques in determining the size of the proton. Measurements from muonic hydrogen indicate a significantly smaller radius than those from electron-proton scattering or spectroscopy measurements, suggesting systematic errors or limitations of the current theoretical frameworks [57].

Highly charged ions offer an alternative approach to probing QED under extreme conditions where the nucleus' electromagnetic field strength is significantly higher than in hydrogen. This strong interaction makes them suitable for studying QED corrections, which in the lowest-order correction are given by [56]

$$E^{(1)}_{\mathrm{QED}}(n,l,j) = \frac{\alpha}{\pi}\frac{(Z\alpha)^4}{n^3} m_e c^2 F^{(1)}_{(n,l,j)}(Z\alpha), \tag{2.22}$$

where $F^{(1)}_{(n,l,j)}$ is a slowly varying function of $Z\alpha$. Experimenting on HCIs with high Z allows to have a ratio of QED contribution that scales proportionally to Z^2. Hydrogen-like ions are presumed to be the best species in which to perform spectroscopic tests on QED corrections. Nevertheless, theoretical knowledge of the system is oftentimes limited, leading to large uncertainties [56].

For these applications, highly charged ions have been previously experimentally generated by a variety of different means, including via heavy ion storage rings and electron beam ion traps. Storage rings are particle accelerators that keep a particle beam circulating for time scales hard to achieve otherwise. This is particularly useful for the study of exotic ions such as HCIs [58]. Heavy ion storage rings are in particular useful for the study of heavier ions, which can not be reliably produced through other methods.

The primary functions of storage rings involve the confinement and circulation of the ion beam. This is achieved by reaching an ultra-low vacuum inside a pipe closed on itself, typically in a ring shape. Charged particles are kept inside the ring via magnetic [59] or electrostatic [60] elements that bend and focus the ion beam. The beam is kept stable inside the ring via diverse cooling mechanisms such as electron cooling, which reduces the momentum spread of the ions, stochastic cooling, which corrects small deviations in the ions' momentum via feedback loops, and laser cooling, which targets specific ion species of interest, ideally for spectroscopy.

In storage rings, HCIs can be produced by stripping electrons from fast-moving heavy ions. Beams of heavy ions are accelerated via linear accelerators, cyclotrons, or synchrotrons, injected

and focused into a thin stripper target. In general, the velocity needed for the beam to generate fully stripped ions can be estimated via the Bohr criterion, namely [58]

$$\beta = \frac{v_0}{c} = Z\frac{\alpha}{n}. \tag{2.23}$$

Here, β denotes the velocity needed in units of the speed of light c and how it is related to the nuclear charge Z, the fine structure constant α and principal quantum number n of the outermost electron. For example, to produce fully stripped Uranium ($Z = 92$, $n = 1$), a beam velocity of $\beta = 0.67$ [58] is needed. The thickness of the target can be controlled to produce specific charged states such as those of hydrogen-like HCIs.

The electron beam ion trap (EBIT) is an alternative method to heavy ion storage rings for generating HCIs. The general method used in EBITs is the ionization of low-charge ions via electron excitations through collisions with electrons. Studies on light HCIs have been greatly successful in EBITs, however, highly-charged fully stripped ions such as Uranium can't be reliably achieved, as it is the case with storage rings [61].

Ions are trapped in the EBIT via an electron beam ion source. A trap is generated via the space charge field of an electron beam, which is a radial static potential generated by the movement of the electron's charges around the electron beam. To the space charge, typically, an external magnetic field parallel to the electron beam is added for further strengthening of the confinement. An additional, axially confining field is created by a set of three cylindrical drift tubes through which the electron beam travels. Loading of the ions into the trap then follows by either ionizing the background gas inside the trap or injection of ions from a source [61].

Following the loading procedure, HCIs are generated via electron impact of the confined ions with the electron beam (electron impact ionization). During this process, the space charge field of the electron beam continues to play a large role, as it ensured the ions remain trapped during ionization. However, oftentimes the heating rate of the ions through elastic collisions with the electrons can make the ion cloud spread larger than the electron beam, reducing the ionization rate. This heating effect, in turn, limits the number of electrons that can be stripped through this method [61].

After ionization, HCIs may be analyzed via their X-ray emission spectrum. In this process, the electron beam plays a third key role, supplying energy to excite electronic states of the ions and participating in ion-electron recombination. When the ion relaxes from these excited states, they emit X-ray photons, which provide an insight into their energy level structure. Additionally, recombination of the highly charged ion with electrons from the beam also results in emission of X-ray photons. Adjusting the energy of the electron beam helps to precisely control probing different charge states of the ion to study these resonant phenomena [61].

2.3.3. Antiproton Annihilation as a Synthesis Method for HCIs

As previously discussed, heavy ion storage rings and electron beam ion traps are the two main methods utilized for the formation of HCIs. However, both of these methods have certain constraints that limit the types of HCIs species that can be produced. New approaches have thus been sought after for the study of HCIs. In particular, here, the formation of HCIs via antiprotonic atoms is presented.

Antiprotonic atoms are atoms where an antiproton replaces one of the orbiting electrons in the atom. Initially, antiprotons are captured at a highly excited state with a very large principal quantum number n, as seen in Fig. 2.8. Following capture, the antiproton begins to lose energy and transition downward, at first radiatively and then in a cascade-like manner [62]. In the

upper part of the cascade, the internal Auger process dominates, which is where the antiproton transfers its energy to atomic electrons, kicking them out of the atom. This causes a depopulation of the higher principal quantum number states without X-ray emissions. As the antiproton begins to occupy lower-level states, relaxation transitions begin producing X-ray photons, yielding information on the ionization state of the ion, which is now highly charged [63].

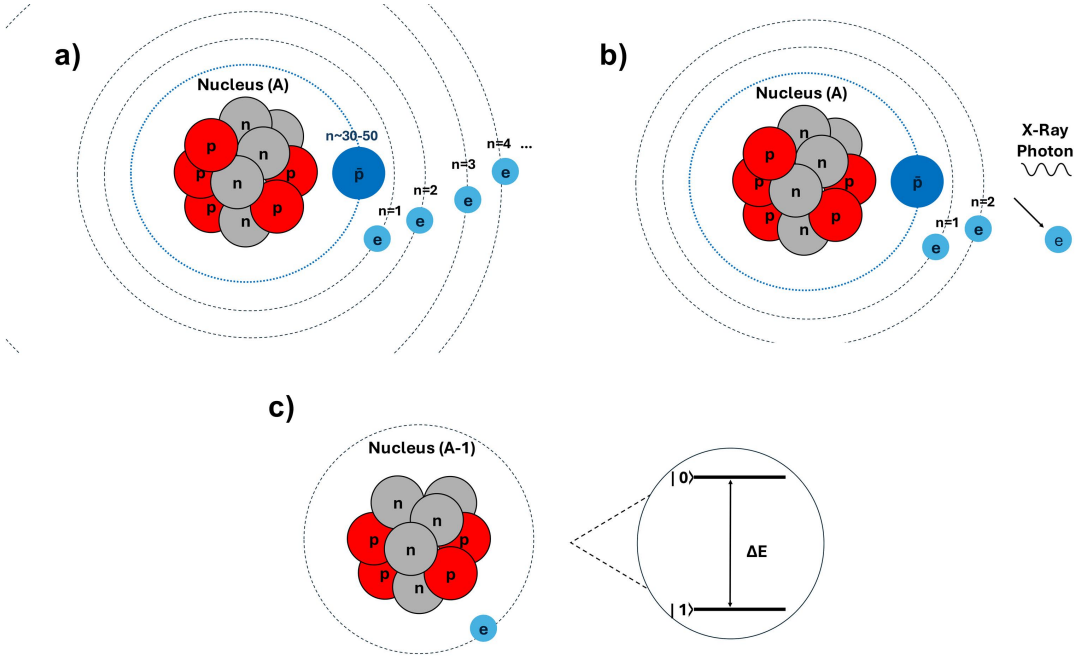

Figure 2.8.: Schematic depiction of the process for HCI formation via annihilation with an antiproton. a) Initially, the antiproton "$\bar{p}$" is captured by the atom (mass number "A") at a large principal quantum number ("n"), typically 30-50, but is found deep inside the electron cloud. b) The antiproton then initiates the Auger emission of electrons by energy transfer from Coulomb interactions, ejecting or exciting the orbiting electrons "e" around the nucleus and generating X-ray photons in the process. c) Finally, the atom is left fully or partially stripped, with a proton "p" (or a neutron "n") from the nucleus undergoing annihilation with the antiproton in the process (mass number "A−1"). This results in an HCI two-level system with energy difference ΔE and a single electron either left over after the stripping process or introduced during experimentation.

Experimentally, the X-ray spectrum for antiprotonic noble gases $\bar{p}$-Ar, $\bar{p}$-Kr, and $\bar{p}$-Xe have been studied at the low-energy antiproton ring (LEAR) at CERN, as presented in Ref. [63]. Inside this storage ring, an antiproton beam with momentum 105 MeV/c was sent through a gas medium confined in a volume of 20 cm^3 at a pressure of a few tens of mbar. By examining the resulting X-ray spectra, it was shown that this effect fully strips antiprotonic Krypton, while for atoms with higher electron binding energies like Xenon, it has been shown that some electrons remain [63].

3. Isomeric HCIs from Antiproton Annihilation

In this chapter, the motivation behind a transportable trap for antiprotons as a contribution to the field of precision spectroscopy with highly charged ions (HCI) is discussed. Here, experimental possibilities for producing highly charged isomeric ions via antiproton annihilation are described. A list of potential isomeric candidates that could be used for such an experiment is presented, along with the calculations of their hyperfine splitting wavelengths, calculations that were carried out alongside the work in this thesis. Furthermore, additional simulations performed to narrow down the list of candidates and their experimental feasibility are described. The simulations presented in this chapter were originally carried out in the context of the research article Ref. [23].

3.1. Metrology with highly charged isomeric ions from antiproton annihilation

Heavy ion storage rings and electron beam ion traps are the primary methods utilized for the formation of highly charged ions (HCIs). However, both of these techniques have certain constraints that limit the types of HCIs species that can be produced. As a result, new approaches have been sought for the study of HCIs. One such approach is the formation of HCIs via antiprotonic atoms.

Advancements in low-energy antiproton generation techniques have enabled the deceleration and manipulation of antiprotons, making the long-term storage of large numbers of antiprotons a possibility. The ELENA ring located at the antimatter factory at the European Organization for Nuclear Research (CERN) is currently the only source of readily available low-energy antiprotons in the world [6]. At this facility, antiprotons can be trapped and controlled in charged particle traps, enabling precision experiments to probe the Standard Model of particle physics.

Low-energy antiprotons could find their application beyond antimatter precision experiments in the field of HCI spectroscopy and metrology. The formation of HCI via antiprotonic annihilation, as described in Sec. 2.3, follows via total or partial electron stripping in an antiprotonic atom. Such a reaction could be engineered inside an ion trap by either mixing antiprotons with positive ions or via charge exchange with negative ions.

Harnessing the potential of HCI formation via antiproton annihilation requires assessing its relevance for the field. For this, we now present hyperfine transition calculations done to select nuclear candidates suitable for this application. The hyperfine splitting wavelengths for hydrogen-like HCIs are calculated for a few isomeric nuclei.

These calculations are restricted to isomeric states, which present advantageous properties for this application. Isomeric states generally exhibit stronger magnetic dipole moments than their ground-state counterparts, leading to a greater hyperfine splitting. Environmental noise decoherence is reduced for larger hyperfine splitting, making them more robust candidates. Additionally, the focus is placed on hyperfine transitions in the infrared regime, which are accessible using laser radiation, facilitating high-precision manipulation with commercially available devices.

3.1.1. Hyperfine Splitting of HCIs

The following calculations were performed adhering to the theory and calculation examples presented in Ref. [55, 64]. The data used for the calculations can be found in Ref. [65].

The hyperfine splitting energy difference E_{HF} for a hydrogen-like ion is, in general, given by [55]

$$E_{\mathrm{HF}} = \frac{\alpha(\alpha Z)^3}{n^3}\frac{\mu}{\mu_{\mathrm{N}} I}\frac{m_e}{m_p}\frac{F(F+1) - I(I+1) - j(j+1)}{2j(j+1)(2l+1)} mc^2 \left[A \cdot (1-\delta)(1-\epsilon) + X_{\mathrm{rad}}\right]. \quad (3.1)$$

Here, α denotes the fine structure constant, c the speed of light in vacuum, and m_{e} and m_{p} the electron and proton masses, respectively. The quantum numbers n, F, j, and l denote the principal quantum number, total atomic angular momentum, the total electronic angular momentum, and the orbital angular momentum, respectively, and μ/μ_N denotes the nuclear magnetic moment for each of the nuclei in units of the nuclear magneton. Here, A denotes a relativistic correction factor, and δ and ϵ are the nuclear charge distribution and nuclear magnetization distribution correction factors, respectively. Lastly, X_{rad} is the radiative correction factor which can be ignored for this application.

The selection of elements computed is restricted to only those heavier than Krypton (Kr) and lighter than Xenon (Xe), as this range is most promising to show full stripping of the atom and obtain a large splitting E_{HF}. Krypton has been shown to be fully stripped, ensuring the formation of a hydrogen-like HCI, whereas, for xenon, only partial stripping has been achieved [63]. Furthermore, as seen from the scaling of Eq. 3.1 with Z, annihilation of elements heavier than Kr can result in HCI fragments with hyperfine splitting wavelengths in the infrared spectrum, allowing for laser spectroscopy. The calculations presented are restricted to elements with a minimum lifetime of 60 minutes. A sufficiently long observation window ensures sufficient stability and the ability to perform multiple measurement cycles.

For a single electron atom at ground state (1s), meaning $s = 1/2$ and $l = 0$, we calculate the energy difference between the $F = I + 1/2$ and $F = I - 1/2$ states. The formula for the energy difference ΔE_{HF} is thus given by the expression previously introduced in Eq. 2.20.

The relativistic correction factor A is given by [55]

$$A = \frac{1}{\gamma(2\gamma - 1)} \quad (3.2)$$

for the 1s state. Here, $\gamma = \sqrt{\kappa^2 - (\alpha Z)^2}$, with $\kappa = (-1)^{j+l+1/2}(j + 1/2)$. For the nuclear charge distribution correction δ, the computation consists of interpolating the simulations outlined in Ref. [55].

The nuclear magnetization distribution correction, oftentimes also referred to as the Bohr-Weisskopf correction, is given by [55]

$$\epsilon = \alpha_S \left[\langle K_S\rangle + \xi\left(\langle K_S\rangle - \langle K_L\rangle\right)\right] + \alpha_L \langle K_L\rangle, \quad (3.3)$$

where α_S and α_L are the fractions of the spin and orbital contributions to the magnetic moment with

$$\langle K_S\rangle = \int_0^\infty K_S(R)|u(R)|^2 R^2 dR, \quad (3.4)$$

$$\langle K_L\rangle = \int_0^\infty K_L(R)|u(R)|^2 R^2 dR, \quad (3.5)$$

where $K_S(R)$ and $K_L(R)$ are integrals for the radial parts of the Dirac wavefunction for the electron and $|u(R)|$ is the radial part of whichever nucleon is odd. For this application, we assume homogenous distribution over the nuclear volume, approximating it as

$$|u(R)|^2 = \frac{3}{R_0^3}\Theta(R_0 - R). \tag{3.6}$$

We assume that the odd nucleon possesses the total nuclear moment, differentiating between three nuclei cases: an odd number of neutrons, an odd number of protons, or an odd number of both protons and neutrons. For nuclei with an even number of protons and an odd number of neutrons, we set $\alpha_S = 1$ and $\alpha_L = 0$, whereas for an odd number of protons and even number of neutrons, these two factors are given by [55]

$$\alpha_S = \frac{g_s(\mu - I)}{\mu(g_s - 1)} \quad , \quad \alpha_L = 1 - \alpha_S. \tag{3.7}$$

Here, g_s is the g-factor for the proton when $|I + 1/2|$ is odd or that of the neutron when it is even. A signed value of I is assigned depending on the parity of the nuclear spin, for example, for a nucleus such as $^{83}Kr^{35+}$ with a reported nuclear spin of $1/2-$, the value is assigned as $I = -1/2$. Similarly ξ is computed for the two cases by

$$\xi = \frac{2I - 1}{4(I + 1)} \quad \text{for } |I + 1/2| \text{ odd}, \tag{3.8}$$

$$\xi = \frac{2I + 3}{4I} \quad \text{for } |I + 1/2| \text{ even}. \tag{3.9}$$

To perform the computations for nuclei with an odd number of both protons and neutrons, we again use Eq. 3.3. The previously outlined computations are done for both cases of $I + 1/2$ being odd or even separately and are then added to compute the total correction factor [64].

After obtaining the energy splitting between the two hyperfine levels, the hyperfine splitting wavelength can then be extracted via the Planck-Einstein relation given by [66]

$$E_{\mathrm{HF}} = \frac{hc}{\lambda_{\mathrm{HF}}}. \tag{3.10}$$

Table 3.1 presents the analytically calculated wavelength $\lambda_{\mathrm{HF}}^{\mathrm{a}}$ for the filtered list of nuclei, including their isomeric excitation energy and half-life. An extension to the presented results can be found in Table A.1, which includes the intermediate results of the correction factors.

Ion	I	μ/μ_N	E (keV)	$t_{1/2}$	$\lambda^{\mathrm{a}}_{\mathrm{HF}}$ (µm)
$^{83}Kr^{35+}$	1/2-	0.5910	42	1.83 h	19.42455
$^{85}Kr^{35+}$	1/2-	0.6320	305	4.48 h	18.16445
$^{82}Rb^{36+}$	5-	1.5096	69	6.47 h	12.51460
$^{85}Sr^{37+}$	1/2-	0.5990	239	67.6 m	16.10615
$^{87}Sr^{37+}$	1/2-	0.6240	388	2.82 h	15.46087
$^{85}Y^{38+}$	9/2+	6.2000	20	4.9 h	2.567061
$^{87}Y^{38+}$	9/2+	6.2400	381	13.4 h	2.550630
$^{90}Y^{38+}$	7+	5.2800	682	3.19 h	3.125522
$^{92}Nb^{40+}$	2+	6.1370	135	10.15 d	1.968983
$^{93}Mo^{41+}$	21/2+	9.9300	2425	6.85 h	1.336406
$^{99}Rh^{44+}$	9/2+	5.6200	65	4.7 h	1.769000
$^{101}Rh^{44+}$	9/2+	5.4300	157	4.34 d	1.830757
$^{102}Rh^{44+}$	6+	4.0100	141	3.74 y	2.540022
$^{106}Ag^{46+}$	6+	3.7040	90	8.3 d	2.374345
$^{108}Ag^{46+}$	6+	3.5800	109	438 y	2.455607
$^{110}Ag^{46+}$	6+	3.6020	118	250 d	2.440786
$^{110}In^{48+}$	2+	4.3650	62	69.1 m	1.529835
$^{114}In^{48+}$	5+	4.6460	190	49.5 d	1.625155
$^{116}Sb^{50+}$	8-	2.5900	383	60.3 m	2.587845
$^{118}Sb^{50+}$	8-	2.3200	250	5.0 h	2.880392
$^{120}Sb^{50+}$	8-	2.3400	0 + x	5.76 d	2.856473
$^{119}Te^{51+}$	11/2-	0.8940	261	4.70 d	6.946341
$^{121}Te^{51+}$	11/2-	0.8950	294	164 d	6.938580

Table 3.1.: Potential isomeric candidates that will result from antiproton annihilation with masses between Kr and Xe, and with lifetime longer than 60 minutes. The candidates are sorted by increasing proton number and neutron number as the second criterion. The nuclear spin I, magnetic moment μ/μ_N, excitation energy E, and half-life $t_{1/2}$, and calculated ground state hyperfine splitting wavelength λ_{HF} for each of the respective hydrogen-like ion is shown. The time units are "m" minutes, "h" hours, "d" days, and "y" years. The calculations are conducted using the nuclear data provided in Ref. [65]. Here, "$0 + x$" refers to an excitation energy above 0 keV but of undefined value.

3.1.2. Shortlisted Candidates and Additional Simulations

The production of most of the isomeric candidates previously presented in Tab. 3.1 is not feasible via beta-decay due to unfavorable decay pathways or extremely short precursor half-lives. In fact, a fast decay precursor would force experimenters to work with highly radioactive samples, as they must be macroscopic. Moreover, the sample would quickly deplete of the interesting component. This sets appealing prospects for utilizing antiproton annihilation as a preferred route for on-demand synthesis of the discussed HCI candidates, offering significant advantages over conventional production methods.

The selection of a list of optimal candidates is narrowed down by assessing their experimental feasibility. As a practical requirement, only isotopes predicted to produce an overall yield of at least 5% in antiproton annihilation reactions are retained for further consideration. The isotope yield from annihilation reactions was simulated by examining nuclear fragmentation of antiprotonic atoms using the Geant4 simulation framework [67–69]. For these simulations, a Penning trap setup such as that of the AEgIS experimental apparatus is assumed for the reactions.

In it, the yield of isomeric nuclei produced from collisions of possible reagent materials with antiprotons was calculated, and only isotopes meeting the trappable yield above 5% criteria were kept for further study.

Additional simulations for the hyperfine splitting wavelength of the candidate HCI species were performed using the GRASP software package [70–72]. The calculated values for the wavelength $\lambda_{\mathrm{HF}}^{\mathrm{GRASP}}$ showed an excellent agreement with the previously presented analytical approach for calculating the wavelength $\lambda_{\mathrm{HF}}^{\mathrm{a}}$, as seen in Table 3.2. All hyperfine excited states presented exhibit lifetimes in the range of $94 - 637$ ms, as calculated via Eq. 22 of Ref. [73], making them suitable for precision spectroscopy applications.

Table 3.2.: Shortlisted candidates from Tab. 3.1 that can be produced and trapped in more than 5% of the annihilation events ("Isotope yield") as simulated using the Geant4 simulation framework [67–69]. The isomeric "product" emerging from the simulated annihilation is reported together with its respective excitation energy E(keV). For each product, a suggested list of precursors ("Reagent") with corresponding "natural abundance". Finally, the transition wavelength of Hyperfine splitting for the Hydrogen-like atom calculated analytically according to Ref. [55] ("$\lambda_{\mathrm{HF}}^{\mathrm{a}}$") and with the GRASP [70–72] software ("$\lambda_{\mathrm{HF}}^{\mathrm{GRASP}}$"). The corresponding lifetimes of the Hyperfine excited states ("Lifetime"), as calculated with Eq. 22 of Ref. [73], are reported.

Product	E (keV)	Reagent	Natural abundance (%)	Isotope yield (%)	$\lambda_{\mathrm{HF}}^{\mathrm{a}}$ (µm)	$\lambda_{\mathrm{HF}}^{\mathrm{GRASP}}$ (µm)	Lifetime (ms)
^{87}Y	381	^{90}Zr	51.45	8.6	2.551	2.544	358.8
		^{89}Y	100	8.9			
^{90}Y	682	^{92}Zr	17.15	7.1	3.126	3.119	637.1
^{92}Nb	135	^{93}Nb	100	9	1.969	1.953	183.7
		^{94}Mo	9.2	5.2			
^{101}Rh	157	^{102}Pd	1	6	1.831	1.814	132.5
		^{103}Rh	100	8.5			
		^{104}Pd	11.14	6.6			
^{102}Rh	141	^{104}Pd	11.14	6.6	2.540	2.513	343.7
		^{103}Rh	100	7.9			
^{114}In	190	^{115}In	95.72	6.86	1.625	1.613	93.7
^{118}Sb	250	^{121}Sb	57.21	5.2	2.880	2.920	540.7
^{120}Sb	0+x	^{121}Sb	57.21	5.2	2.856	2.599	381.4

4. A Transportable Linear Paul Trap for Antiprotons

Having discussed the theoretical contribution of this thesis about HCI that motivates how the fields of nuclear physics, metrology, and low-energy antimatter may benefit from the transport of antiprotons, the focus will now shift to the experimental work conducted during this thesis. This chapter outlines the development, construction, and preliminary tests of a transportable linear Paul trap for ions to be used in low-energy antiproton experiments. Furthermore, the construction of a detection mechanism for antiproton extraction at the AEgIS experiment, alongside the initial attempts at antiproton extraction from the AEgIS experiment for loading low-energy antiprotons into the linear Paul trap, are presented.

4.1. Transportable Paul Trap Design and Assembly

Antimatter is a primary constituent of the Standard Model of particle physics. The fundamental question of baryon asymmetry has puzzled physicists for decades, leading to the development of techniques for conducting precision studies on antiprotons to detect any differences with respect to matter. These experiments can be high-energy, such as studying cosmic rays [74], or low-energy, such as measurements of the antiproton's magnetic moment [7].

The primary challenge for trapping antiprotons at room temperature is their interaction with residual gas molecules in the trapping environment, which even at ultra-high vacuum (UHV), leads to annihilation. However, by trapping antiprotons at higher energies, namely 10s of electronvolts, the rearrangement cross section of antiprotons with surrounding hydrogen molecules may be reduced [52], allowing for room temperature transport. This is the main foundation behind the transportable trap for antiprotons developed during this thesis, which is designed to trap and operate at room temperature. This transportable trap has the primary goal of loading antiprotons and delivering the first experimental result for the annihilation cross section of antiprotons in a room-temperature trap. Additionally, this experiment would aim to deliver the first results of capturing antiprotons and of co-trapping antiprotons with ions in a linear Paul trap. This section provides details regarding the design and reports the construction of the Paul trap worked on during this thesis. Here, both the trap's vacuum components, as well as the exterior devices needed for its function, are outlined. The final experimental apparatus presented has a compact design allowing for operation during transport.

4.1.1. Paul trap Design

The design for the trap follows a linear Paul trap design, such as the one discussed in Section 2.1, consisting of four parallel rod-shaped electrodes with a characteristic distance $r_0 = 1.75\,\mathrm{mm}$. However, so far, the discussion revolving Paul traps has focused on ideal harmonic potentials such as those described in Chapter 2.1. Nevertheless, real-world experimental traps do not exhibit purely quadrupolar potentials. Oftentimes, geometrical constraints and imperfections introduce

anharmonic (higher-order) contributions to the potential. These undesirable contributions to the potential can result in a special form of RF-heating, resulting in the loss of ions [75].

The geometry and design chosen for this particular trap are motivated by Ref. [75]. Here, a few measures are discussed for reducing anharmonicity in the trap's quadrupole potential. The particular choice for the trap's radius r_0 with respect to the RF rod's radius r_e is of particular importance. These two radii, as pictured in Fig. 4.1, are kept in an optimal ratio closer to the ideal quadrupole field when $r_e/r_0 \approx 1.145$, a feature that was implemented in the design of this trap.

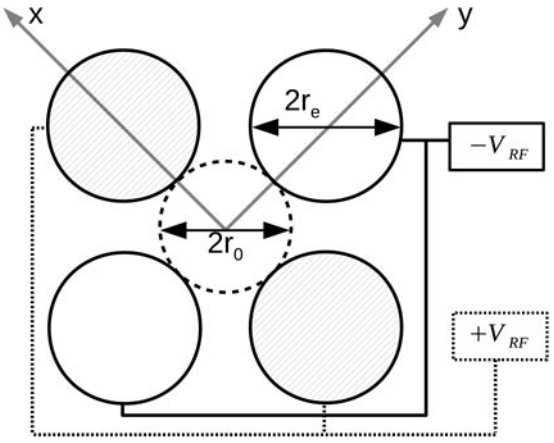

Figure 4.1.: Schematic depiction of a linear four-rod Paul trap as seen from the axial z-axis. The quadrupole potential generated by the four rods can be optimized in real-world experiments by adjusting the radius of the trap r_0 with respect to that of the rod r_e. Optimal conditions are found when the ratio of the two is approximately $r_e/r_0 \approx 1.145$ [75]. Figure taken from Ref. [75].

Two opposing rods provide the trap's oscillating radiofrequency potential, while the other two are found at radio-frequency ground, altogether generating an approximately quadrupolar trapping field radially in the $x-$axis and $y-$axis. Two flat endcap electrodes, shown in Fig. 4.2, provide the axially confining direct-current field, leading to ion confinement along the $z-$axis of the trap. The endcap electrodes feature a circular aperture with a diameter of 3.4 mm along the trapping axis. This aperture in both endcaps allows for the loading of the antiproton beam from the front endcap and the subsequent detection on the opposite side after being released through the back endcap.

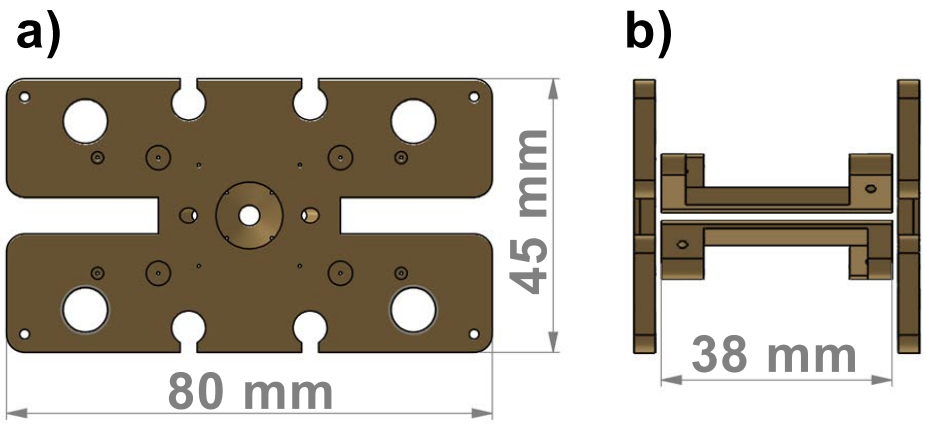

Figure 4.2.: Schematic a) front and b) side view of the trap's electrode configuration. In addition to the four rod electrodes, which provide an approximately quadrupolar radially confining field, the two endcap electrodes on either side provide a confining DC voltage that axially confines the charged particles. Both endcap electrodes feature a circular aperture with a diameter of 3.4 mm aligned with the trapping axis, allowing for loading and detection of antiprotons.

The vacuum chamber hosting the trap is cylindrical. The bases of the cylinder are closed by two ConFlat-200 flanges, and 16 ConFlat-40 openings run along the circular surface. The trap is aligned with two ConFlat-40 openings, one of which has a manual in-line valve that can be opened towards a beamline to load antiprotons into the trap. Two other Conflat-40 openings are connected to the pumps in the chamber. One of the pumps is a non-evaporative getter (NEG) pump (SAES Getters - CapaciTorr Z 400), while the other is an ion-combination pump (SAES Getters - NEXTorr Z 200). The remaining openings are sealed with viewports to be used as optical access for lasers or for image acquisition. The trap is firmly held on the chamber by a modified ConFlat-200 flange with additional ConFlat-16 openings for the feedthroughs of the trap's electrical connections.

The structure holding the trap also holds four metallic targets for ion generation via laser ablation: Barium (Ba), Molybdenum (Mo), Niobium (Nb), and Ytterbium (Yb). On one side of the trap sits the microchannel plate detector (MCP) used for destructive detection of the ions and antiprotons. On the other side sits an Einzel lens which will focus the incoming antiproton beam towards the trap 3.4 mm aperture. The complete schematic layout of the chamber design can be seen in Fig. 4.3.

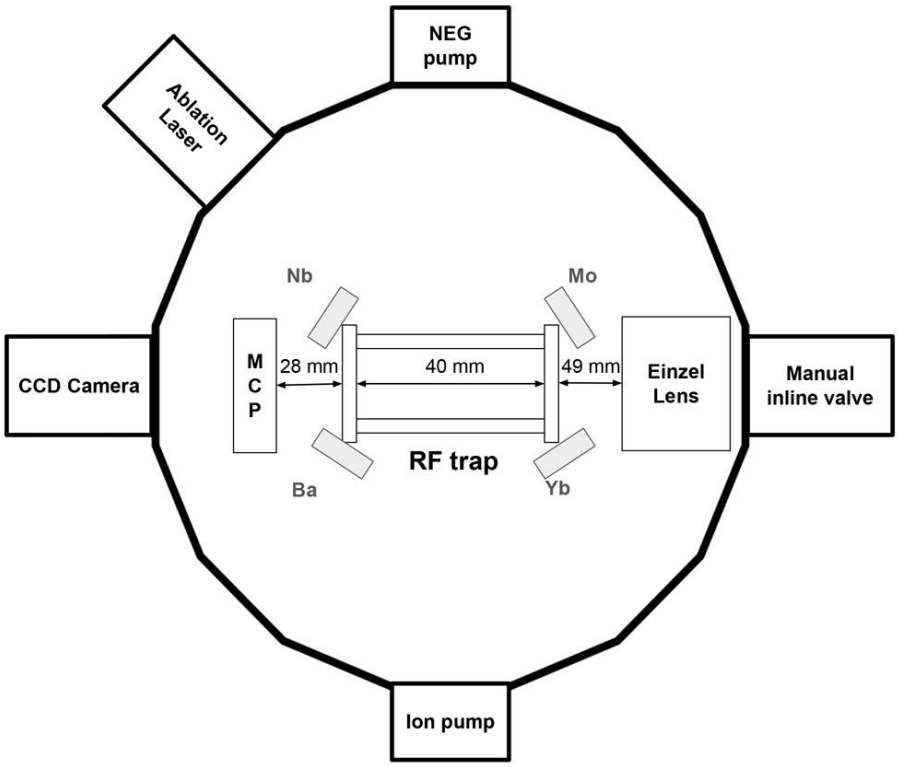

Figure 4.3.: Schematic layout of the trap from a top-down view. The chamber is a 16-sided ConFlat-200 chamber with ConFlat-40 ports on the sides. One of the sides is an entrance port for the antiproton injection and is thus equipped with a manual in-line valve. Two other ports are occupied by an ion-combination (SAES Getters - NEXTorr®Z200) and NEG pump (SAES Getters - CapaciTorr Z 400) to maintain the ultra-high vacuum conditions in the chamber. The remaining openings are sealed with viewports. Two of those are used as optical access for laser ablation and for image acquisition from the MCP detector inside. Inside the chamber, the radio-frequency trap is situated in the center with four metal targets for ablation (Barium, Molybdenum, Niobium, and Ytterbium) around it. Between the trap and the opening to the manual valve, an Einzel lens is positioned to steer the antiprotons into the trap axis.

4.1.2. Trap Assembly

The assembly of the trap was conducted in a room under forced air flow to minimize contamination. Furthermore, during the entire assembly process, clean room suits, hairnets, and masks were worn. All metal pieces in the trap assembly are made of 316L grade stainless steel. Its low outgassing rates [76] make it an optimal material for UHV experiments. Additionally, ceramic components are used for insulation. To further ensure a reliable vacuum, each piece, except for the large ConFlat-200 chamber, was also ultrasonically cleaned in a sequential bath using four solvents, namely acetone, ethanol, isopropanol, and distilled water.

The main interior assembly consists of three sub-assemblies: the linear trap, the Einzel lens corrector, and the MCP detector. The assembly for the linear Paul trap can be seen in Fig. 4.4 and consists of four rods compressed between a front and a back endcap electrode that provide the axial confinement of the trap. The entire trapping assembly is mounted on two pillar structures by four threaded rods. The pillars have screw holes for the trap assembly to be mounted on the main chamber. On the side of the back endcap, an additional deflecting electrode was put in place

to guide the antiprotons towards the MCP during detection. During the experiments reported in this thesis, it was used to confirm the presence of charged particles by changing their impact position on the detector as a result of applying different voltages to the deflecting electrode.

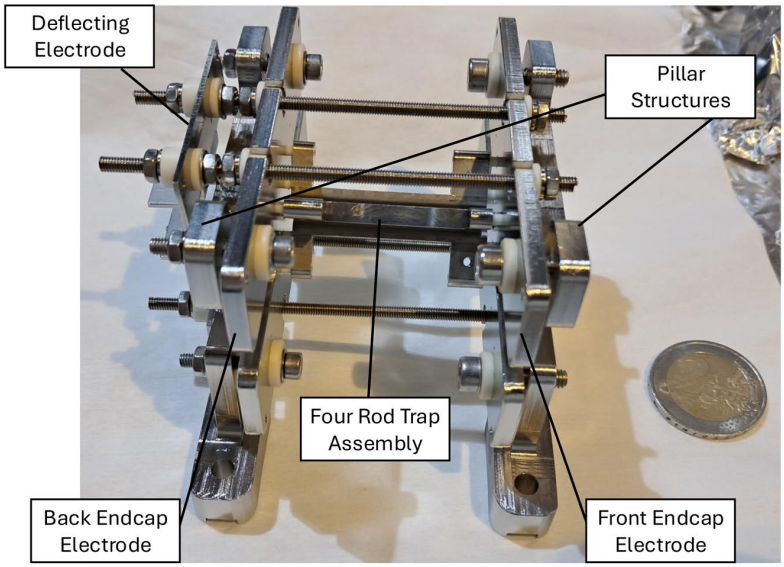

Figure 4.4.: Linear Paul trap assembly with a 2 Euro coin (diameter 25.75 mm [77]) for size comparison. The assembly consists of a four-rod linear Paul trap between two flat endcap electrodes. Antiprotons can be loaded in the trap through the aperture in the "Front Endcap Electrode". On the side of the "Back Endcap Electrode", a deflecting electrode element was put in place to diagnose the charge state of the particles guided. Four threaded rods hold together the endcaps with the four linear rods and secure the trap onto the two pillar structures.

Once the sub-assemblies were put together individually, they were then mounted on a ConFlat-200 customized flange with twelve ConFlat-16 openings for the feedthroughs to power the trap, MCP, and Einzel lens components. The completed flange assembly, including the electrical connections, can be seen in Fig. 4.5. Such a configuration allows for the trajectory correction and loading of the antiproton beam via the Einzel lens corrector for capture in the linear Paul trap. Following this, the captured antiprotons can be sent towards the back by switching the back endcap electrode potential to 0 V and observing the signal on the MCP detector.

The last step of the interior assembly before closing off the trap was installing the four ablation targets (Barium, Molybdenum, Ytterbium, and Niobium) on each corner of the trap assembly. This step had to be done rather quickly due to the fast oxidation of the Barium target. Once the targets were placed, the ConFlat-200 chamber with the ConFlat-40 viewports, in-line valve, and pumps already attached was closed onto the flange. Following the assembly, the trap was placed in an oven, as seen in Fig. 4.6 and baked at 250 °C for one week. After cooling down and turning on the getter and combination pump, the pressure inside the trap was lower than 2×10^{-11}mbar as read by the ion-pump controller (SAES - SIP POWER), confirming the UHV environment inside.

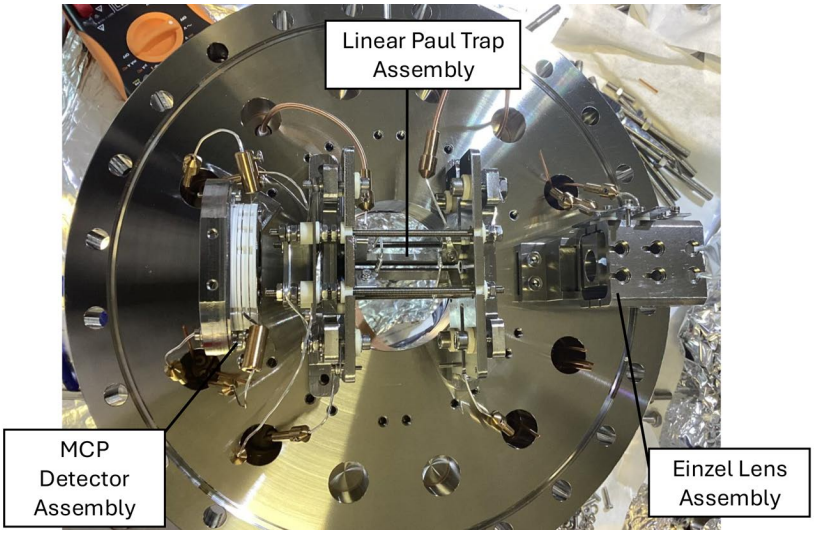

Figure 4.5.: Linear Paul trap assembly on a customized ConFlat-200 flange with twelve ConFlat-16 ports for electrical feedthroughs. The construction consists of three sub-assemblies for the correcting Einzel lens, the linear Paul trap (see Fig. 4.4), and the MCP detector. This configuration allows for loading and correcting the antiproton beam into the linear Paul trap using the Einzel lens and consequent detection by releasing the particles onto the MCP detector by switching off the back endcap potential.

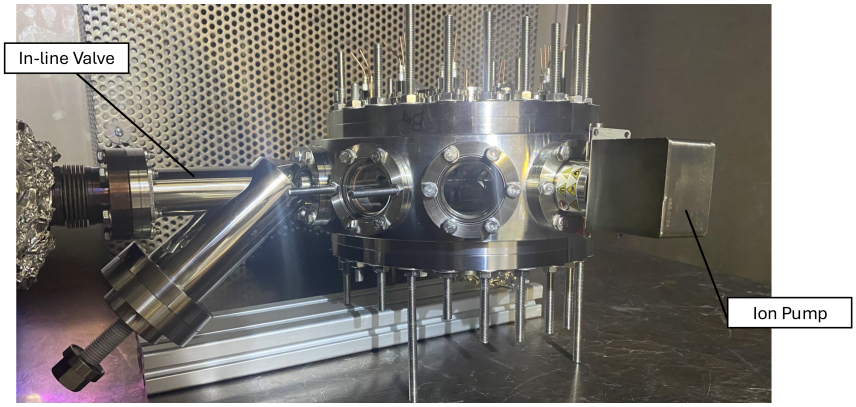

Figure 4.6.: Closed trap chamber inside the oven. The in-line valve is connected to a pumping station located to the left (not pictured), which pumps down the system as the trap is being baked. The trap was baked at 250 °C for one week until reaching a pressure lower than 2×10^{-11}mbar.

4.1.3. Transportable Trap Rack

The vacuum apparatus was assembled on a movable structure that could host all the necessary electronics to enable operation during transport. The structure consists of rack-sized metal construction based on aluminum profiles mounted on wheels. For simplicity, I will refer to this structure as "rack". The rack has several sections for the different electronics needed for the trap's operation. All together, the entire rack has a total height of 180 cm, a width of 61 cm, and a length of 90 cm. A picture of the entire rack containing the trap and electronics can be seen in Fig. 4.7. The trap chamber is mounted on a custom holder, allowing it to be secured onto the rack.

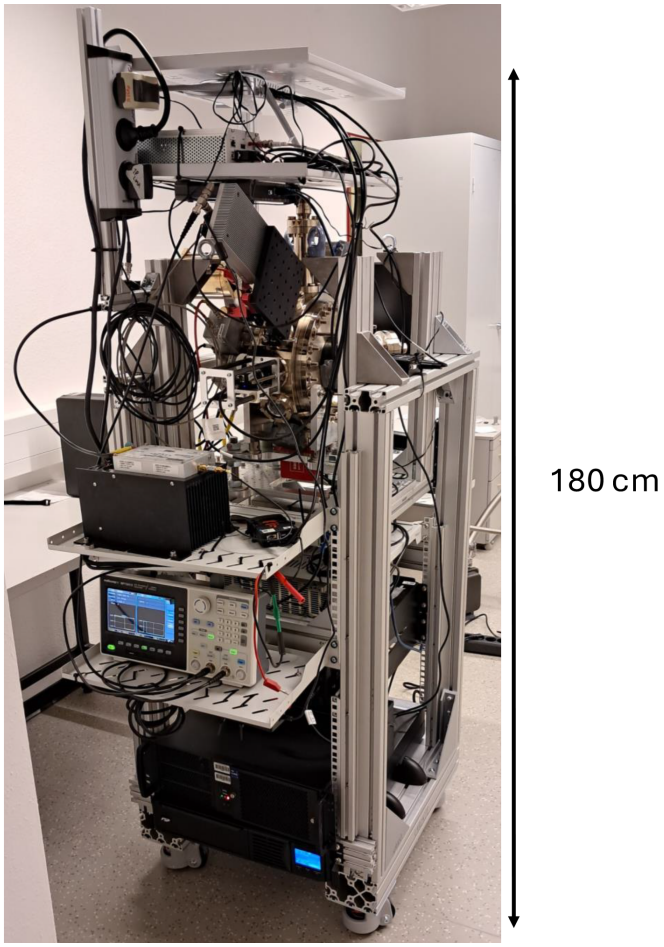

Figure 4.7.: Transportable Paul trap rack. The rack compactly holds the Paul trap chamber and electronics that allow it to operate continuously during transport. This includes the DC high-voltage power supply for the trap endcaps and MCP detector and the RF signal supplied, which is amplified and delivered to the trap via the resonator. The laser ablation system, consisting of a compact optical setup and a function generator, as well as the camera and computer for data acquisition and control of the trap, are also held in the rack.

The power required for the endcap electrodes of the trap and MCP detector is provided to the system by two high-voltage DC power supplies (iseg - EBS EHS F020x and iseg - EHS 40150p). The connection to the MCP detector is direct, while each endcap electrode can be configured to either go through a high-voltage switch (Behlke-HTS 61-01-GSM) or through a low-pass filter. The high-voltage switch allows for nanosecond switching of the endcap voltage between zero and hundreds or thousands of volts. In contrast, the filter allows for a gradual lowering of the potential. The time constant for the low-pass filter used at the endcap was calculated to be a few milliseconds.

The radiofrequency signal for the trap is generated by a Red Pitaya single-board computer, a multifunctional measurement and control tool [78]. The signal goes through an amplifier (Minicircuit - LZY-22+) and is fed into a helical resonator attached to one side of the trap, as seen in Fig. 4.8. The output and the housing of the resonator are further connected to each other via a capacitive voltage divider that allows monitoring the RF signal on the electrodes via an oscilloscope (PicoScope - 3405D MSO). The attenuation factor of the capacitive voltage divider was calculated to be 18.76(3). The resonator boosts the radiofrequency signal and is

used to match the impedance between the amplifier and the trap. The resonance of the full circuit including the trap has a central frequency of 17 MHz and a Q-factor of approximately 170. During the experiment, a maximum peak-to-peak voltage of 600 V was applied.

For capturing the ions or particles detected by the MCP detector inside the trap, a CCD camera (Hikrobot - MV-CU013-A0GM) with an $f = 16$ mm objective is mounted on one side of the trap. The camera is inside an optical enclosure made up of optical blackout material, as shown in Fig. 4.8, in order to minimize the background from exterior light sources. All viewports in the chamber were also covered with additional optical blackout material for the same reason.

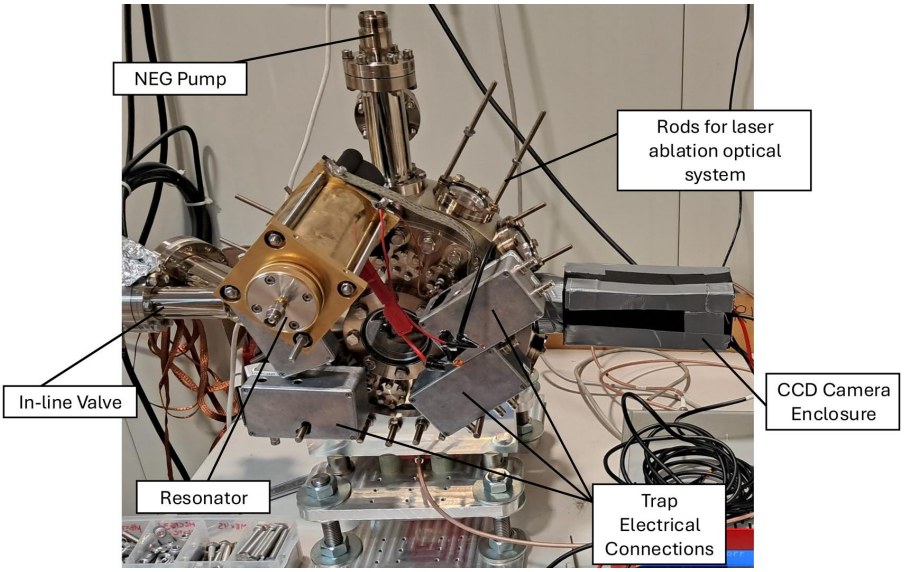

Figure 4.8.: Trap chamber mounted on its stand. A helical resonator is attached on one side to provide the radiofrequency voltage signal coming from the Red Pitaya (not pictured). On the left side of the chamber, there is the in-line valve that is to be attached to the antiproton receiving port, and on the opposite side, the CCD camera, which captures the image from the MCP detector of detected ions or particles inside the trap. Threaded rods were used to secure one of the ConFlat-40 viewports to be able to mount the laser ablation system presented in Fig. 4.9. The electrical connections from the trap are direct Safe High Voltage (SHV) connections to the high voltage power supply in the rack (not pictured). The NEG pump and ion combination pump (below trap chamber, not visible) maintain the UHV environment inside the trap.

The ablation laser system for generating ions inside the trap is attached via threaded rods to one of the viewports of the trap's chamber, as seen in Fig. 4.9. For ablation, a CoboltTor™XS ultra-compact Q-switched diode laser emitting light with a wavelength of 532 nm and a pulse energy of 50 µJ. A Q-switched laser is ideal for material ablation as the short, intense laser pulses are ideal for vaporizing the material with minimal heat spread [79]. The laser beam is focused into the Paul trap through one of the ConFlat-40 viewports around the chamber via a compact optical system. The laser first goes through a convex lens with a focal length $f = 175$ mm and is then reflected and focused into the trap by two mirrors and an additional convex lens with a focal length of $f = 150$ mm. The mirrors are mounted on precision kinematic mounts, allowing for precise adjusting of the laser beam into the desired ablation area.

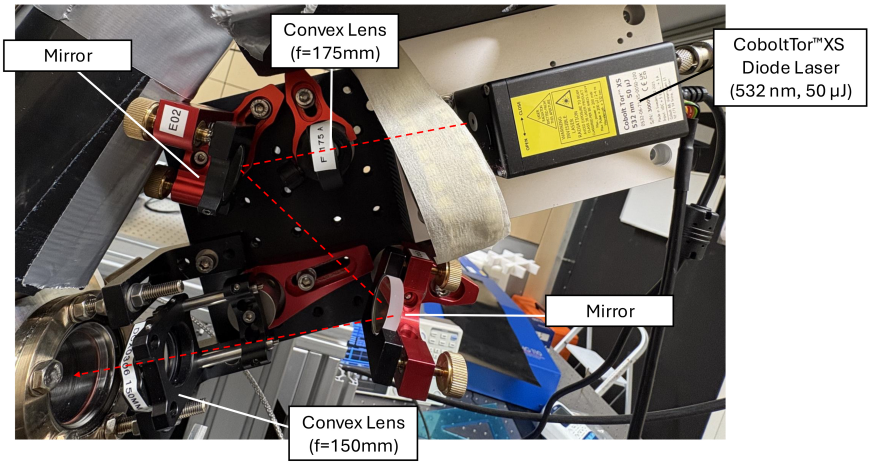

Figure 4.9.: Compact optical system for laser ablation. The 532 nm Q-switched diode laser is sent onto the ConFlat-40 viewport via a convex lens with a focal length of f =175 mm, two adjustable mirrors, and an additional convex lens f =150 mm that focuses the beam into the trap. The pulse trigger for the laser is generated by a function generator (not pictured). The dashed red line represents the trajectory of the laser into the viewport.

All devices in the transportable rack are powered via two Uninterruptible Power Supplies (UPS) secured to the rack. These can be directly connected to the laboratory's power outlet for charging the UPS or for continuous operation of the devices while not running on the battery. The system can be fully powered on battery for approximately two hours. This time is sufficient for all transport operations that are planned at the Antimatter Factory, such as room temperature trapping and short-distance transport of antiprotons. If a longer transport time is required, the UPS units can be reconnected to a power supply inside a transporting vehicle.

4.2. Transportable Paul trap Testing and Characterization

The transport of antiprotons away from CERN's Antimatter Factory facilities to other laboratories would open the doors for many experiments beyond what is currently available with antimatter today. The linear Paul trap developed during this thesis aims to achieve the transport of antiprotons at room temperature. Before attempting to extract and trap antiprotons, however, the system was first tested to demonstrate its ability to reliably trap and transport ions.

The transportable Paul trap features four metal targets inside (Ba, Yb, Mo, Nb), allowing for loading ions into the trap via laser ablation. While loading of these ions was not yet achieved in the trap, ablation of the flat endcap electrodes generated ions in the trap, which were used for experimentation. The unidentified ion species produced via ablation of the stainless steel endcap electrode was used for initial transport tests of the trap to verify its transportability while in operation. Furthermore, these ions were used to characterize the trapping parameters of the trap and to optimize the trap's lifetime configuration.

This chapter outlines the image and video processing steps for analyzing the data acquired by the CCD camera in the setup. Videos and images of the ions detected by the MCP detector are presented, and the procedure to extract the number of ions for each measurement is laid out in detail.

Here, the first storage time characterization results for the trap with the unidentified ions produced via laser ablation of the stainless steel flat endcaps of the linear Paul trap are presented.

The storage time characterization results are presented for different configurations of the endcap voltages to determine the impact of different electrical circuits on the ions' storage time for catching and storing antiprotons.

The operation of loading antiprotons into the trap will follow a ballistic procedure, in which antiprotons will be guided in a beamline from the main trap of the AEgIS experiment into the portable trap. The ballistic transfer requires acceleration of antiprotons out of the primary trap and subsequent deceleration in the portable trap. The deceleration will be realized by adapting the reference ground of several electronic components to be raised to several hundreds of Volts to match the kinetic energy of the incoming antiprotons during the ballistic transfer. This strategy was chosen over the employment of degrader foils or drift tubes, with which a large part of the antiprotons may be lost to annihilation [6]. For this reason, the functionality of the trap was, in addition, tested while floating the reference ground of the Paul trap to 500 V by measuring the storage time of the ions.

Furthermore, the first results of ion transport are presented. This work involved the transport of the trap inside a van during operation while loaded with ions. Here, the best results during the transport procedure are presented, where approximately several tens of ions were detected after 15 min of driving a distance of 18.6 km with the loaded ion trap.

Lastly, an error discussion of the ion measurements is presented. The different sources of error and their impact on the ion count are outlined and compared to determine the most influential sources. These errors include, but are not limited to, uncertainties from the image background noise, systematic errors from the analysis, and the MCP detector's inherent uncertainty.

4.2.1. Ion Signal Measurement Procedure

GIO ARRIVED HERE, DO NOT REMOVE THIS COMMENT. *Figure exchange?*[gio]

In this section, the experimental procedure for performing measurements of ion storage in the trap is described. Firstly, the Red Pitaya used as an RF generator and the signal amplifier are switched on. The proprietary software for the PicoScope oscilloscope is used to monitor the signal during the measurements. The delivered radiofrequency signal is shown against the reflected signal coming back from the trap. The RF generator is set to deliver a signal with a peak-to-peak amplitude of $V_{\mathrm{RF}} = 600\,\mathrm{V}$ and a frequency of 17.1 MHz to the trap's radiofrequency rod-shaped electrodes. A schematic depiction of the full experimental setup is shown in Fig. 4.10.

Following the powering of the radiofrequency signal, the front endcap is switched on to $V_{\mathrm{F}} = 1\,\mathrm{kV}$ and the back endcap is powered on but kept at $V_{\mathrm{B}} = 0\,\mathrm{V}$. Once the trap system is powered up and all parameters are set, the measurement procedure starts by aligning the ablation laser and confirming ion ablation of the endcap electrode in the trap. For this, the detection system, namely the MCP detector and camera, is powered on. The MCP detector's in-electrode, out-electrode, and phosphor screen are switched on to $V_{\mathrm{IN}} = -700\,\mathrm{V}$, $V_{\mathrm{OUT}} = 0\,\mathrm{V}$, and $V_{\mathrm{S}} = 3\,\mathrm{kV}$ respectively. The CCD camera is set to continuous acquisition mode with a gain of 16.37 dB and an exposure time of 100 ms to visually confirm the ablation upon detection of the ions. A sample for a captured triggered image of an ion detection event of the MCP detector can be seen in Fig. 4.11. This image was used for dimension calibration of posterior measurements, as the diameter of the MCP is known to be 25 mm. For reference, the phosphor screen of the MCP used for the measurements is of type a P43 phosphor, which has a response time of about 1 ms.

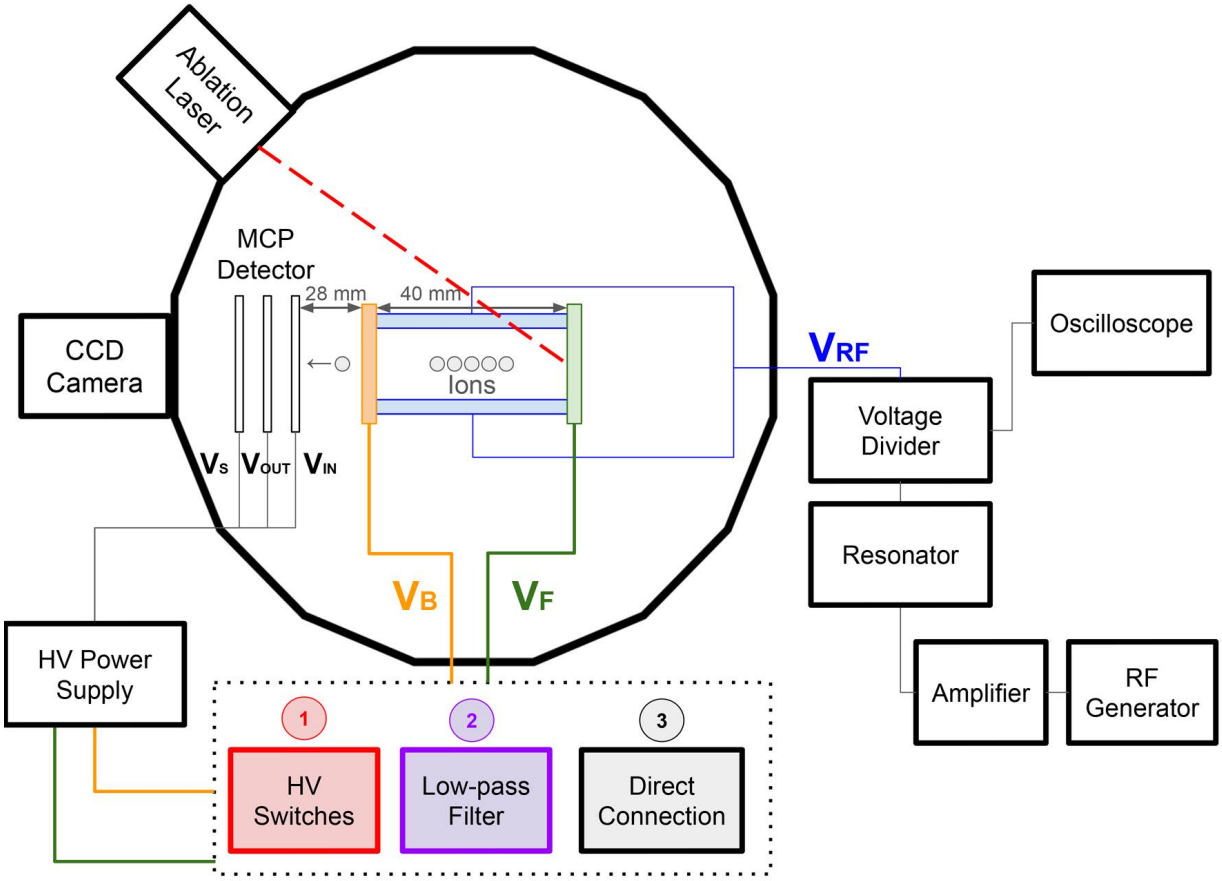

Figure 4.10.: Schematic depiction of the experimental setup and relevant voltages. The generation, trapping, and subsequent detection of ions begins by switching on the RF and DC electrodes of the trap. The delivered RF signal after the resonator, amplifier, and voltage divider has a voltage of $V_{\mathrm{RF}} = 600\,\mathrm{V}$ with a frequency of 17.1 MHz. During the measurements, the signal is monitored via an oscilloscope. The DC front and back endcap voltages are set to $V_{\mathrm{F}} = 1\,\mathrm{kV}$ and $V_{\mathrm{B}} = 1\,\mathrm{kV}$. These voltages are delivered from the power supply, passing through either high voltage switches, low-pass filters, or directly connected, depending on the desired configuration. Ions are loaded into the set trap by switching on the ablation laser, which is triggered to produce 10 pulses with a frequency of 33.3 Hz. The trapped ions are then sent to the detector by switching off the back endcap electrode. Detection of the ions then follows via the MCP detector which has its in-, out-electrode and screen set to $V_{\mathrm{IN}} = [-700, -1300]$ V (depending on the experiment), $V_{\mathrm{OUT}} = 0\,\mathrm{V}$, and $V_{\mathrm{S}} = 3\,\mathrm{kV}$ respectively. An image or video of the detection event is consequently captured by the CCD camera (see Fig. 4.11).

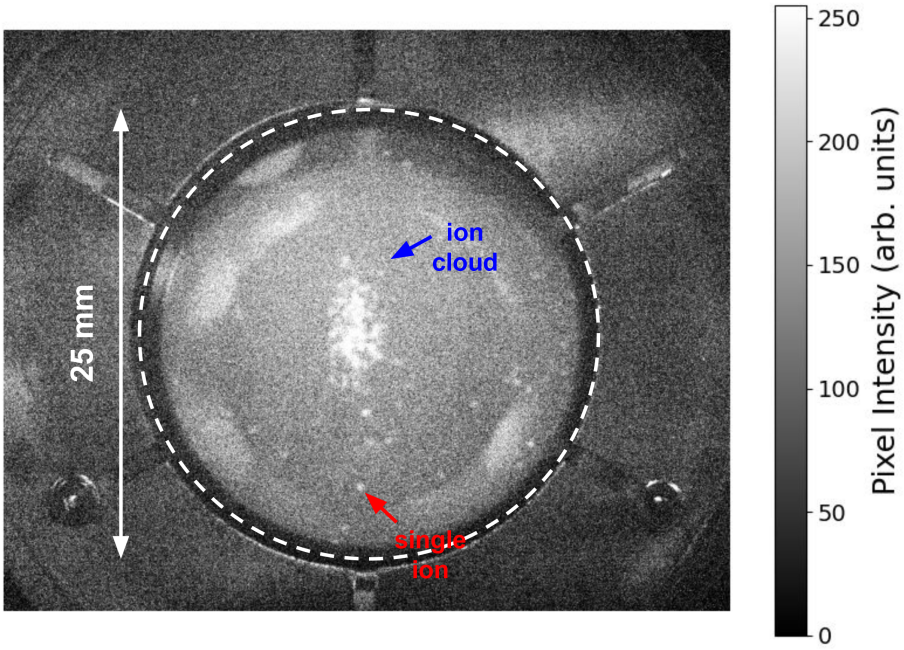

Figure 4.11.: Single image captured by the CCD camera set in trigger mode with a gain 16.37 dB and an exposure time 1 s. The trigger of the camera and high-voltage switch at the back endcap electrode is accordingly timed to capture the cloud of ions arriving at the MCP detector after being ejected from the trap. The resulting image is a dense ion cloud focused towards the center of the MCP detector with voltages on the in electrode of $V_{\mathrm{IN}} = -1.3\,\mathrm{kV}$, the out-electrode at $V_{\mathrm{OUT}} = 0\,\mathrm{V}$, and the phosphor screen at $V_{\mathrm{S}} = 3\,\mathrm{kV}$.

The ablation laser is triggered to produce 10 pulses with a frequency of 33.3 Hz. By triggering and carefully adjusting the laser with the rotatable mirror mounts, the signal of the ions hitting the MCP detector is captured and adjusted until an ion signal is captured by the camera. The detected ions appear on the camera as a bright spot directed towards the center of the MCP detector. One such picture of the ablated unidentified ions hitting the MCP detector and being captured by the camera can be seen in Fig. 4.12. Once ablation is confirmed, the back endcap electrode of the trap can be switched on to 1 kV, fully closing the trap. The optimization procedure for finding the optimal trapping voltages mentioned here is described in Sec. 4.2.2.

Measurements of the unidentified ion species inside the trap are then performed by loading ions by triggering the laser into the fully closed trap. Following ion generation and trapping, ions are released towards the MCP detector by lowering the back endcap voltage. This procedure can be done by either lowering the voltage on the control software for the high-voltage power supply or by triggering the high-voltage switches, which lower the voltage of the endcap electrode to 0 V in about 0.3 µs. Approximately thirty seconds before releasing the ions towards the MCP detector, the detector's in-electrode voltage is adjusted to $V_{\mathrm{IN}} = -1.3\,\mathrm{kV}$ to accelerate the ions towards the detector and increase the gain of the MCP detector that amplifies the signal up to single particle sensitivity. This voltage is not kept constant to avoid damaging the MCP detector and is tuned back up to $V_{\mathrm{IN}} = -700\,\mathrm{V}$ after the detection is performed.

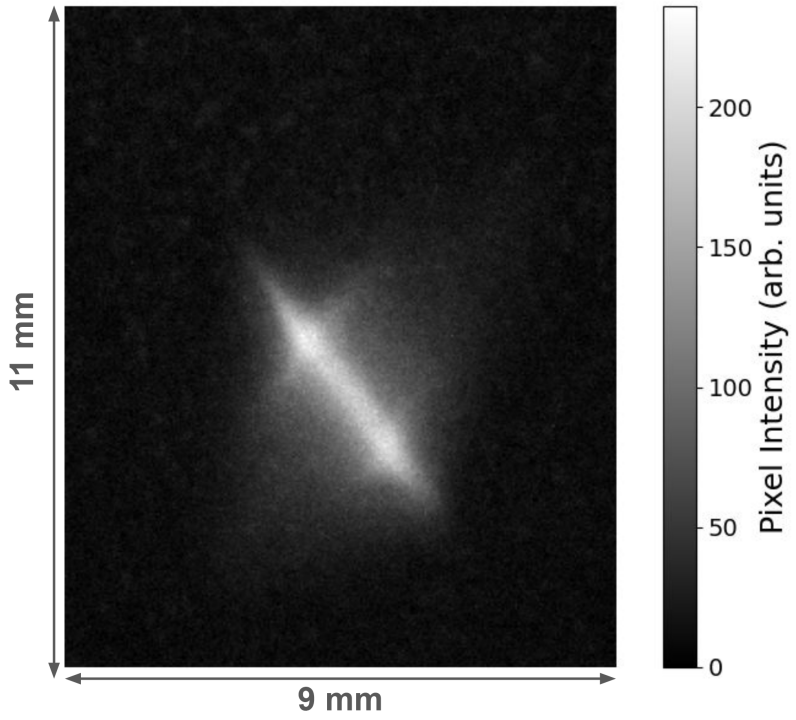

Figure 4.12.: Single image captured of the laser ablation signal on the MCP detector. An unidentified species of ions is generated by laser ablation of the flat stainless steel endcaps inside the trap. The ion signal appears as a tilted, ellipse-shaped bright spot on the MCP detector of the trap. This image is captured with the RF signal of the Paul trap switched on and the back endcap of the trap at 0 V. The CCD camera was set to a gain 16.37 dB and an exposure time 100 ms.

4.2.2. Optimization of Trapping Parameters

Measurements were performed to determine optimal trapping voltages of the RF rod and the DC front and back endcap electrodes. Firstly, the mean intensity of destructive ion detection events is measured for different RF readings of the oscilloscope. For this, the input RF signal at the Red Pitaya was adjusted, and the corresponding delivered RF voltage to the trap V_{RF} was noted. The trap was loaded as per the standard voltage configuration, and after a storage time of 20 s, the ions were released onto the MCP detector via triggering of the high voltage switch. A single image of the MCP's phosphor screen was captured via the CCD camera in trigger mode.

The performed RF voltage scan can be seen in Fig. 4.13. The mean intensity for each ion cloud detection event was recorded for several values of the input peak-to-peak RF voltage V_{RF}. The mean intensity signal grows with the RF voltage but is shown to largely plateau after reaching a voltage of $V_{\mathrm{RF}} \approx 600\,\mathrm{V}$. For this reason, the RF voltage delivered to the trap was kept approximately at the value during the course of the measurements. Nevertheless, the peak-to-peak voltage delivered was shown to fluctuate heavily. The impact of this drift on the measurements is discussed in Sec. 4.2.6.

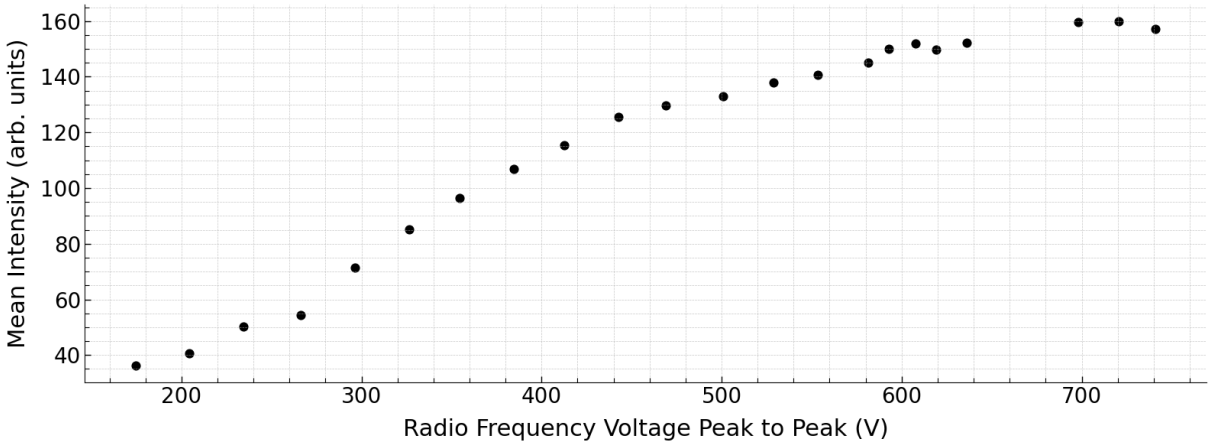

Figure 4.13.: Voltage scan measurements of the RF rod electrodes voltage V_{RF}. A triggered single-image acquisition of the MCP detector is performed after ejecting the trapped ions via the HV switch after 20 s of storage. The mean intensity of the acquired image is then recorded for several values of the RF voltage V_{RF}. It was determined that the ion signal begins to plateau at approximately $V_{\mathrm{RF}} = 600\,\mathrm{V}$, which was chosen as the desired RF peak-to-peak voltage.

An analogous voltage scan was performed for the endcap voltages V_{F} and V_{B}, which axially close the trap. For this, antiprotons were loaded into the trap at different set endcap voltages. Clarifying that by set voltage, the voltage input value on the power supply software is meant. After 20 s of storage inside the trap, the ions are ejected by lowering the back endcap voltage V_B to 0 V by triggering the high-voltage switch. The ion cloud detection event is captured for each set voltage by triggering a single image acquisition by the CCD camera. The mean ion intensity is calculated for each endcap voltage set and can be seen in Fig 4.14. From this measurement, it was determined that the mean intensity plateaus for the endcap voltages close to 1 kV, which was determined as the optimal value for trapping experiments.

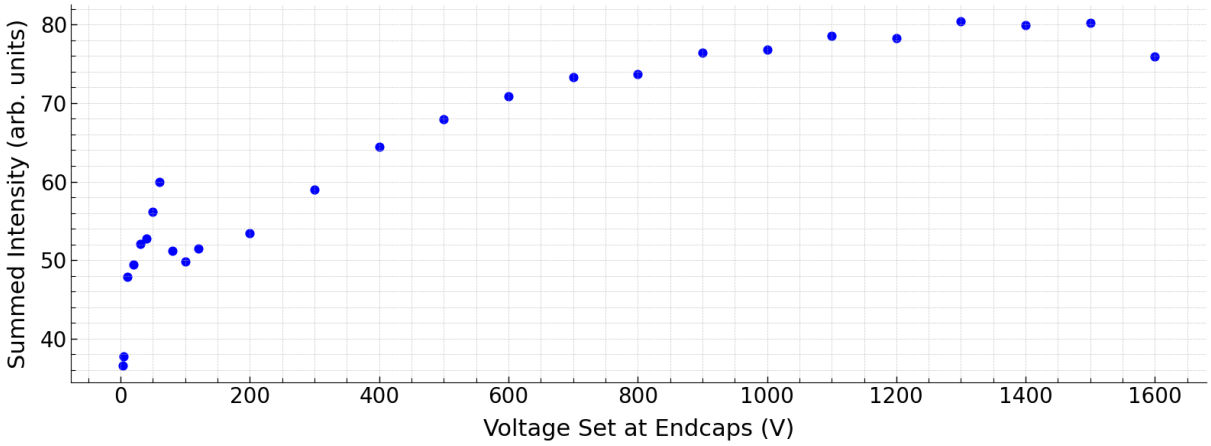

Figure 4.14.: Voltage scan measurements of the DC endcap electrodes voltages V_{F} and V_{B}. A triggered single-image acquisition of the MCP detector is performed after ejecting the trapped ions via the HV switch after 20 s of storage. The summed intensity of the acquired image is then recorded for several values of the voltage set for both endcap electrodes V_{F} and V_{B}. The summed intensity of the acquired images begins to plateau after setting the endcap voltages to 1 kV, which was the parameter chosen for trapping and transport procedures.

4.2.3. Ion Number Video Analysis

Capturing the image of the trapped ions with a CCD camera can be done in either the form of a picture or a video. For a picture, the ejection of the ions from the trap, i.e., lowering of the back endcap electrode potential, must be accordingly timed with the image capture. This can be achieved by using a high-voltage switch that lowers the endcap voltage down to $V_B = 0\,V$ within approximately 0.3 µs, which is the measured switching transient time of the device. This time can be considered effectively instantaneous for the trapped ions. For example, an antiproton with a kinetic energy of about 10 eV travels approximately 13 mm in 0.3 µs, whereas the trap is 40 mm long. By timing the trigger of the switching with that of the image capture of the camera and adjusting the exposure time of the camera accordingly, one can capture single images of ions ejected from the trap.

Alternatively, the voltage at the endcap can be lowered with the power supply software, and a video of the gradual ejection of the ions from the trap can be captured as the voltage lowers. Lowering the voltage with the power supply can take several seconds and is, thus, much slower than what is achieved by using the switch. An example of the gradual ejection and detection of ions can be seen in Fig. 4.15. For this and the following image processing steps, the example of measurements taken for ions stored for 3 min in the trap and ejected with the low-pass filter on the back endcap will be used. Here, ions were ejected towards the MCP detector by switching the voltage of the back endcap to V_B 0 V on the high-voltage power supply control software. Gradual ejection of the ions then follows by the gradual lowering of the voltage at the power supply and further damping by the low-pass filter connected to the endcap electrode. Ions typically begin to exit the trap when the voltage shown on the high-voltage power supply controller software reads a few Volts. This was found to happen approximately 20 s after lowering the voltage of the back endcap V_B from 1 kV down to 0 V.

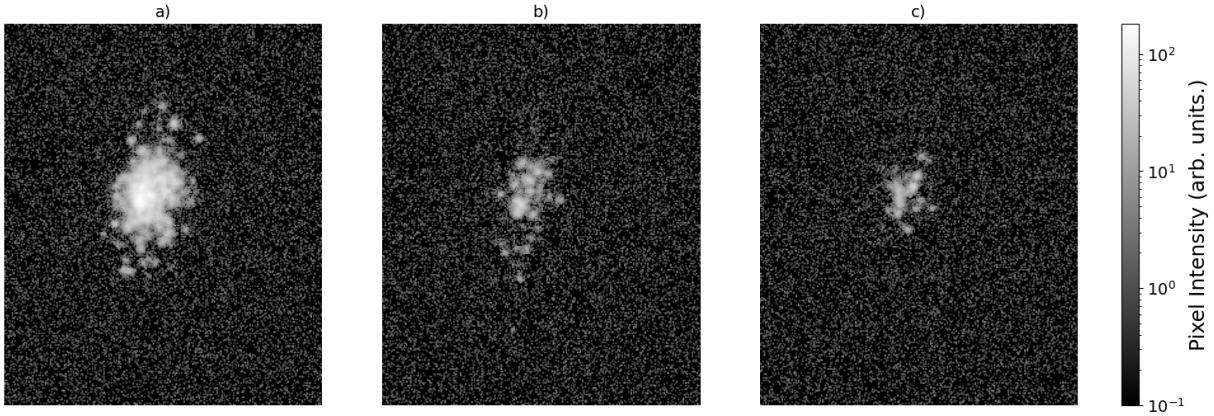

Figure 4.15.: First (a), second (b), and third (c) key frames in a sample video acquisition of detected ions captured by the camera (with a gain 16.37 dB and an exposure time 100 ms). The back endcap electrode was connected to the high-voltage power supply by a low-pass filter (time constant of approximately a few milliseconds), and the voltage of the endcap was ramped down to V_B =0 V to release the ions into the MCP detector. The frames for the video were taken after ions had been stored for 3 min inside the trap.

The analysis of the recorded videos is followed by determining the key frames in which ions were detected. This is done by first selecting a region of interest in the video centered on the MCP detector's active area in the frame. The total size for each video frame spans a height of 1024 px and a width of 1280 px. The region of interest was cropped down to a height of 300 px and

a width of 250 px corresponding to a physical size of 11 mm by 9 mm to exclude regions outside the MCP detector's active area.

Following the selection of the region of interest, the mean intensity of the selected region is evaluated using Python's *Pillow* image processing library. This is done for each frame in the video, and is then plotted against the frame number in the video. The mean intensity per frame for the measurement performed using the low-pass filter after 3 min of storage can be seen in Fig. 4.16. From this, the frames to be evaluated for each ion detection event are determined. This process was done manually for each video, considering the mean intensity per frame as well as visually analyzing the video itself. Once the frames containing ions from each video are determined, each of these frames is extracted into individual Tagged Image File Format (.TIF) image files.

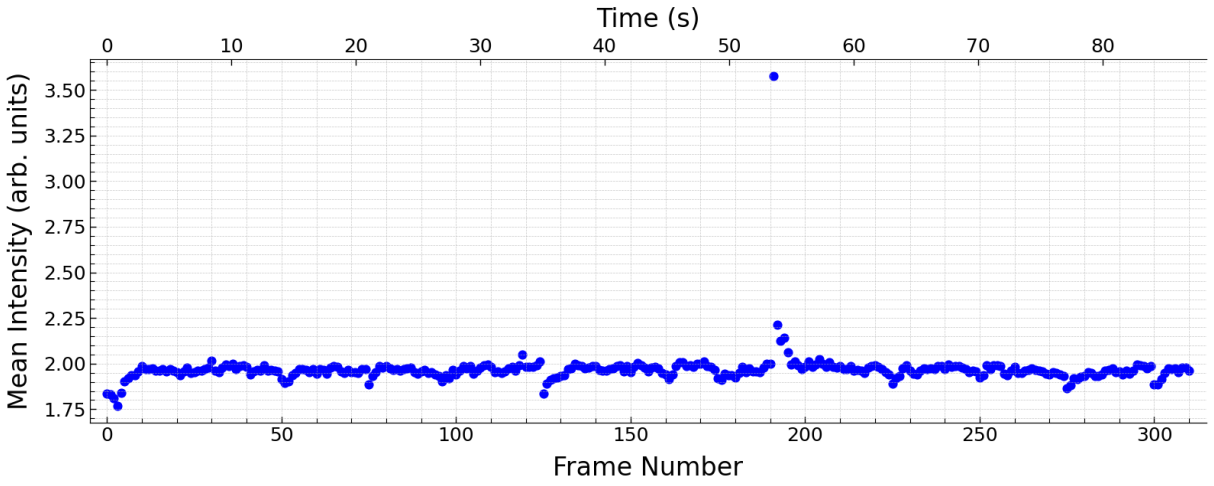

Figure 4.16.: Mean intensity per frame in video of MCP detector during ejection of ions after 3 min of storage inside the trap. The ejection was done by lowering the back endcap of the trap, which was connected to a lowpass filter. The ion detection event begins at frame number 191, where a spike of the captured mean intensity occurs.

Consequently, a background image for each video is generated by averaging the intensity at each pixel for typically the first 100 frames in the video where no ions are present. For shorter videos, fewer frames could be taken. Once a reference background frame for each video was generated, the average background intensity at each background pixel I_0 was subtracted from the intensity of each pixel in the identified frames with ions. An example of the background-subtracted frame for the measurement performed after 3 min of storage is presented in Fig. 4.17.

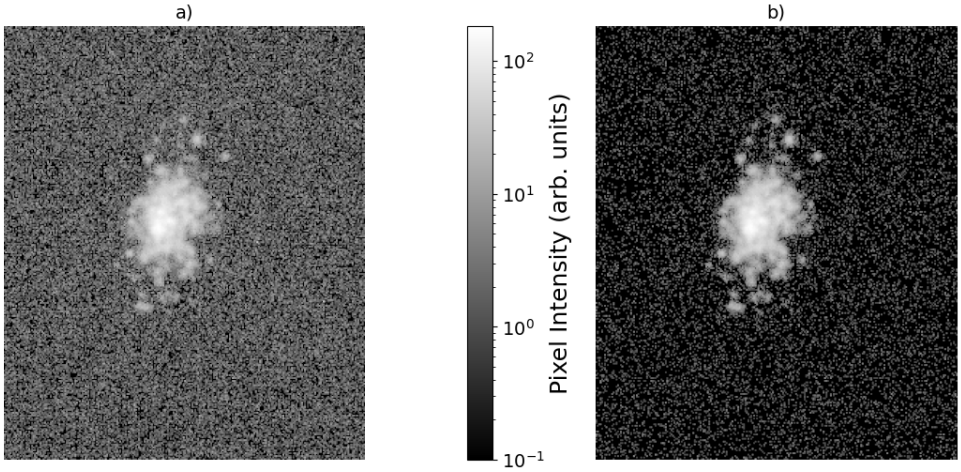

Figure 4.17.: Raw (a) and corrected (b) images of the region of interest for a frame of a measurement video taken after 3 min of storage in the trap. The background reduction was done by taking a background sample of 100 frames without ions present and averaging the intensity at each pixel. This background is subtracted from the raw image to produce a background-reduced corrected image. The intensity map scale is presented logarithmically to improve the contrast and aid in the visualization of the subtracted background.

After having determined the key frames for each ion detection event, determining a region of interest, and subtracting the background, the total intensity for each frame of the measurement is determined. This is again evaluated using Python's *Pillow* library for image processing. The same procedure was used to determine the intensity of a single ion in order to use it as a calibration factor for the number of ions.

The efficiency of electron-photon conversion of the MCP detector is not constant and may vary between detected ions. This is of particular importance when trying to estimate the intensity of a single ion; for this reason, a statistical analysis over several single-ion samples was conducted. A total of 15 single ions were manually selected, as presented in Fig. 4.18. These ions were extracted from the evaluated frames, and the mean intensity of each single ion was determined. The region selected for each single ion was kept constant to 5×5 px in order to minimize fluctuations due to the background. The intensity values of each pixel in the 5×5 px single ion capture were summed to obtain the total intensity expected of each ion. The expected mean intensity for a single ion was then determined by averaging the single ion intensity for the 15 samples and was found to be $I_{\text{ion}} = 353(17)$.

The number of ions found in each measurement can then be found by summing over the total intensity for each analyzed frame and dividing by the average mean intensity of a single ion. The image processing calculation for determining the number of ions, including the background subtraction, is thus given by

$$N = \frac{1}{I_{\text{ion}}} \left(\sum_{f=f_i}^{f_e} I_f - I_0 \right), \tag{4.1}$$

where I_f is the intensity per frame number f, and f_i and f_e are the initial and end frame numbers determined for each measurement.

The statistical uncertainty for the number of ions σ_N is estimated via the uncertainty of the single-ion average σ_{ion} given by the standard error of the mean, as estimated via error propagation

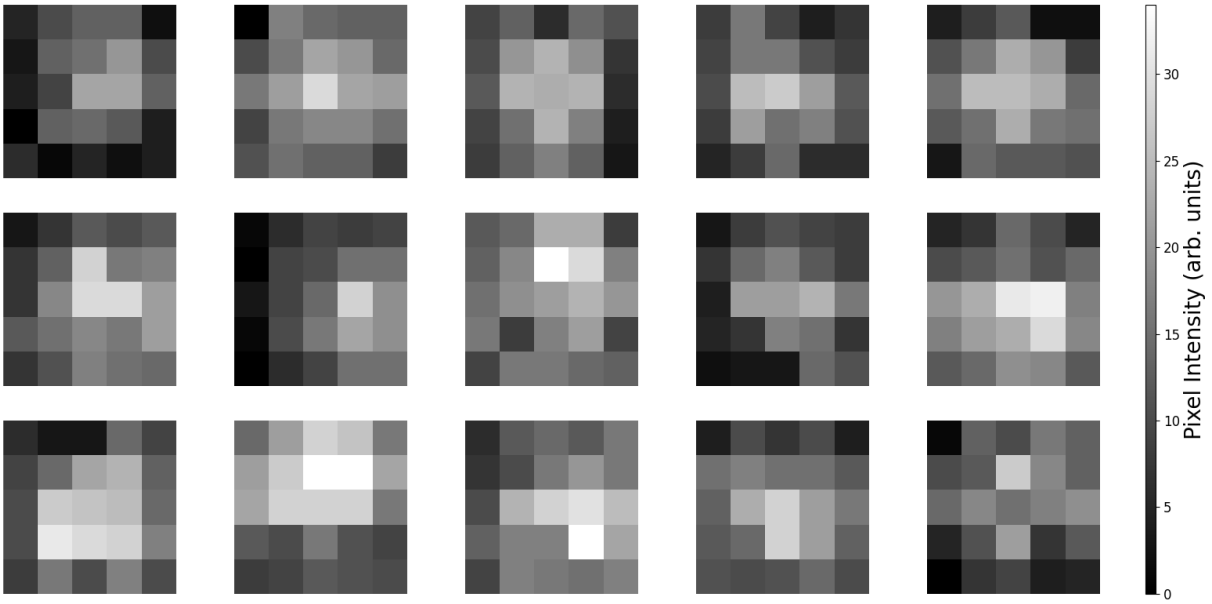

Figure 4.18.: Fifteen single ion detection events manually selected and cropped to a 5×5 px square. For each manually selected ion, the total signal intensity was measured by summing all the pixel values. These intensities were then averaged to calculate the expected signal from a single ion, which was found to be $I_{\text{ion}} = 353(17)$.

to be

$$\sigma_N \approx \frac{N \cdot \sigma_{\text{ion}}}{I_{\text{ion}}}. \tag{4.2}$$

This gives, however, only an approximation for the statistical uncertainty of the measurement. Further uncertainties and sources of error are discussed in Sec. 4.2.6.

4.2.4. Paul Trap Storage Time Characterization

The storage time of the unidentified ions was measured under different conditions. Here, the results for the storage time of ions for different endcap electrode ion release conditions are investigated. The effect of lowering the voltage, with and without the low-pass filter, is compared to that of triggering the release of ions via the high-voltage switch. Furthermore, the functionality of the trap while operating at a floated ground of 500 V is evaluated, and the storage time of the ions in such a configuration is measured.

For both of the performed sets of measurements, ions were loaded by ablation of the endcap electrode into the closed trap. The ions stay inside the trap for the desired storage time until they are released either by setting the high-voltage power supply input to the back endcap electrode to 0 V or by triggering the high-voltage switch. Thus, the storage time in the trap is counted as the time between the triggering of the laser for ablation and the time of switching down the voltage. The ion release is recorded by the CCD camera in the form of a video to be analyzed frame by frame as outlined in Sec. 4.2.3, extracting the total number of ions obtained in each measurement.

The total number of ions obtained for each measurement is plotted against the time the ions were stored inside the trap for that particular measurement. The storage time of ions in a Paul trap is defined as the time it takes for the number of ions in the trap to decrease to $1/e$ of the

original number [80]. Thus, the storage time of the ions can be extracted by fitting the obtained data with an exponential decay function for the number of ions $N(t)$ of the form

$$N(t) = N_0 \cdot e^{-t/\tau} + C, \tag{4.3}$$

where N_0 is the initial number of ions, τ the storage time of the ions, and C an offset due to the background which is further elaborated on in Sec. 4.2.6. From this analysis, the storage time of the ions in the trap for the different configurations can be evaluated and compared.

The mechanism used for lowering the back endcap voltage V_B from 1 kV down to 0 V to release the ions onto the MCP detector was determined to impact the number of ions and storage times of ions trapped. When connecting the endcap electrodes directly to the high voltage power supply and lowering the voltage of the back endcap electrode on the control software, the ions were shown to have a corresponding storage time of 74(7) s with an initial ion count of $7.4(6) \times 10^2$ ions. The initial ion count and storage time were improved when evaluating the measurements using the high-voltage switch to lower the voltage, presenting a storage time of 61(3) s and an ion count of $3.4(2) \times 10^3$ ions. For the measurements taken with the low-pass filter connected to the endcap electrodes, the storage time of the ions was further improved to 94(5) s with a corresponding initial ion count of $1.81(9) \times 10^3$ ions.

The functionality of the trap was tested during floating of its ground to 500 V by measuring the storage time of the ions for up to 7 min and lowering the back-endcap voltage V_B with the low-pass filter attached. A reduction in the initial ion count was observed with only $6(2) \times 10^2$ ions. Similarly, the evaluated storage time of 23(9) s was reduced in comparison to when using the low-pass filter without floating the ground of the trap.

Ion Storage Time Electrode Configurations

In order to determine the optimal configuration of the trap to prolong the storage time of the ions, the storage time was measured for different lowering configurations of the trap's back endcap voltage. Three sets of storage time measurements were performed, firstly for ions released via triggering of the high voltage switch connected to the back endcap voltage, and then for the lowering of the voltage from the high-voltage power supply controller, once with a direct connection to the endcaps and once with the low-pass filter in between.

The number of ions per time stored in the trap was measured for the three endcap voltage configurations by taking a video of the ion event on the MCP detector after waiting a set storage time. This measurement was performed for storage times between 20 s and 20 min for all three configurations. The number of ions per time stored inside the trap was extracted from each video by using the video analysis process outlined in Sec. 4.2.3. From this, the measurements were plotted for all three data sets as seen in Fig. 4.19. Each set of data was fitted with an exponential decay function of the number of ions in the trap according to the model expressed in Eq. 4.3. From this, the storage time of the ions τ was determined to be 74(7) s in the case of a direct connection between the back endcap and the power supply, 61(3) s for the release of the ions through the triggering of the high-voltage switches, and 94(5) s for a connection to the endcap through the low-pass filter.

The measured storage times for the different configurations indicate some noise is likely being introduced into the voltages of the endcaps. The low-pass filter may be filtering some of the noise in the endcap voltages, leading to an improvement of approximately 50% and 30% over the lifetime of the measurements performed with a direct connection and with the high-voltage switches accordingly.

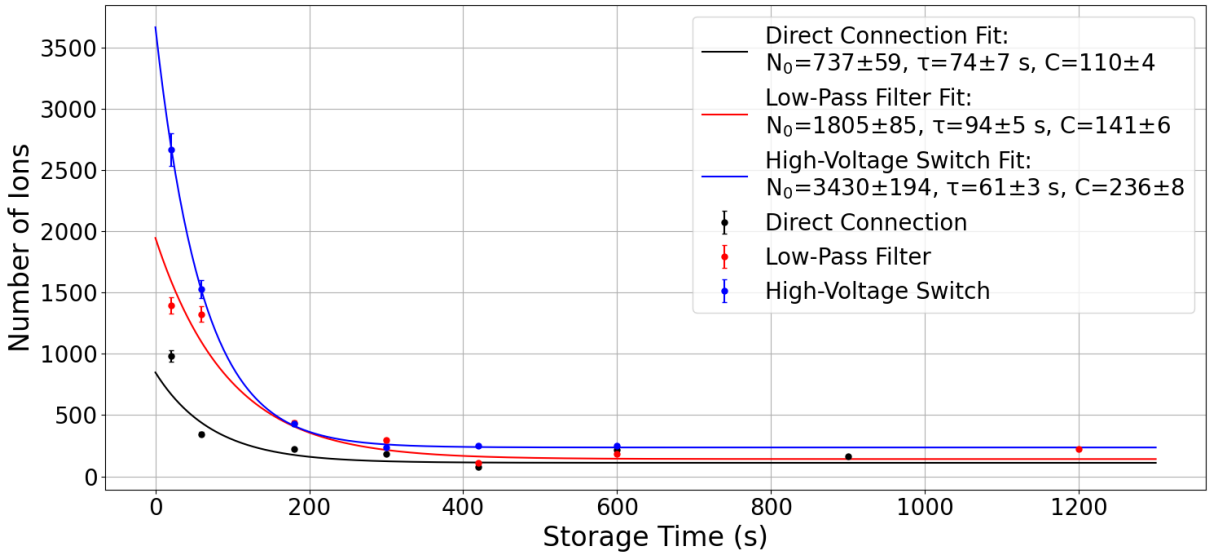

Figure 4.19.: Storage time of the unidentified ions inside the transportable Paul trap. The number of ions was obtained by evaluating videos of ion detection by the MCP detector as captured by the CCD camera. The storage time was measured for three different configurations of the endcap voltage release configuration, namely, either by triggering of the high voltage switch or by lowering the back endcap voltage to 0 V with a direct connection or with the low-pass filter in between. Each data set was fitted with an exponential decay function as described in Eq. 4.3 and the corresponding initial number of ions N_0, storage time τ, and background offset C were evaluated. The lowest storage time of the ions was measured for the direct connection at 61(3) s, followed by the high-voltage switches at 74(7) s, and finally that of the low-pass filter configuration at 94(5) s.

Furthermore, there is a considerable difference in the obtained initial ion number between the configurations. The highest initial ion number of $3.4(2) \times 10^3$ was obtained for the data of the high-voltage switch trigger, followed by that of the low-pass filter at $1.81(9) \times 10^3$, and lastly that of the directly connected electrode at $7.4(6) \times 10^2$. This may come as a result of several effects, firstly that of the instability introduced by noise at the endcaps, which may also be at fault for the short storage times described previously. Furthermore, the gradual detection of ions in the case of the direct connection and low-pass filter data may result in an initial dimmer image, as ions may not have yet reached equilibrium inside the trap and may be exiting individually before the voltage at the endcap reaches close to 0 V. This may, however, not be the case for the high-voltage switch measurement, as ions exit the trap much faster.

It is also important to note that all of the exponential decay fits have a sizeable offset, considered here to be 236(8) ions for the high-voltage switch data, 141(6) ions for the low-pass filter data, and 110(4) ions for the direct connection data. These offsets are not actual ion counts, but rather background intensity still present after the aforementioned background subtraction. A comprehensive evaluation of this offset and the introduced uncertainty is presented in Sec. 4.2.6.

Floated Trap Storage Time

The procedure of extracting and loading antiprotons from the AEgIS experimental apparatus to the room temperature transportable Paul trap relies on the ability to operate the trap with a floated ground potential. Antiprotons are initially ejected by the apparatus at energies in the order of kiloelectronvolts. Floating the ground potential of the trap to match the energy of the

antiproton beam will allow decelerating the antiproton beam, enabling trapping [81]. Confirming the trap's functionality with a floated ground potential is thus a key step towards the goal of transporting antiprotons at room temperature.

In order to confirm the trap's operation at a floated potential, the ground of the trap was floated to 500 V as per the floating configuration shown in Sec. 4.1.3. All other parameters and trapping voltages were kept consistent with previous measurements. From this, the lifetime of the ions was once again measured by recording videos of the MCP detector's phosphor screen with the CCD camera and analysing them with the same methodology as in the previous measurements.

The storage time for the ions in the trap with the floated ground was measured up to 7 min, after this time, no ion signal was clearly visible. The resulting storage time exponential decay can be seen in Fig. 4.20. From the measured data points, a measured storage time of 23(9) s and an initial number of ions of $6(2) \times 10^2$ were extracted. This is a considerably lower storage time and initial number of ions when compared to the previous measurements, also using the low-pass filter but without floating the trap, for which a storage time of 94(5) s and initial ion number of $1.81(9) \times 10^3$ were measured.

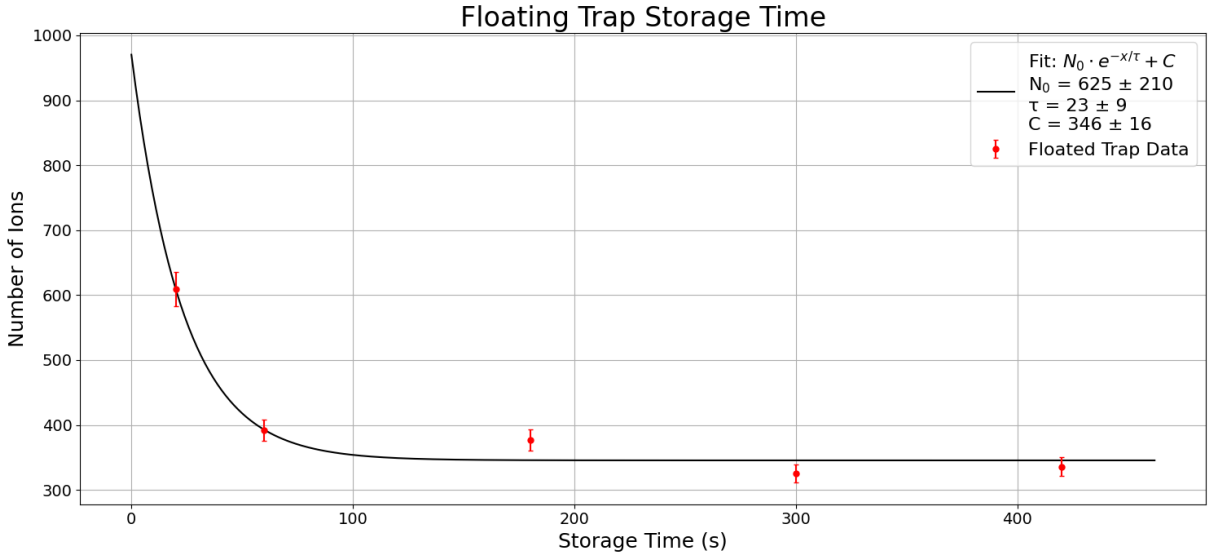

Figure 4.20.: Storage time of the unidentified ions inside the transportable Paul trap when having its reference ground floated at 500 V. Videos of the ions stored for up to 7 min were analyzed, and the number of ions was analyzed exponential decay function as described in Eq. 4.3 with the corresponding initial number of ions N_0, storage time τ, and background offset C was evaluated. A storage time of 23(9) s and an initial number of ions of $6(2) \times 10^2$ were extracted from the fit.

The considerably lower lifetime found when floating the trap, as compared to the measurements under grounded conditions, may be largely explained by an insufficient ground reference. During the experimental sequence, the trap was limited to be floated to only 500 V, as when going any higher, the section of the electronics floated at high-voltage would discharge and generate a spark towards the low-voltage section of the trap. Furthermore, improper shielding and isolation may also generate additional noise that can in turn lower the storage time capabilities of the trap as previously discussed.

4.2.5. Ion Storage during Transport

Confirming the trap's operation during transport is a key step towards achieving the goal of antiproton transport inside the trap. For this reason, the transportable Paul trap functionality was tested for transporting the unidentified ions generated from the ablation of the endcap. The trap, along with its transportable frame with all components attached and secured, was loaded into a truck using a forklift at the University of Innsbruck to be transported to the University of Trento. Once positioned, the trap was secured with straps to the van to avoid movement during transport.

Initially, the two UPSes to power the trap were first switched on, and the trap was first loaded with ions after passing the Austria-Italy border at the Lanz-Brenner rest station (approximate coordinates to 11 m precision: 46.9958, 11.5045) at 13:07. The first destructive measurement of ions was then conducted at a rest station in Campo di Trens, approximately 18.6 km away (approximate coordinates to 11 m precision: 46.8807, 11.4812) at 13:22. The total distance traveled with the trap and alongside the loading and measurement points can be seen in Fig. 4.21.

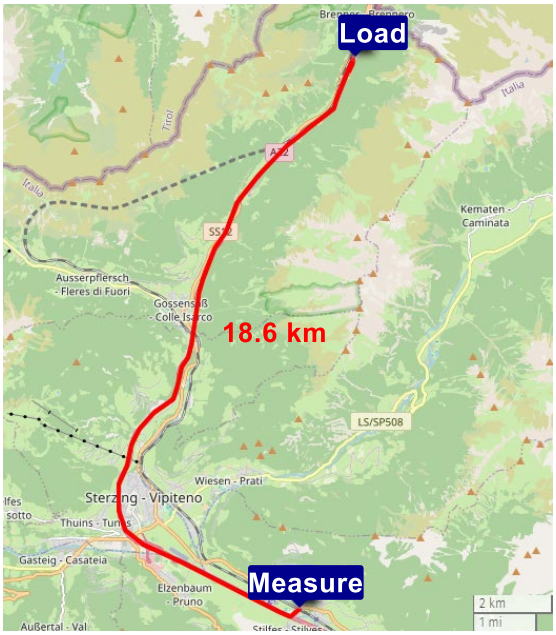

Figure 4.21.: Distance traveled for the performed 15 min storage measurement during transport. Ions were loaded at the Lanz-Brenner rest station (approximate coordinates to 11 m precision: 46.9958, 11.5045) at 13:07, here marked as "Load". The trapped ions were then destructively measured after driving approximately 18.6 km for 15 min at a rest station in Campo di Trens (approximate coordinates to 11 m precision: 46.8807, 11.4812) at 13:22, here marked as "Measure".

From the moment of switching on the trap to the moment of conducting the destructive measurement on the ions, the CCD camera was kept recording a video of the measurement. This measurement was captured in the Mono8 image format (monochrome 8 bits per pixel). After the 15 min drive, the back encap voltage was lowered from 1 kV to 0 V and the ion signal reaching the MCP detector's phosphor screen was recorded.

The captured video frames were then analyzed to extract the estimated ion number as per the steps outlined in Sec. 4.2.3. Due to the experimental conditions in the van, however, the background was not as controlled as in the experimental conditions of the laboratory. For this reason, a lesser number of background frames (here, 15 frames) could be selected for the back-

ground subtraction near the release time of the ions. Likewise, the ion frames were then cropped to select for the region of the MCP where the ion signal is present. The corrected and cropped frames can be seen in Fig. 4.22. From these frames, a total number of ions of $2.4(1) \times 10^3$ was extracted.

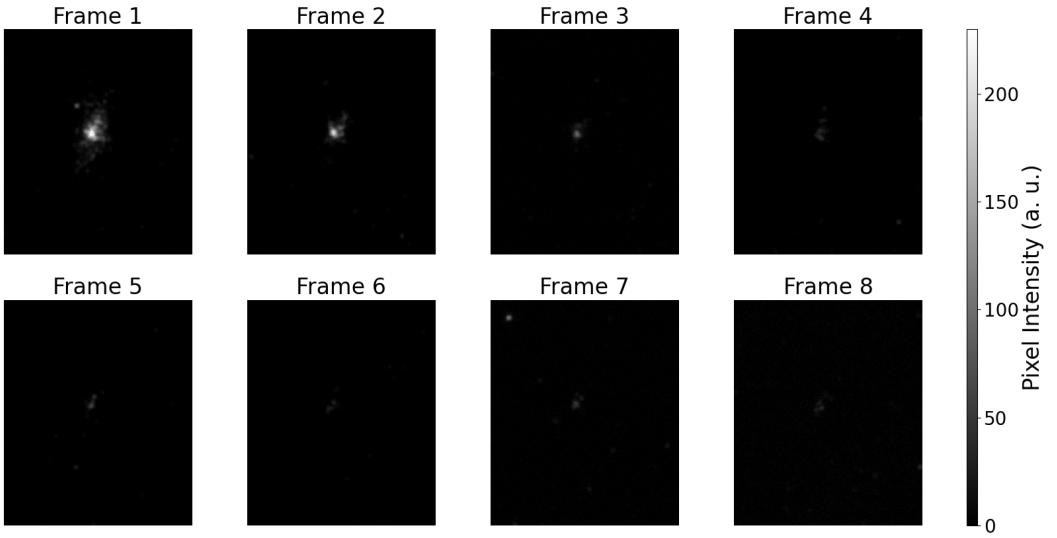

Figure 4.22.: Background-subtracted cropped frames of the measurement of ion transport after 15 min of storage. A total number of ions of $2.4(1) \times 10^3$ was extracted via the frame-by-frame analysis of the video.

Subsequent transport measurements along the route to the University of Trento were conducted, but no improvement in the storage time of the ions during transport was achieved. Furthermore, the experiment was limited by the battery of the UPSes. The UPS that powers the amplifier for the RF signal of the trap switched off after approximately 2 h of measurements, limiting the number of measurement sequences that could be performed on the way to Trento.

4.2.6. Image and Video Uncertainty Discussion

Here, the detection uncertainty stemming from the inherent uncertainty of the MCP detector and CCD camera is discussed. Furthermore, the drift of the radiofrequency peak-to-peak voltage is described, and its impact on the measurements is estimated. Lastly, the ion number offset of the storage time exponential decay fits presented in Sec. 4.2.4 and its dependence on the area of interest taken for the measurements are characterized.

Detection Uncertainty

The detection uncertainty of the ions relies on three main factors. Firstly, the gain uncertainty of the MCP for the ions, as there is an inherent spatial gain inhomogeneity in an MCP detector. Secondly, the phosphor conversion efficiency of the MCP detector, meaning how many photons are generated for every electron that reaches the phosphor screen. Lastly, the camera and imaging uncertainty, which in this particular case largely depends on the frame per second limitations of the CCD camera used.

An MCP detector works by amplifying the signal of incoming ions via secondary electron cascades. The particular model of MCP detector used in the experiment is reported to have

a gain of at least $4 \cdot 10^4$ electrons per ion detected. The gain is, however, variable due to the geometry, applied voltage, aging of the detector, and inhomogeneities. Furthermore, the detector's phosphor conversion efficiency leads to an uncertainty between each ion detection, which is mostly deal with as a component of the statistical uncertainty previously discussed.

The last step in the measurement is the capture of the phosphor screen by the CCD camera in the form of a video. It was found during post-processing that the camera's video frame-per-second capabilities were limited. For the video measurements captured with an exposure time of 100 ms, the frame-per-second of the recorded video was limited to 3.5. This means that there is a considerable data loss from the camera acquisition limitations, which could account for up to 65% loss in data if ions are assumed to arrive homogenously in time. This, while not largely impacting relative measurements between the configurations, may have a large effect on the accuracy of the reported ion numbers. For future measurements, the camera configuration can be adjusted to reduce the data loss. By cropping the size of the recorded video from the control software and increasing the exposure time to 189 ms, it was found that the frames-per-second could be maximized to 5, lowering the estimated maximal losses to 5.5%.

Radio-Frequency Amplitude Drift

Initially, it was determined that the optimal RF trapping voltage measured at the oscilloscope was approximately V_{RF} =600 V. However, during the course of the lifetime measurements in the laboratory, a drift of the measured RF voltage after the capacity divider at the oscilloscope was observed, introducing uncertainty into the number of ions measured.

The first measurements performed were conducted with a direct connection between the trap and the high-voltage power supply. At the beginning of these measurements, the value recorded at the oscilloscope was approximately 607 V with the Red Pitaya input voltage set to 0.34 V as previously determined to be optimal. By the end of the performed measurements, when beginning a new round of measurements using the low-pass filter, the value recorded at the oscilloscope had reduced to 553 V. Consequently, for the last set of measurements using the high-voltage switches, the value at the oscilloscope had reduced to approximately 501 V.

In order to estimate the impact of the radiofrequency measured at the oscilloscope drifting during measurements, the peak-to-peak radiofrequency voltage scan presented in Sec. 4.2.2 is utilized. The trap was found to be optimized when keeping the input RF voltage of the trap close to V_{RF} =600 V. Nevertheless, values were shown to oscillate down to 500 V at times. Assuming a close to worst case scenario, taking into account the values presented in Fig. 4.13 from the measured voltage of 608 V to 501 V, an estimated reduction in mean intensity between ion images of -12.5% was observed.

Background Ion Number Offset

As seen from the lifetime measurements presented in Sec. 4.2.4, a non-negligible offset with the intensity of several hundred ions was present during all measurements, even after background subtraction of the analyzed frames. This offset is highly dependent on the area of interest analyzed in the measurements.

The ion number offset's dependence on the area of interest analyzed was characterized by recording the offset C for different cropped areas of interest of the floated trap measurements presented in Sec. 4.2.4. The analyzed areas (including their width and height in pixels) and corresponding exponential decay offset are presented in Table 4.1.

The offset values obtained alongside the image's area of interest were plotted as seen in Fig. 4.23.

Height (px)	Width (px)	Image Area of Interest (px^2)	Ion Number Offset C
300	250	7.5×10^4	346(16)
300	200	6×10^4	276(15)
300	150	4.5×10^4	211(14)
250	150	3.75×10^4	175(13)
200	150	3×10^4	143(12)

Table 4.1.: Offset C of the storage time exponential decay fit as per Eq. 4.3 of the storage time for the unidentified ions trapped in the transportable Paul trap during floating at 500 V for different-sized areas of interest in pixels squared, alongside the image's height and width in pixels.

The data is closely described with a linear function, exhibiting a coefficient of determination $R^2 = 0.9998$. This behavior indicates the offset may be caused by a remaining background signal even after the background subtraction is performed.

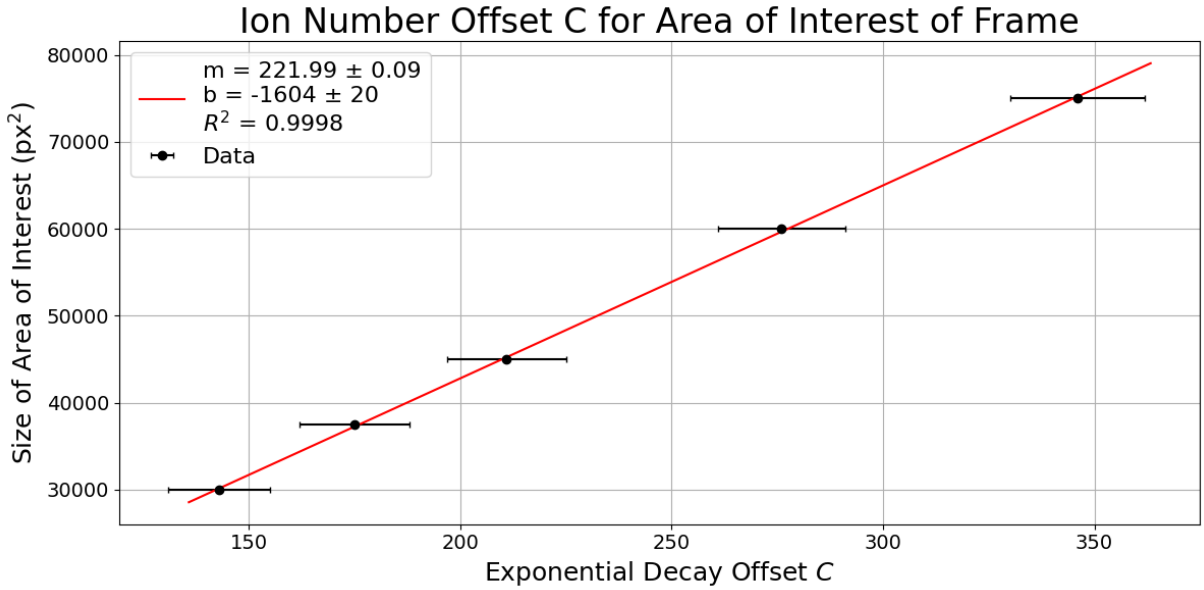

Figure 4.23.: Plot of the offset C for different sizes of the area of interest as presented in Table 4.1. The data is closely described by a linear fit ($R^2 = 0.9998$) with a slope of 221.99(9) pixels squared per ion number offset and an intercept at $-1.60(2) \times 10^3$ pixels squared. The linear behaviour is indicative of an offset caused by a remaining background signal even after background subtraction.

A possible improvement to reduce the offset caused by a non-optimal signal-to-noise ratio can be achieved by image processing thresholding. This means processing only pixels that are above a certain intensity, in order to filter out background pixels from the signal.

4.3. Antiproton Extraction at the AEgIS Experiment

The procedure of extracting antiprotons from the AEgIs experiment had only been preliminarily tested before the work on this thesis. The extraction of non-electron cooled antiprotons from the AEgIS was demonstrated for the purposes of the development of a high precision detector [51]. For the purpose of loading electron-cooled antiprotons into the transportable Paul trap, an additional

loading technique and detection strategy have to be developed.

The extraction of cooled antiprotons from the AEgIS trap into the extraction port of the transportable Paul trap involves the adjustment of several electrodes across the beamline. The voltages of these electrodes have to be optimized to result in the maximal signal of antiprotons at the extraction port. During the work of this thesis, an MCP detector assembly for antiprotons was installed at the extraction port of the AEgIS experimental beamline. Here, the assembly process of this detector is presented and the detection strategy outlined.

Furthermore, this section presents preliminary results of low-energy antiprotons extracted from the AEgIS experimental apparatus back into the beamline. From these initial measurements performed an estimate for the extracted antiproton beam energy was calculated to be 2.19(9) keV via a time of flight measurement performed with scintillator detectors.

4.3.1. Detector Assembly for Antiproton Extraction

Loading antiprotons from the AEgIS apparatus into the transportable Paul trap requires the antiproton beam to be sent by a pulsed drift tube from the 5 T trap and guided via bender electrodes and einzel lenses positioned across the beamline, as seen in Fig. 4.24. The tools in place allow for the steering of antiprotons in the direction of the 75° extraction port. This is inherently a reversal of the extraction direction of the antiprotons, meaning a substantial optimization of several electrodes across the beamline is needed. For this reason, a few diagnostic tools have been developed during the course of this thesis to look at the quality, shape, and spread of the beam before it is able to reach the transportable Paul trap.

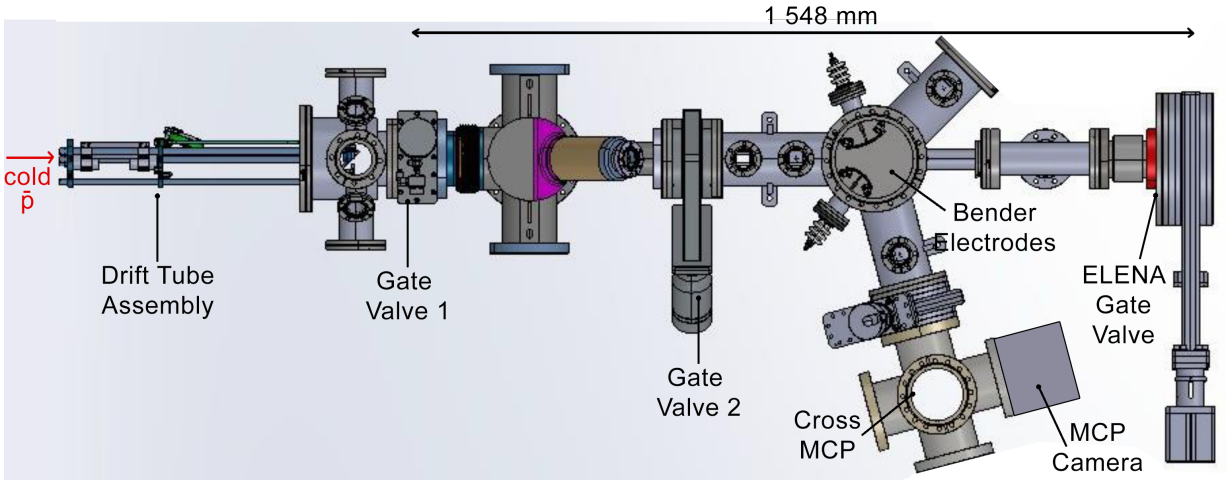

Figure 4.24.: Region of the AEgIS beamline connected to the ELENA facility. Antiprotons are injected from right (ELENA) to left (AEgIS trap). The work presented in this chapter consists of reversing the direction of the antiproton beam, i.e., extracting antiprotons from the AEgIS Penning trap towards the 75° extraction port of the beamline. To do so, cold antiprotons coming from the AEgIS apparatus are pulsed by the drift tube assembly and stirred across the beamline by bending and focusing electrodes. The main goal of this procedure is to optimize the incoming antiproton beam at the imaging MCP detector found in the six-way ConFlat 100 cross, here referred to as the "Cross MCP". The antiproton beam will be measured and optimized by looking at the image of the phosphor screen of the detector with a camera, here labeled "MCP Camera". Across the beamline, there are several gate valves, gate valve 1, gate valve 2, and the Elena gate valve, which were used as obstacles for the antiproton beam to be measured with a scintillator tube positioned on top of the ELENA gate valve.

In order to optimize the beam steering towards the portable trap, the AEgIS control system

has full control of all electrodes in the beamline. Optimization is then possible by scanning along a series of voltages for the electrodes and verifying if antiprotons are reaching the extraction site located at the 75° extraction port of the beamline. The work of this thesis involved the installation of an imaging microchannel plate detector (MCP) assembly at the extraction port after the 75° turn in the AEgIS beamline.

This detector was mounted on a pneumatic actuator that allows it to be moved in and out of the beamline without needing to break the vacuum. The pneumatic actuator ConFlat 40 flange is mounted on a ConFlat 100 six-way cross. Behind the MCP, there is a prism that reflects the image of the phosphor screen of the detector towards one of the other sides of the six-way cross. This side flange has a viewport, where a camera is placed to record the image of the MCP. Fig. 4.25 shows a picture of the MCP assembly that is found inside the six-way cross, referred to as the "cross MCP".

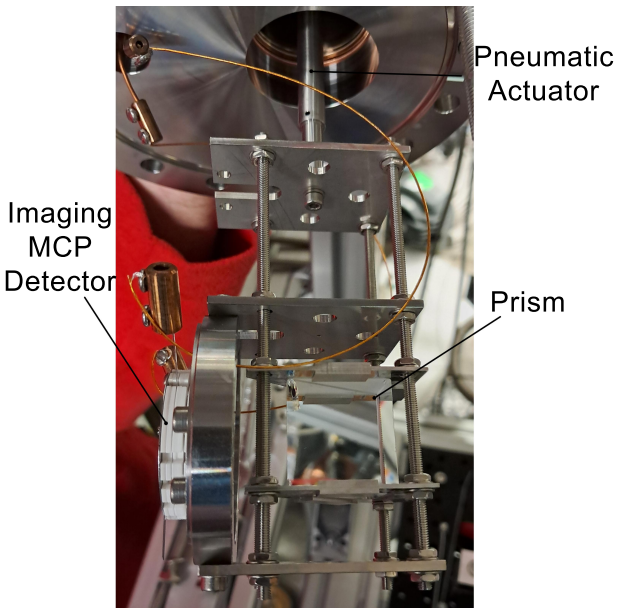

Figure 4.25.: Side view of the MCP assembly that was developed during the thesis, and it is located inside the "Cross MCP" (see Fig. 4.24). The MCP sits on a custom holder attached to a pneumatic actuator that allows for pushing and pulling the detector in and out of the beamline. Behind the MCP, there is a prism that reflects the image of the MCP's phosphor screen out through a viewport into a camera.

The verification of antiprotons reaching the extraction site can be performed by capturing images of the MCP's phosphor screen and optimizing the steering of the beam until the maximal signal is reached. The preliminary procedures of setting up the hardware and integrating the software of the camera into the AEgIS control system were conducted during the work of this thesis. Furthermore, extraction attempts were performed using simulated optimal voltages for the electrodes on the beamline. While the extraction of an antiproton beam and optimization of the beam line voltages to reach the site has yet to be achieved, the functionality of the MCP detector assembly was confirmed. During the initial extraction attempts, a suspected pion event was detected by the MCP detector as seen in Fig. 4.26. This detection event likely stems from a stray pion reaching the detector from an annihilation event somewhere in the beam line. Nevertheless, due to limitations of the available antiproton beamtime, no additional measurements could be performed.

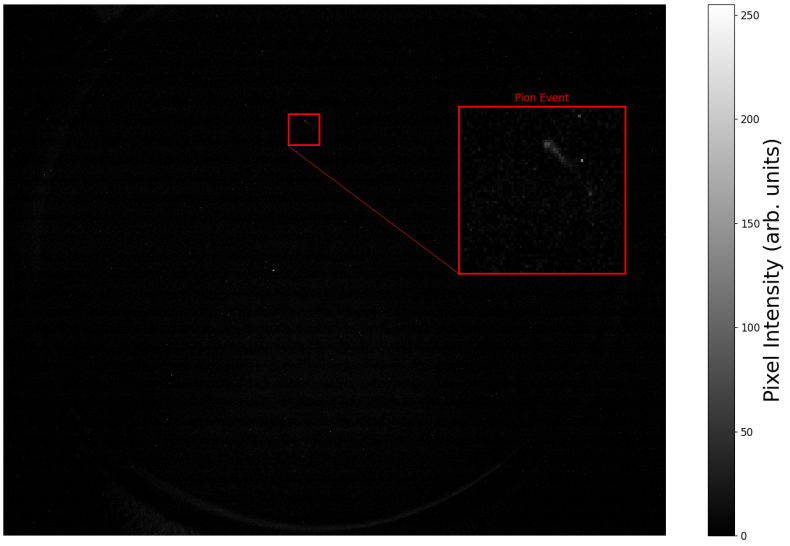

Figure 4.26.: A pion event detected with the MCP detector during antiproton extraction attempts that confirms the functionality of the assembly. Unfortunately, the antiproton beam could not be steered on this detector due to beamtime limitations, as discussed in the main text.

4.3.2. Preliminary Antiproton Extraction Measurements

The backward extraction of antiprotons from the 5 T Penning trap towards the ELENA ring was attempted via a time of flight measurement using a sodium iodide scintillator with thallium impurities (NaI(Tl)). These are a type of inorganic crystal scintillators that operate via ionizing radiation stemming from the antiprotons annihilating on the beamline. The excitation of electrons forming free electron-hole pairs in the crystal leads to scintillation of the impurities in it. This signal is amplified and captured via the photomultiplier tube in the detector. The characteristic shape of a NaI(Tl) scintillator signal can be closely approximated by a double exponential given by [82]

$$y(t) = \left(e^{-t/\tau_d} - e^{-t/\tau_r}\right), \tag{4.4}$$

which describes the exponential rise time τ_r and decay time τ_d of the scintillator signal in time t with a normalization factor A. This characteristic shape comes as a result of the exponential rise due to electron-hole pair formation and an exponential decay from de-excitation scintillation.

The NaI(Tl) scintillator was positioned on top of the gate valve that goes from the AEgIS beamline back to the ELENA ring. High-energy pions and other charged particles created via antiproton annihilation are detected by the scintillator, allowing to determine at which point in time annihilation occurred i.e. when the antiprotons are annihilating in the beamline. The annihilation measurement via the NaI scintillator was conducted for different configurations of the beamline, where gate-valves across it are closed to function as blockages and determine where the beam is annihilating in space. This way, both the information of where and when antiprotons are annihilating is known, allowing to determine how the beam is being stirred in the beamline without having a direct measurement. For this measurement, two different gate valves in the beamline were closed. First, the first gate valve (Gate Valve 1) between the 5 T and the beam steering electrodes is closed, and the annihilation peak is observed and maximized by adjusting some of the guiding electrodes. Lastly, the final gate valve, which goes from the beamline to the ELENA ring (Gate Valve ELENA) is closed, and the same operation is performed. A computer-aided design drawing of the section of the beamline used for this measurement can be seen in

Fig. 4.24

Initially, an uncompressed electron-cooled antiproton beam was used for reverse extraction toward the extraction port. As seen from the data in Fig. 4.27, this beam seemed to be too broad and unfocused for performing the steering and bending maneuver into the 75° extraction port. The bulk of the beam was annihilated in the region between the drift tube and the bending electrodes, with only a small portion getting all the way to the back and reaching the closed ELENA gate valve. This was largely due to the unfocussing of the beam when exiting the higher magnetic field region inside the 5 T Penning trap to the lower magnetic field region of the beamline. A similar measurement was performed for an electron-cooled antiproton beam exiting the AEgIS apparatus. The annihilation peak was measured with the first gate valve between the trap and the bender electrodes (Gate Valve 1) closed, to conduct a time of flight measurement between the two annihilation peaks.

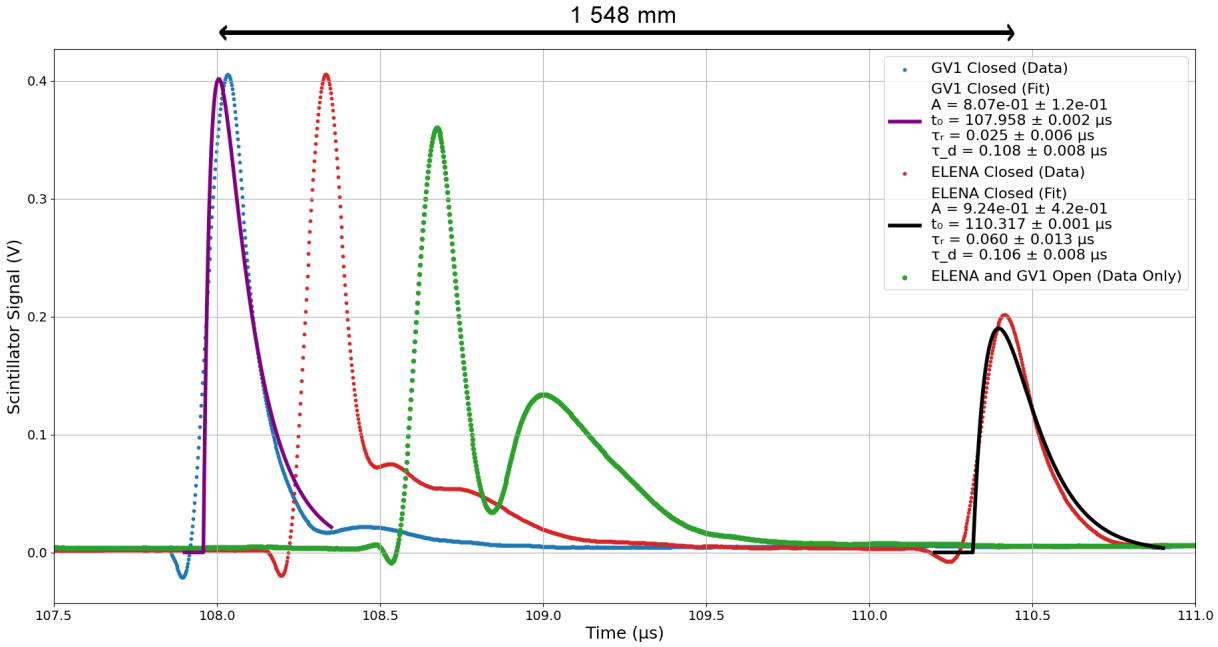

Figure 4.27.: Antiproton annihilation signal on a scintillator positioned on the beamline of the AEgIS experiment. The scintillator signal in Volts determines the time in microseconds from when the antiprotons are extracted from the 5 T AEgIS trap to when they annihilate on the beamline. The red dotted curve represents the data for the extraction of an uncompressed beam of antiprotons with the ELENA Gate Valve closed. The blue dotted curve is the data from a compressed and electron-cooled beam of antiprotons with Gate Valve 1 closed. These two curves were fitted with the function presented in Eq. 4.4 and are shown as a solid black and solid purple curve respectively. The physical distance between the two gate valves (GV1 and ELENA) is approximately 1548 mm. The green dotted curve is the data for a compressed electron-cooled beam of antiprotons with both gate valves open. Cold antiprotons were detected to be annihilating in the region between the drift tube and the bending electrodes. A new diagnostic tool will be put in place to determine the quality of the beam when leaving the drift tube to correct its trajectory for future extraction attempts.

Physically, the first gate valve and the ELENA gate valve are separated by a distance of approximately d =1548 m. From the conducted time of flight measurement, the energy of the beam can be determined by measuring its velocity v via

$$v = \frac{d}{t_1 - t_0}, \tag{4.5}$$

with $t_0 = 108.01(1)\,\mu s$ being the time at which the scintillator detects the annihilation with Gate Valve 1, and $t_1 = 110.40(5)\,\mu s$ the time at which it detects the annihilation with the ELENA Gate Valve. These times were determined by finding the mean time of the annihilation peaks in Fig. 4.27. From this, the average kinetic energy $E_{\bar{p}}$ of the antiproton beam ($m_p = 1.672 \times 10^{-27}$kg [83]) can be calculated to be

$$E_{\bar{p}} = \frac{1}{2}mv^2 = 2.19(9)\,\text{keV}. \tag{4.6}$$

This kinetic energy measurement justifies the need for floating the transportable Paul trap to a few kilovolts in order to be able to catch the incoming beam of antiprotons. For antiprotons at the calculated 2.1 keV, the trap would have to be raised to 2.1 kV with respect to the antiprotons' reference potential for them to match their energy and be able to capture them.

Optimization measurements of a compressed antiproton beam were then performed to attempt to reach the extraction port. The beam was stirred along the beamline past the open Gate Valve 1 into the region with the bender electrodes. However, the defocusing effect from exiting the region of high magnetic field seemed to be too large for the antiproton beam to reach the 75° extraction port. The annihilation peaks of the compressed cold antiproton can be seen in Fig. 4.27. This measurement, however, showed a significant improvement over the initial measurement for the uncompressed beam, as the largest annihilation peak occurred further along the beamline, inside the bender electrode region. This indicates that the compression of the antiproton beam may be a crusial step for the success of future extraction attemps.

To perform this optimization measurement systematically, an additional MCP detector will be placed in the region between the drift tube assembly and the bender electrodes. This detector will be on a rotating mount, allowing it to be placed in and out of the beamline when needed. The imaging from the phosphor screen of this MCP will allow for determining the quality and trajectory of the beam as it is leaving the 5 T Penning trap, enabling optimization of the beam before reaching the bending electrodes.

5. Outlook and Conclusion

This thesis has presented the challenges faced by antimatter precision experiments conducted at low energies due to restricted antiproton availability. The transport of low-energy antiprotons, which can currently only be experimented with at CERN's Antimatter Factory facilities, would pave the way for future precision experiments with antimatter. Within this framework, the use of low-energy antiprotons for generating HCIs for use in metrology and the prospects of this production method are presented in this work. Calculations and simulations conducted for determining a viable list of HCI candidates for such experiments were discussed.

Furthermore, this thesis extensively describes the experimental work conducted in the development, assembly, and testing of a transportable linear Paul trap intended for experiments with antiprotons. Here, results on the trap's trapping parameter optimization, ion storage time characterization, and trapped ion transport are presented. Furthermore, the ongoing efforts of low-energy antiproton extraction from the AEgIS experimental apparatus are discussed, and preliminary results are presented.

In the experimental work presented, the ions trapped in the linear Paul trap have been described as unidentified. This is due to the species of the ions trapped being unknown, as these were generated by direct ablation of the 316L stainless steel flat endcap electrodes of the trap. The composition of 316L stainless steel suggests that the ions created may originate from Iron, Chromium, Nitrogen, Molybdenum, Manganese, Carbon, Silicon, Sulfur, or Phosphor [84]. Initial mass estimate calculations suggest the mass of the trapped ions is close to that of C^+, however, no definitive conclusions could be drawn.

Further experiments with the transportable linear Paul trap are needed to determine the ion species trapped. This includes, but is not limited to, additional attempts at trapping ions generated from ablation of the targets (Mo, Nb, Yb, Ba) found inside the trap. These efforts can be performed alongside fluorescence detection measurements of known atomic transitions of the ions for confirmation of the ionic species trapped. Once a known species of ions is trapped, one can interpolate from the trapping parameters used to determine the mass of the unidentified species of ions. Efforts for performing this mass calibration are underway by developing a laser cooling and fluorescence detection mechanism for Barium ions.

Another key challenge faced during the experimental efforts presented in this thesis was the limited antiproton extraction results from the AEgIS experiment. The available antiproton beam time at CERN's Antimatter Factory facilities is highly restricted and often has to be split among several experiments within a collaboration. Antiprotons are a coveted resource at these experimental facilities, as they are only available for approximately half of the year [85]. Data taking during this period was therefore limited, and with a complicated optimization at hand, the results of successful antiproton extraction were limited.

Future low-energy antiproton extraction attempts from the AEgIS experiment will be performed with additional diagnostic tools placed on the beamline. These tools will access the shape and spread of the antiproton beam before reaching the extraction port, allowing for a systematic correction and optimization of its trajectory. Once this procedure can be successfully achieved, the transportable antiproton trap will be placed on the extraction port of the beamline to begin antiproton trapping experiments.

Bibliography

[1] Helen R. Quinn. The asymmetry between matter and antimatter. *Physics Today*, 56(2):30–35, 2003.

[2] Carl D. Anderson. The positive electron. *Phys. Rev.*, 43:491–494, Mar 1933.

[3] Laurent Canetti, Marco Drewes, and Mikhail Shaposhnikov. Matter and antimatter in the universe. *New Journal of Physics*, 14(9):095012, Sep 2012.

[4] David S. Pereira, João Ferraz, Francisco S. N. Lobo, and José P. Mimoso. Baryogenesis: A symmetry breaking in the primordial universe revisited. *Symmetry*, 16(1), 2024.

[5] LHCb collaboration, R. Aaij, A. S. W. Abdelmotteleb, C. Abellan Beteta, F. Abudinén, T. Ackernley, A. A. Adefisoye, B. Adeva, M. Adinolfi, P. Adlarson, C. Agapopoulou, C. A. Aidala, Z. Ajaltouni, S. Akar, K. Akiba, P. Albicocco, J. Albrecht, F. Alessio, Z. Aliouche, P. Alvarez Cartelle, R. Amalric, S. Amato, J. L. Amey, Y. Amhis, L. An, L. Anderlini, M. Andersson, A. Andreianov, P. Andreola, M. Andreotti, D. Andreou, A. Anelli, D. Ao, F. Archilli, M. Argenton, S. Arguedas Cuendis, A. Artamonov, M. Artuso, E. Aslanides, R. Ataíde Da Silva, M. Atzeni, B. Audurier, D. Bacher, I. Bachiller Perea, S. Bachmann, M. Bachmayer, J. J. Back, P. Baladron Rodriguez, V. Balagura, A. Balboni, W. Baldini, L. Balzani, H. Bao, J. Baptista de Souza Leite, C. Barbero Pretel, M. Barbetti, I. R. Barbosa, R. J. Barlow, M. Barnyakov, S. Barsuk, W. Barter, J. Bartz, J. M. Basels, S. Bashir, B. Batsukh, P. B. Battista, A. Bay, A. Beck, M. Becker, F. Bedeschi, I. B. Bediaga, N. A. Behling, S. Belin, K. Belous, I. Belov, I. Belyaev, G. Benane, G. Bencivenni, E. Ben-Haim, A. Berezhnoy, R. Bernet, S. Bernet Andres, A. Bertolin, C. Betancourt, F. Betti, J. Bex, Ia. Bezshyiko, O. Bezshyyko, J. Bhom, M. S. Bieker, N. V. Biesuz, P. Billoir, A. Biolchini, M. Birch, F. C. R. Bishop, A. Bitadze, A. Bizzeti, T. Blake, F. Blanc, J. E. Blank, S. Blusk, V. Bocharnikov, J. A. Boelhauve, O. Boente Garcia, T. Boettcher, A. Bohare, A. Boldyrev, C. S. Bolognani, R. Bolzonella, R. B. Bonacci, N. Bondar, A. Bordelius, F. Borgato, S. Borghi, M. Borsato, J. T. Borsuk, E. Bottalico, S. A. Bouchiba, M. Bovill, T. J. V. Bowcock, A. Boyer, C. Bozzi, J. D. Brandenburg, A. Brea Rodriguez, N. Breer, J. Brodzicka, A. Brossa Gonzalo, J. Brown, D. Brundu, E. Buchanan, L. Buonincontri, M. Burgos Marcos, A. T. Burke, C. Burr, J. S. Butter, J. Buytaert, W. Byczynski, S. Cadeddu, H. Cai, A. Caillet, R. Calabrese, S. Calderon Ramirez, L. Calefice, S. Cali, M. Calvi, M. Calvo Gomez, P. Camargo Magalhaes, J. I. Cambon Bouzas, P. Campana, D. H. Campora Perez, A. F. Campoverde Quezada, S. Capelli, L. Capriotti, R. Caravaca-Mora, A. Carbone, L. Carcedo Salgado, R. Cardinale, A. Cardini, P. Carniti, L. Carus, A. Casais Vidal, R. Caspary, G. Casse, M. Cattaneo, G. Cavallero, V. Cavallini, S. Celani, S. Cesare, A. J. Chadwick, I. Chahrour, H. Chang, M. Charles, Ph. Charpentier, E. Chatzianagnostou, M. Chefdeville, C. Chen, S. Chen, Z. Chen, A. Chernov, S. Chernyshenko, X. Chiotopoulos, V. Chobanova, M. Chrzaszcz, A. Chubykin, V. Chulikov, P. Ciambrone, X. Cid Vidal, G. Ciezarek, P. Cifra, P. E. L. Clarke, M. Clemencic, H. V. Cliff, J. Closier, C. Cocha Toapaxi, V. Coco, J. Cogan, E. Cogneras, L. Cojocariu, S. Collaviti, P. Collins, T. Colombo, M. Colonna, A. Comerma-Montells, L. Congedo, A. Contu,

N. Cooke, C. Coronel, I. Corredoira, A. Correia, G. Corti, J. Cottee Meldrum, B. Couturier, D. C. Craik, M. Cruz Torres, E. Curras Rivera, R. Currie, C. L. Da Silva, S. Dadabaev, L. Dai, X. Dai, E. Dall'Occo, J. Dalseno, C. D'Ambrosio, J. Daniel, A. Danilina, P. d'Argent, G. Darze, A. Davidson, J. E. Davies, O. De Aguiar Francisco, C. De Angelis, F. De Benedetti, J. de Boer, K. De Bruyn, S. De Capua, M. De Cian, U. De Freitas Carneiro Da Graca, E. De Lucia, J. M. De Miranda, L. De Paula, M. De Serio, P. De Simone, F. De Vellis, J. A. de Vries, F. Debernardis, D. Decamp, V. Dedu, S. Dekkers, L. Del Buono, B. Delaney, H. P. Dembinski, J. Deng, V. Denysenko, O. Deschamps, F. Dettori, B. Dey, P. Di Nezza, I. Diachkov, S. Didenko, S. Ding, L. Dittmann, V. Dobishuk, A. D. Docheva, C. Dong, A. M. Donohoe, F. Dordei, A. C. dos Reis, A. D. Dowling, W. Duan, P. Duda, M. W. Dudek, L. Dufour, V. Duk, P. Durante, M. M. Duras, J. M. Durham, O. D. Durmus, A. Dziurda, A. Dzyuba, S. Easo, E. Eckstein, U. Egede, A. Egorychev, V. Egorychev, S. Eisenhardt, E. Ejopu, L. Eklund, M. Elashri, J. Ellbracht, S. Ely, A. Ene, J. Eschle, S. Esen, T. Evans, F. Fabiano, S. Faghih, L. N. Falcao, Y. Fan, B. Fang, L. Fantini, M. Faria, K. Farmer, D. Fazzini, L. Felkowski, M. Feng, M. Feo, A. Fernandez Casani, M. Fernandez Gomez, A. D. Fernez, F. Ferrari, F. Ferreira Rodrigues, M. Ferrillo, M. Ferro-Luzzi, S. Filippov, R. A. Fini, M. Fiorini, M. Firlej, K. L. Fischer, D. S. Fitzgerald, C. Fitzpatrick, T. Fiutowski, F. Fleuret, M. Fontana, L. F. Foreman, R. Forty, D. Foulds-Holt, V. Franco Lima, M. Franco Sevilla, M. Frank, E. Franzoso, G. Frau, C. Frei, D. A. Friday, J. Fu, Q. Führing, Y. Fujii, T. Fulghesu, E. Gabriel, G. Galati, M. D. Galati, A. Gallas Torreira, D. Galli, S. Gambetta, M. Gandelman, P. Gandini, B. Ganie, H. Gao, R. Gao, T. Q. Gao, Y. Gao, Y. Gao, Y. Gao, L. M. Garcia Martin, P. Garcia Moreno, J. García Pardiñas, P. Gardner, K. G. Garg, L. Garrido, C. Gaspar, A. Gavrikov, L. L. Gerken, E. Gersabeck, M. Gersabeck, T. Gershon, S. Ghizzo, Z. Ghorbanimoghaddam, L. Giambastiani, F. I. Giasemis, V. Gibson, H. K. Giemza, A. L. Gilman, M. Giovannetti, A. Gioventù, L. Girardey, C. Giugliano, M. A. Giza, F. C. Glaser, V. V. Gligorov, C. Göbel, L. Golinka-Bezshyyko, E. Golobardes, D. Golubkov, A. Golutvin, S. Gomez Fernandez, W. Gomulka, F. Goncalves Abrantes, M. Goncerz, G. Gong, J. A. Gooding, I. V. Gorelov, C. Gotti, E. Govorkova, J. P. Grabowski, L. A. Granado Cardoso, E. Graugés, E. Graverini, L. Grazette, G. Graziani, A. T. Grecu, L. M. Greeven, N. A. Grieser, L. Grillo, S. Gromov, C. Gu, M. Guarise, L. Guerry, V. Guliaeva, P. A. Günther, A. K. Guseinov, E. Gushchin, Y. Guz, T. Gys, K. Habermann, T. Hadavizadeh, C. Hadjivasiliou, G. Haefeli, C. Haen, G. Hallett, M. M. Halvorsen, P. M. Hamilton, J. Hammerich, Q. Han, X. Han, S. Hansmann-Menzemer, L. Hao, N. Harnew, T. H. Harris, M. Hartmann, S. Hashmi, J. He, F. Hemmer, C. Henderson, R. D. L. Henderson, A. M. Hennequin, K. Hennessy, L. Henry, J. Herd, P. Herrero Gascon, J. Heuel, A. Hicheur, G. Hijano Mendizabal, J. Horswill, R. Hou, Y. Hou, N. Howarth, J. Hu, W. Hu, X. Hu, W. Huang, W. Hulsbergen, R. J. Hunter, M. Hushchyn, D. Hutchcroft, M. Idzik, D. Ilin, P. Ilten, A. Inglessi, A. Iniukhin, A. Ishteev, K. Ivshin, R. Jacobsson, H. Jage, S. J. Jaimes Elles, S. Jakobsen, E. Jans, B. K. Jashal, A. Jawahery, V. Jevtic, E. Jiang, X. Jiang, Y. Jiang, Y. J. Jiang, M. John, A. John Rubesh Rajan, D. Johnson, C. R. Jones, T. P. Jones, S. Joshi, B. Jost, J. Juan Castella, N. Jurik, I. Juszczak, D. Kaminaris, S. Kandybei, M. Kane, Y. Kang, C. Kar, M. Karacson, D. Karpenkov, A. Kauniskangas, J. W. Kautz, M. K. Kazanecki, F. Keizer, M. Kenzie, T. Ketel, B. Khanji, A. Kharisova, S. Kholodenko, G. Khreich, T. Kirn, V. S. Kirsebom, O. Kitouni, S. Klaver, N. Kleijne, K. Klimaszewski, M. R. Kmiec, S. Koliiev, L. Kolk, A. Konoplyannikov, P. Kopciewicz, P. Koppenburg, A. Korchin, M. Korolev, I. Kostiuk, O. Kot, S. Kotriakhova, A. Kozachuk, P. Kravchenko, L. Kravchuk, M. Kreps, P. Krokovny, W. Krupa, W. Krzemien, O. Kshyvanskyi, S. Kubis, M. Kucharczyk, V. Kudryavtsev, E. Kulikova, A. Kupsc, B. K. Kutsenko, I. Kyryllin, D. Lacarrere,

P. Laguarta Gonzalez, A. Lai, A. Lampis, D. Lancierini, C. Landesa Gomez, J. J. Lane, R. Lane, G. Lanfranchi, C. Langenbruch, J. Langer, O. Lantwin, T. Latham, F. Lazzari, C. Lazzeroni, R. Le Gac, H. Lee, R. Lefèvre, A. Leflat, S. Legotin, M. Lehuraux, E. Lemos Cid, O. Leroy, T. Lesiak, E. D. Lesser, B. Leverington, A. Li, C. Li, C. Li, H. Li, J. Li, K. Li, L. Li, M. Li, P. Li, P. R. Li, Q. Li, S. Li, T. Li, T. Li, Y. Li, Y. Li, Z. Lian, X. Liang, S. Libralon, C. Lin, T. Lin, R. Lindner, H. Linton, V. Lisovskyi, R. Litvinov, D. Liu, F. L. Liu, G. Liu, K. Liu, S. Liu, W. Liu, Y. Liu, Y. Liu, Y. L. Liu, G. Loachamin Ordonez, A. Lobo Salvia, A. Loi, T. Long, J. H. Lopes, A. Lopez Huertas, S. López Soliño, Q. Lu, C. Lucarelli, D. Lucchesi, M. Lucio Martinez, V. Lukashenko, Y. Luo, A. Lupato, E. Luppi, K. Lynch, X. R. Lyu, G. M. Ma, S. Maccolini, F. Machefert, F. Maciuc, B. Mack, I. Mackay, L. M. Mackey, L. R. Madhan Mohan, M. J. Madurai, A. Maevskiy, D. Magdalinski, D. Maisuzenko, J. J. Malczewski, S. Malde, L. Malentacca, A. Malinin, T. Maltsev, G. Manca, G. Mancinelli, C. Mancuso, R. Manera Escalero, F. M. Manganella, D. Manuzzi, D. Marangotto, J. F. Marchand, R. Marchevski, U. Marconi, E. Mariani, S. Mariani, C. Marin Benito, J. Marks, A. M. Marshall, L. Martel, G. Martelli, G. Martellotti, L. Martinazzoli, M. Martinelli, D. Martinez Gomez, D. Martinez Santos, F. Martinez Vidal, A. Martorell i Granollers, A. Massafferri, R. Matev, A. Mathad, V. Matiunin, C. Matteuzzi, K. R. Mattioli, A. Mauri, E. Maurice, J. Mauricio, P. Mayencourt, J. Mazorra de Cos, M. Mazurek, M. McCann, T. H. McGrath, N. T. McHugh, A. McNab, R. McNulty, B. Meadows, G. Meier, D. Melnychuk, F. M. Meng, M. Merk, A. Merli, L. Meyer Garcia, D. Miao, H. Miao, M. Mikhasenko, D. A. Milanes, A. Minotti, E. Minucci, T. Miralles, B. Mitreska, D. S. Mitzel, A. Modak, L. Moeser, R. A. Mohammed, R. D. Moise, E. F. Molina Cardenas, T. Mombächer, M. Monk, S. Monteil, A. Morcillo Gomez, G. Morello, M. J. Morello, M. P. Morgenthaler, J. Moron, W. Morren, A. B. Morris, A. G. Morris, R. Mountain, H. Mu, Z. M. Mu, E. Muhammad, F. Muheim, M. Mulder, K. Müller, F. Muñoz-Rojas, R. Murta, V. Mytrochenko, P. Naik, T. Nakada, R. Nandakumar, T. Nanut, I. Nasteva, M. Needham, E. Nekrasova, N. Neri, S. Neubert, N. Neufeld, P. Neustroev, J. Nicolini, D. Nicotra, E. M. Niel, N. Nikitin, Q. Niu, P. Nogarolli, P. Nogga, C. Normand, J. Novoa Fernandez, G. Nowak, C. Nunez, H. N. Nur, A. Oblakowska-Mucha, V. Obraztsov, T. Oeser, S. Okamura, A. Okhotnikov, O. Okhrimenko, R. Oldeman, F. Oliva, M. Olocco, C. J. G. Onderwater, R. H. O'Neil, D. Osthues, J. M. Otalora Goicochea, P. Owen, A. Oyanguren, O. Ozcelik, F. Paciolla, A. Padee, K. O. Padeken, B. Pagare, T. Pajero, A. Palano, M. Palutan, X. Pan, G. Panshin, L. Paolucci, A. Papanestis, M. Pappagallo, L. L. Pappalardo, C. Pappenheimer, C. Parkes, D. Parmar, B. Passalacqua, G. Passaleva, D. Passaro, A. Pastore, M. Patel, J. Patoc, C. Patrignani, A. Paul, C. J. Pawley, A. Pellegrino, J. Peng, M. Pepe Altarelli, S. Perazzini, D. Pereima, H. Pereira Da Costa, A. Pereiro Castro, P. Perret, A. Perrevoort, A. Perro, M. J. Peters, K. Petridis, A. Petrolini, J. P. Pfaller, H. Pham, L. Pica, M. Piccini, L. Piccolo, B. Pietrzyk, G. Pietrzyk, R. N. Pilato, D. Pinci, F. Pisani, M. Pizzichemi, V. Placinta, M. Plo Casasus, T. Poeschl, F. Polci, M. Poli Lener, A. Poluektov, N. Polukhina, I. Polyakov, E. Polycarpo, S. Ponce, D. Popov, S. Poslavskii, K. Prasanth, C. Prouve, D. Provenzano, V. Pugatch, G. Punzi, S. Qasim, Q. Q. Qian, W. Qian, N. Qin, S. Qu, R. Quagliani, R. I. Rabadan Trejo, J. H. Rademacker, M. Rama, M. Ramírez García, V. Ramos De Oliveira, M. Ramos Pernas, M. S. Rangel, F. Ratnikov, G. Raven, M. Rebollo De Miguel, F. Redi, J. Reich, F. Reiss, Z. Ren, P. K. Resmi, M. Ribalda Galvez, R. Ribatti, G. Ricart, D. Riccardi, S. Ricciardi, K. Richardson, M. Richardson-Slipper, K. Rinnert, P. Robbe, G. Robertson, E. Rodrigues, A. Rodriguez Alvarez, E. Rodriguez Fernandez, J. A. Rodriguez Lopez, E. Rodriguez Rodriguez, J. Roensch, A. Rogachev, A. Rogovskiy, D. L. Rolf, P. Roloff, V. Romanovskiy, A. Romero Vidal, G. Romolini, F. Ronchetti, T. Rong, M. Rotondo, S. R. Roy, M. S. Rudolph, M. Ruiz

Diaz, R. A. Ruiz Fernandez, J. Ruiz Vidal, J. Ryzka, J. J. Saavedra-Arias, J. J. Saborido Silva, R. Sadek, N. Sagidova, D. Sahoo, N. Sahoo, B. Saitta, M. Salomoni, I. Sanderswood, R. Santacesaria, C. Santamarina Rios, M. Santimaria, L. Santoro, E. Santovetti, A. Saputi, D. Saranin, A. Sarnatskiy, G. Sarpis, M. Sarpis, C. Satriano, A. Satta, D. Savrina, H. Sazak, F. Sborzacchi, A. Scarabotto, S. Schael, S. Scherl, M. Schiller, H. Schindler, M. Schmelling, B. Schmidt, S. Schmitt, H. Schmitz, O. Schneider, A. Schopper, N. Schulte, S. Schulte, M. H. Schune, G. Schwering, B. Sciascia, A. Sciuccati, I. Segal, S. Sellam, A. Semennikov, T. Senger, M. Senghi Soares, A. Sergi, N. Serra, L. Sestini, A. Seuthe, Y. Shang, D. M. Shangase, M. Shapkin, R. S. Sharma, I. Shchemerov, L. Shchutska, T. Shears, L. Shekhtman, Z. Shen, S. Sheng, V. Shevchenko, B. Shi, Q. Shi, Y. Shimizu, E. Shmanin, R. Shorkin, J. D. Shupperd, R. Silva Coutinho, G. Simi, S. Simone, M. Singha, N. Skidmore, T. Skwarnicki, M. W. Slater, E. Smith, K. Smith, M. Smith, A. Snoch, L. Soares Lavra, M. D. Sokoloff, F. J. P. Soler, A. Solomin, A. Solovev, I. Solovyev, N. S. Sommerfeld, R. Song, Y. Song, Y. Song, Y. S. Song, F. L. Souza De Almeida, B. Souza De Paula, E. Spadaro Norella, E. Spedicato, J. G. Speer, E. Spiridenkov, P. Spradlin, V. Sriskaran, F. Stagni, M. Stahl, S. Stahl, S. Stanislaus, M. Stefaniak, E. N. Stein, O. Steinkamp, O. Stenyakin, H. Stevens, D. Strekalina, Y. Su, F. Suljik, J. Sun, L. Sun, D. Sundfeld, W. Sutcliffe, K. Swientek, F. Swystun, A. Szabelski, T. Szumlak, Y. Tan, Y. Tang, M. D. Tat, A. Terentev, F. Terzuoli, F. Teubert, E. Thomas, D. J. D. Thompson, H. Tilquin, V. Tisserand, S. T'Jampens, M. Tobin, L. Tomassetti, G. Tonani, X. Tong, T. Tork, D. Torres Machado, L. Toscano, D. Y. Tou, C. Trippl, G. Tuci, N. Tuning, L. H. Uecker, A. Ukleja, D. J. Unverzagt, A. Upadhyay, B. Urbach, A. Usachov, A. Ustyuzhanin, U. Uwer, V. Vagnoni, V. Valcarce Cadenas, G. Valenti, N. Valls Canudas, J. van Eldik, H. Van Hecke, E. van Herwijnen, C. B. Van Hulse, R. Van Laak, M. van Veghel, G. Vasquez, R. Vazquez Gomez, P. Vazquez Regueiro, C. Vázquez Sierra, S. Vecchi, J. J. Velthuis, M. Veltri, A. Venkateswaran, M. Verdoglia, M. Vesterinen, D. Vico Benet, P. Vidrier Villalba, M. Vieites Diaz, X. Vilasis-Cardona, E. Vilella Figueras, A. Villa, P. Vincent, B. Vivacqua, F. C. Volle, D. vom Bruch, N. Voropaev, K. Vos, C. Vrahas, J. Wagner, J. Walsh, E. J. Walton, G. Wan, A. Wang, C. Wang, G. Wang, H. Wang, J. Wang, J. Wang, J. Wang, J. Wang, M. Wang, N. W. Wang, R. Wang, X. Wang, X. Wang, X. W. Wang, Y. Wang, Y. W. Wang, Z. Wang, Z. Wang, Z. Wang, J. A. Ward, M. Waterlaat, N. K. Watson, D. Websdale, Y. Wei, J. Wendel, B. D. C. Westhenry, C. White, M. Whitehead, E. Whiter, A. R. Wiederhold, D. Wiedner, G. Wilkinson, M. K. Wilkinson, M. Williams, M. J. Williams, M. R. J. Williams, R. Williams, Z. Williams, F. F. Wilson, M. Winn, W. Wislicki, M. Witek, L. Witola, G. Wormser, S. A. Wotton, H. Wu, J. Wu, X. Wu, Y. Wu, Z. Wu, K. Wyllie, S. Xian, Z. Xiang, Y. Xie, T. X. Xing, A. Xu, L. Xu, L. Xu, M. Xu, Z. Xu, Z. Xu, Z. Xu, K. Yang, S. Yang, X. Yang, Y. Yang, Z. Yang, V. Yeroshenko, H. Yeung, H. Yin, X. Yin, C. Y. Yu, J. Yu, X. Yuan, Y Yuan, E. Zaffaroni, M. Zavertyaev, M. Zdybal, F. Zenesini, C. Zeng, M. Zeng, C. Zhang, D. Zhang, J. Zhang, L. Zhang, S. Zhang, S. Zhang, Y. Zhang, Y. Z. Zhang, Z. Zhang, Y. Zhao, A. Zhelezov, S. Z. Zheng, X. Z. Zheng, Y. Zheng, T. Zhou, X. Zhou, Y. Zhou, V. Zhovkovska, L. Z. Zhu, X. Zhu, X. Zhu, V. Zhukov, J. Zhuo, Q. Zou, D. Zuliani, and G. Zunica. Observation of charge-parity symmetry breaking in baryon decays, 2025.

[6] C. Alanzeau, M.-E. Angoletta, J. Baillie, D. Barna, W. Bartmann, P. Belochitskii, J. Borburgh, H. Breuker, F. Butin, M. Buzio, O. Capatina, C. Carli, E. Carlier, M. Cattin, T. Dobers, P. Chiggiato, L. Ducimetiere, T. Eriksson, S. Fedemann, T. Fowler, R. Froeschl, R. Gebel, N. Gilbert, S. Hancock, J. Harasimowicz, M. Hori, L. V. Jorgensen, R. Kersevan, D. Kuchler, J.-M. Lacroix, G. LeGodec, P. Lelong, L. Lopez-Hernandez,

S. Maury, J. Molendijk, B. Morand, A. Newborough, D. Nisbet, A. Nosych, W. Oelert, M. Paoluzzi, S. Pasinelli, F. Pedersen, D. Perini, B. Puccio, J. Sanchez-Quesada, D. Schoerling, L. Sermeus, L. Soby, M. Timmins, D. Tommasini, G. Tranquille, G. Vanbavinckhove, A. Vorozhtsov, C. Welsch, and T. Zickler. Extra low energy antiproton (elena) ring and its transfer lines - design report. *CERN*, 2014. `https://cds.cern.ch/record/1694484/files/CERN-2014-002.pdf`.

[7] S. Sellner, Matthias Borchert, James Harrington, T. Higuchi, Hiroki Nagahama, Toshihiro Tanaka, A. Mooser, G. Schneider, Matthew Bohman, K. Blaum, Y. Matsuda, C. Ospelkaus, Wolfgang Quint, J. Walz, Yasunori Yamazaki, and Stefan Ulmer. A parts-per-billion measurement of the antiproton magnetic moment. *Nature*, 550:371–374, 10 2017.

[8] C. Smorra, S. Sellner, M. J. Borchert, J. A. Harrington, T. Higuchi, H. Nagahama, T. Tanaka, A. Mooser, G. Schneider, M. Bohman, K. Blaum, Y. Matsuda, C. Ospelkaus, W. Quint, J. Walz, Y. Yamazaki, and S. Ulmer. A parts-per-billion measurement of the antiproton magnetic moment. *Nature*, 550(7676):371–374, Oct 2017.

[9] C. J. Baker, W. Bertsche, A. Capra, C. Carruth, C. L. Cesar, M. Charlton, A. Christensen, R. Collister, A. Cridland Mathad, S. Eriksson, A. Evans, N. Evetts, J. Fajans, T. Friesen, M. C. Fujiwara, D. R. Gill, P. Grandemange, P. Granum, J. S. Hangst, W. N. Hardy, M. E. Hayden, D. Hodgkinson, E. Hunter, C. A. Isaac, M. A. Johnson, J. M. Jones, S. A. Jones, S. Jonsell, A. Khramov, L. Kurchaninov, N. Madsen, D. Maxwell, J. T. K. McKenna, S. Menary, T. Momose, P. S. Mullan, J. J. Munich, K. Olchanski, A. Olin, J. Peszka, A. Powell, P. Pusa, C. Ø. Rasmussen, F. Robicheaux, R. L. Sacramento, M. Sameed, E. Sarid, D. M. Silveira, C. So, G. Stutter, T. D. Tharp, R. I. Thompson, D. P. van der Werf, J. S. Wurtele, and G. M. Shore. Precision spectroscopy of the hyperfine components of the 1s-2s transition in antihydrogen. *Nature Physics*, 21(2):201–207, 2025.

[10] E. K. Anderson, C. J. Baker, W. Bertsche, N. M. Bhatt, G. Bonomi, A. Capra, I. Carli, C. L. Cesar, M. Charlton, A. Christensen, R. Collister, A. Cridland Mathad, D. Duque Quiceno, S. Eriksson, A. Evans, N. Evetts, S. Fabbri, J. Fajans, A. Ferwerda, T. Friesen, M. C. Fujiwara, D. R. Gill, L. M. Golino, M. B. Gomes Gonçalves, P. Grandemange, P. Granum, J. S. Hangst, M. E. Hayden, D. Hodgkinson, E. D. Hunter, C. A. Isaac, A. J. U. Jimenez, M. A. Johnson, J. M. Jones, S. A. Jones, S. Jonsell, A. Khramov, N. Madsen, L. Martin, N. Massacret, D. Maxwell, J. T. K. McKenna, S. Menary, T. Momose, M. Mostamand, P. S. Mullan, J. Nauta, K. Olchanski, A. N. Oliveira, J. Peszka, A. Powell, C. Ø. Rasmussen, F. Robicheaux, R. L. Sacramento, M. Sameed, E. Sarid, J. Schoonwater, D. M. Silveira, J. Singh, G. Smith, C. So, S. Stracka, G. Stutter, T. D. Tharp, K. A. Thompson, R. I. Thompson, E. Thorpe-Woods, C. Torkzaban, M. Urioni, P. Woosaree, and J. S. Wurtele. Observation of the effect of gravity on the motion of antimatter. *Nature*, 621(7980):716–722, 2023.

[11] Masaki Hori, Hossein Aghai-Khozani, Anna Sótér, Daniel Barna, Andreas Dax, Ryugo Hayano, Takumi Kobayashi, Yohei Murakami, Koichi Todoroki, Hiroyuki Yamada, Dezső Horváth, and Luca Venturelli. Buffer-gas cooling of antiprotonic helium to 1.5 to 1.7 k, and antiproton-to–electron mass ratio. *Science*, 354(6312):610–614, 2016.

[12] P. Adrich, P. Blumer, G. Caratsch, M. Chung, P. Cladé, P. Comini, P. Crivelli, O. Dalkarov, P. Debu, A. Douillet, D. Drapier, P. Froelich, N. Garroum, S. Guellati-Khelifa, J. Guyomard, P.-A. Hervieux, L. Hilico, P. Indelicato, S. Jonsell, J.-P. Karr, B. Kim, S. Kim, E.-S. Kim,

Y. J. Ko, T. Kosinski, N. Kuroda, B. M. Latacz, B. Lee, H. Lee, J. Lee, E. Lim, L. Liszkay, D. Lunney, G. Manfredi, B. Mansoulié, M. Matusiak, V. Nesvizhevsky, F. Nez, S. Niang, B. Ohayon, K. Park, N. Paul, P. Pérez, C. Regenfus, S. Reynaud, C. Roumegou, J.-Y. Roussé, Y. Sacquin, G. Sadowski, J. Sarkisyan, M. Sato, F. Schmidt-Kaler, M. Staszczak, K. Szymczyk, T. A. Tanaka, B. Tuchming, B. Vallage, A. Voronin, D. P. van der Werf, A. Welker, D. Won, S. Wronka, Y. Yamazaki, K.-H. Yoo, and P. Yzombard. Production of antihydrogen atoms by 6 kev antiprotons through a positronium cloud. *The European Physical Journal C*, 83(11):1004, 2023.

[13] S. Aghion, O. Ahlén, C. Amsler, A. Ariga, T. Ariga, A. S. Belov, K. Berggren, G. Bonomi, P. Bräunig, J. Bremer, R. S. Brusa, L. Cabaret, C. Canali, R. Caravita, F. Castelli, G. Cerchiari, S. Cialdi, D. Comparat, G. Consolati, H. Derking, S. Di Domizio, L. Di Noto, M. Doser, A. Dudarev, A. Ereditato, R. Ferragut, A. Fontana, P. Genova, M. Giammarchi, A. Gligorova, S. N. Gninenko, S. Haider, T. Huse, E. Jordan, L. V. Jørgensen, T. Kaltenbacher, J. Kawada, A. Kellerbauer, M. Kimura, A. Knecht, D. Krasnický, V. Lagomarsino, S. Lehner, A. Magnani, C. Malbrunot, S. Mariazzi, V. A. Matveev, F. Moia, G. Nebbia, P. Nédélec, M. K. Oberthaler, N. Pacifico, V. Petràček, C. Pistillo, F. Prelz, M. Prevedelli, C. Regenfus, C. Riccardi, O. Røhne, A. Rotondi, H. Sandaker, P. Scampoli, J. Storey, M.A. Subieta Vasquez, M. Špaček, G. Testera, R. Vaccarone, E. Widmann, S. Zavatarelli, and J. Zmeskal. A moiré deflectometer for antimatter. *Nature Communications*, 5(1):4538, Jul 2014.

[14] S. Aghion, C. Amsler, A. Ariga, T. Ariga, G. Bonomi, P. Bräunig, J. Bremer, R. S. Brusa, L. Cabaret, M. Caccia, R. Caravita, F. Castelli, G. Cerchiari, K. Chlouba, S. Cialdi, D. Comparat, G. Consolati, A. Demetrio, L. Di Noto, M. Doser, A. Dudarev, A. Ereditato, C. Evans, R. Ferragut, J. Fesel, A. Fontana, O. K. Forslund, S. Gerber, M. Giammarchi, A. Gligorova, S. Gninenko, F. Guatieri, S. Haider, H. Holmestad, T. Huse, I. L. Jernelv, E. Jordan, A. Kellerbauer, M. Kimura, T. Koettig, D. Krasnicky, V. Lagomarsino, P. Lansonneur, P. Lebrun, S. Lehner, J. Liberadzka, C. Malbrunot, S. Mariazzi, L. Marx, V. Matveev, Z. Mazzotta, G. Nebbia, P. Nedelec, M. Oberthaler, N. Pacifico, D. Pagano, L. Penasa, V. Petracek, C. Pistillo, F. Prelz, M. Prevedelli, L. Ravelli, L. Resch, B. Rienäcker, O. M. Røhne, A. Rotondi, M. Sacerdoti, H. Sandaker, R. Santoro, P. Scampoli, L. Smestad, F. Sorrentino, M. Spacek, J. Storey, I. M. Strojek, G. Testera, I. Tietje, S. Vamosi, E. Widmann, P. Yzombard, J. Zmeskal, and N. Zurlo. Laser excitation of the $n = 3$ level of positronium for antihydrogen production. *Phys. Rev. A*, 94(1):012507, Jul 2016.

[15] L. T. Glöggler, N. Gusakova, B. Rienäcker, A. Camper, R. Caravita, S. Huck, M. Volponi, T. Wolz, L. Penasa, V. Krumins, F. P. Gustafsson, D. Comparat, M. Auzins, B. Bergmann, P. Burian, R. S. Brusa, F. Castelli, G. Cerchiari, R. Ciuryło, G. Consolati, M. Doser, Ł. Graczykowski, M. Grosbart, F. Guatieri, S. Haider, M. A. Janik, G. Kasprowicz, G. Khatri, Ł. Kłosowski, G. Kornakov, L. Lappo, A. Linek, J. Malamant, S. Mariazzi, V. Petracek, M. Piwiński, S. Pospíšil, L. Povolo, F. Prelz, S. A. Rangwala, T. Rauschendorfer, B. S. Rawat, V. Rodin, O. M. Røhne, H. Sandaker, P. Smolyanskiy, T. Sowiński, D. Tefelski, T. Vafeiadis, C. P. Welsch, M. Zawada, J. Zielinski, and N. Zurlo. Positronium laser cooling via the $1^3s{-}2^3p$ transition with a broadband laser pulse. *Phys. Rev. Lett.*, 132:083402, Feb 2024.

[16] Claude Amsler, Massimiliano Antonello, Alexander Belov, Germano Bonomi, Roberto Sennen Brusa, Massimo Caccia, Antoine Camper, Ruggero Caravita, Fabrizio Castelli, Patrick

Cheinet, Daniel Comparat, Giovanni Consolati, Andrea Demetrio, Lea Di Noto, Michael Doser, Mattia Fanì, Rafael Ferragut, Julian Fesel, Sebastian Gerber, Marco Giammarchi, Angela Gligorova, Lisa Theresa Glöggler, Francesco Guatieri, Stefan Haider, Alexander Hinterberger, Alban Kellerbauer, Olga Khalidova, Daniel Krasnický, Vittorio Lagomarsino, Chloé Malbrunot, Sebastiano Mariazzi, Viktor Matveev, Simon Müller, Giancarlo Nebbia, Patrick Nedelec, Lilian Nowak, Markus Oberthaler, Emmanuel Oswald, Davide Pagano, Luca Penasa, Vojtech Petracek, Luca Povolo, Francesco Prelz, Marco Prevedelli, Benjamin Rienäcker, Ole Røhne, Alberto Rotondi, Heidi Sandaker, Romualdo Santoro, Gemma Testera, Ingmari Tietje, Valerio Toso, Tim Wolz, Pauline Yzombard, Christian Zimmer, and Nicola Zurlo. Pulsed production of antihydrogen. *Comm. Phys.*, 4(1):19, 2021.

[17] C. Smorra, F. Abbass, D. Schweitzer, M. Bohman, J. D. Devine, Y. Dutheil, A. Hobl, B. Arndt, B. B. Bauer, J. A. Devlin, S. Erlewein, M. Fleck, J. I. Jäger, B. M. Latacz, P. Micke, M. Schiffelholz, G. Umbrazunas, M. Wiesinger, C. Will, E. Wursten, H. Yildiz, K. Blaum, Y. Matsuda, A. Mooser, C. Ospelkaus, W. Quint, A. Soter, J. Walz, Y. Yamazaki, and S. Ulmer. Base-step: A transportable antiproton reservoir for fundamental interaction studies. *Review of Scientific Instruments*, 94(11), November 2023.

[18] T Aumann, W Bartmann, O Boine-Frankenheim, A Bouvard, A Broche, F Butin, D Calvet, J Carbonell, P Chiggiato, H De Gersem, R De Oliveira, T Dobers, F Ehm, J Ferreira Somoza, J Fischer, M Fraser, E Friedrich, A Frotscher, M Gomez-Ramos, J L Grenard, A Hobl, G Hupin, A Husson, P Indelicato, K Johnston, C Klink, Y Kubota, R Lazauskas, S Malbrunot-Ettenauer, N Marsic, W F O Müller, S Naimi, N Nakatsuka, R Necca, D Neidherr, G Neyens, A Obertelli, Y Ono, S Pasinelli, N Paul, E C Pollacco, D Rossi, H Scheit, M Schlaich, A Schmidt, L Schweikhard, R Seki, S Sels, E Siesling, T Uesaka, M Vilén, M Wada, F Wienholtz, S Wycech, and S Zacarias. PUMA, antiProton unstable matter annihilation. *Eur. Phys. J. A*, 58(5):88, 2022.

[19] M. Leonhardt, D. Schweitzer, F. Abbass, K. K. Anjum, B. Arndt, S. Erlewein, S. Endoh, P. Geissler, T. Imamura, J. I. Jäger, B. M. Latacz, P. Micke, F. Voelksen, H. Yildiz, K. Blaum, J. A. Devlin, Y. Matsuda, C. Ospelkaus, W. Quint, A. Soter, J. Walz, Y. Yamazaki, S. Ulmer, and C. Smorra. Proton transport from the antimatter factory of cern. *Nature*, 641(8064):871–875, May 2025.

[20] M.A. Levine, R.E. Marrs, J.N. Bardsley, P. Beiersdorfer, C.L. Bennett, M.H. Chen, T. Cowan, D. Dietrich, J.R. Henderson, D.A. Knapp, A. Osterheld, B.M. Penetrante, M.B. Schneider, and J.H. Scofield. The use of an electron beam ion trap in the study of highly charged ions. *Nuclear Instruments and Methods in Physics Research Section B: Beam Interactions with Materials and Atoms*, 43(3):431–440, 1989.

[21] P. Micke, S. Kühn, L. Buchauer, J. R. Harries, T. M. Bücking, K. Blaum, A. Cieluch, A. Egl, D. Hollain, S. Kraemer, T. Pfeifer, P. O. Schmidt, R. X. Schüssler, Ch. Schweiger, T. Stöhlker, S. Sturm, R. N. Wolf, S. Bernitt, and J. R. Crespo López-Urrutia. The Heidelberg compact electron beam ion traps. *Review of Scientific Instruments*, 89(6):063109, 06 2018.

[22] Markus Steck and Yuri A. Litvinov. Heavy-ion storage rings and their use in precision experiments with highly charged ions. *Progress in Particle and Nuclear Physics*, 115:103811, 2020.

[23] Sara Alfaro, Lorenz Panzl, Jakub Zieliński, Sankarshan Choudapurkar, Fredrik Parnefjord Gustafsson, Matthias Germann, Tommaso Faorlin, Yannick Weiser, Thomas Lafenthaler,

Thomas Monz, Michael Doser, Georgy Kornakov, and Giovanni Cerchiari. Highly charged isomeric qubits from antiproton annihilation, 2025.

[24] J R Crespo López-Urrutia. Frequency metrology using highly charged ions. *Journal of Physics: Conference Series*, 723(1):012052, jun 2016.

[25] V. M. Shabaev, A. I. Bondarev, D. A. Glazov, M. Y. Kaygorodov, Y. S. Kozhedub, I. A. Maltsev, A. V. Malyshev, R. V. Popov, I. I. Tupitsyn, and N. A. Zubova. Stringent tests of qed using highly charged ions. *Hyperfine Interactions*, 239(1):60, 2018.

[26] J. Morgner, B. Tu, C. M. König, T. Sailer, F. Heiße, H. Bekker, B. Sikora, C. Lyu, V. A. Yerokhin, Z. Harman, J. R. Crespo López-Urrutia, C. H. Keitel, S. Sturm, and K. Blaum. Stringent test of qed with hydrogen-like tin. *Nature*, 622(7981):53–57, 2023.

[27] Mandrita Mukherjee, Dietrich Beck, K Blaum, G Bollen, Jens Dilling, Sserunjaba George, Frank Herfurth, Alexander Herlert, A. Kellerbauer, H Kluge, S. Schwarz, Lutz Schweikhard, and C. Yazidjian. Isoltrap: An on-line penning trap for mass spectrometry on short-lived nuclides. *http://dx.doi.org/10.1140/epja/i2007-10528-9*, 35, 02 2008.

[28] Colin D. Bruzewicz, John Chiaverini, Robert McConnell, and Jeremy M. Sage. Trapped-ion quantum computing: Progress and challenges. *Applied Physics Reviews*, 6(2), May 2019.

[29] Martez Ahmadi, B. Alves, C. Baker, William Bertsche, A. Capra, Celeste Carruth, C. Cesar, M. Charlton, S. Cohen, R. Collister, S. Eriksson, Andrew Evans, Nathan Evetts, J. Fajans, T. Friesen, M. Fujiwara, David Gill, J. Hangst, W. Hardy, and J. Wurtele. Characterization of the 1s–2s transition in antihydrogen. *Nature*, 557, 05 2018.

[30] Nobel Prize Outreach. Nobel prize in physics 1989, 1989.

[31] Martina Knoop, Niels Madsen, and Richard Thompson. *Physics with Trapped Charged Particles*. 11 2013.

[32] Wolfgang Paul and Helmut Steinwedel. Ein neues massenspektrometer ohne magnetfeld. *Zeitschrift Naturforschung Teil A*, 8:448, 06 2014.

[33] D. Leibfried, R. Blatt, C. Monroe, and D. Wineland. Quantum dynamics of single trapped ions. *Reviews of Modern Physics*, 75, 05 2003.

[34] Elwin A. Dijck, Christian Warnecke, Malte Wehrheim, Ruben B. Henninger, Julia Eff, Kostas Georgiou, Andrea Graf, Stepan Kokh, Lakshmi P. Kozhiparambil Sajith, Christopher Mayo, Vera M. Schäfer, Claudia Volk, Piet O. Schmidt, Thomas Pfeifer, and José R. Crespo López-Urrutia. Sympathetically cooled highly charged ions in a radio-frequency trap with superconducting magnetic shielding. *Review of Scientific Instruments*, 94(8):083203, 08 2023.

[35] C. Amsler, H. Breuker, M. Bumbar, S. Chesnevskaya, G. Costantini, R. Ferragut, M. Giammarchi, A. Gligorova, G. Gosta, H. Higaki, M. Hori, E.D. Hunter, C. Killian, V. Kraxberger, N. Kuroda, A. Lanz, M. Leali, G. Maero, C. Malbrunot, V. Mascagna, Y. Matsuda, V. Mäckel, S. Migliorati, D.J. Murtagh, Y. Nagata, A. Nanda, L. Nowak, M. Romé, M.C. Simon, M. Tajima, V. Toso, S. Ulmer, L. Venturelli, A. Weiser, E. Widmann, and Y. Yamazaki. Injection and capture of antiprotons in a penning–malmberg trap using a drift tube accelerator and degrader foil. *Nuclear Instruments and Methods in*

Physics Research Section A: Accelerators, Spectrometers, Detectors and Associated Equipment, 1065:169529, 2024.

[36] K. Zimmermann, M. V. Okhapkin, O. A. Herrera-Sancho, and E. Peik. Laser ablation loading of a radiofrequency ion trap. *Applied Physics B*, 107(4):883–889, February 2012.

[37] H. Nägerl, Christian Roos, Harald Rohde, D. Leibfried, J. Eschner, Ferdinand Schmidt-Kaler, and R. Blatt. Addressing and cooling of single ions in paul traps. *Fortschritte Der Physik-progress of Physics - FORTSCHR PHYS*, 48:623–636, 05 2000.

[38] Joseph Ladislas Wiza. Microchannel plate detectors. *Nuclear Instruments and Methods*, 162(1):587–601, 1979.

[39] S O Flyckt and Carole Marmonier. *Photomultiplier tubes: principles and applications; 2nd ed.* Photonis, Brive, 2002.

[40] N. A. Tahir, R. Schmidt, A. Shutov, I. V. Lomonosov, A. R. Piriz, D. H. H. Hoffmann, C. Deutsch, and V. E. Fortov. Large hadron collider at cern: Beams generating high-energy-density matter. *Phys. Rev. E*, 79:046410, Apr 2009.

[41] Geoff Brumfiel. Physicists declare victory in higgs hunt. *Nature*, Jul 2012.

[42] Vogel M. Quint W., editor. *Fundamental Physics in Particle Traps.* Springer, 2014.

[43] D. M. C. M. K. Dissanayake, N. Wickramage, K. M. Liyanage, and K. A. S. Lakshan. Simulating negative hydrogen ion acceleration in linac-4 using unity 3d, 2025.

[44] M. Hori and J. Walz. Physics at cern's antiproton decelerator. *Progress in Particle and Nuclear Physics*, 72:206–253, September 2013.

[45] F. M. Huber, R. A. Lewis, E. W. Messerschmid, and G. A. Smith. Precision tests of einstein's weak equivalence principle for antimatter. *Advances in Space Research*, 25(6):1245–1249, Jan 2000.

[46] R Caravita. Progress report of the AEgIS experiment (2024). Technical report, CERN, Geneva, 2025.

[47] Andreas Knecht, S. Aghion, O. Ahlén, Claude Amsler, Akitaka Ariga, T. Ariga, A. Belov, Germano Bonomi, P. Bräunig, Johan Bremer, R.S. Brusa, L. Cabaret, Carlo Canali, Ruggero Caravita, Fabrizio Castelli, Giovanni Cerchiari, Simone Cialdi, Daniel Comparat, G. Consolati, and Johann Zmeskal. The aegis experiment: Measuring the gravitational interaction of antimatter. *Hyperfine Interactions*, 228:121–131, 10 2014.

[48] Stefano Aghion, Claude Amsler, Germano Bonomi, R.s Brusa, Massimo Caccia, Ruggero Caravita, Fabrizio Castelli, Giovanni Cerchiari, Daniel Comparat, G. Consolati, Andrea Demetrio, Lea Noto, Michael Doser, Craig Evans, Mattia Fanì, Rafael Ferragut, Julian Fesel, Andrea Fontana, Sebastian Gerber, and Massimiliano Antonello. Compression of a mixed antiproton and electron non-neutral plasma to high densities. *The European Physical Journal D*, 72, 04 2018.

[49] G. B. Andresen, M. D. Ashkezari, M. Baquero-Ruiz, W. Bertsche, P. D. Bowe, E. Butler, C. L. Cesar, S. Chapman, M. Charlton, A. Deller, S. Eriksson, J. Fajans, T. Friesen, M. C. Fujiwara, D. R. Gill, A. Gutierrez, J. S. Hangst, W. N. Hardy, M. E. Hayden, A. J.

Humphries, R. Hydomako, S. Jonsell, N. Madsen, S. Menary, P. Nolan, A. Olin, A. Povilus, P. Pusa, F. Robicheaux, E. Sarid, D. M. Silveira, C. So, J. W. Storey, R. I. Thompson, D. P. van der Werf, J. S. Wurtele, and Y. Yamazaki. Centrifugal separation and equilibration dynamics in an electron-antiproton plasma. *Phys. Rev. Lett.*, 106:145001, Apr 2011.

[50] G. Gabrielse, W. S. Kolthammer, R. McConnell, P. Richerme, J. Wrubel, R. Kalra, E. Novitski, D. Grzonka, W. Oelert, T. Sefzick, M. Zielinski, J. S. Borbely, D. Fitzakerley, M. C. George, E. A. Hessels, C. H. Storry, M. Weel, A. Müllers, J. Walz, and A. Speck. Centrifugal separation of antiprotons and electrons. *Phys. Rev. Lett.*, 105:213002, Nov 2010.

[51] Michael Berghold, Davide Orsucci, Francesco Guatieri, Sara Alfaro, Marcis Auzins, Benedikt Bergmann, Petr Burian, Roberto Sennen Brusa, Antoine Camper, Ruggero Caravita, Fabrizio Castelli, Giovanni Cerchiari, Roman Jerzy Ciuryło, Ahmad Chehaimi, Giovanni Consolati, Michael Doser, Kamil Eliaszuk, Riley Craig Ferguson, Matthias Germann, Anna Giszczak, Lisa Glöggler, Łukasz Graczykowski, Malgorzata Grosbart, Natali Gusakova, Fredrik Gustafsson, Stefan Haider, Saiva Huck, Christoph Hugenschmidt, Malgorzata Anna Janik, Tymoteusz Henryk Januszek, Grzegorz Kasprowicz, Kamila Kempny, Ghanshyambhai Khatri, Łukasz Kłosowski, Georgy Kornakov, Valts Krumins, Lidia Lappo, Adam Linek, Sebastiano Mariazzi, Pawel Moskal, Dorota Nowicka, Piyush Pandey, Daniel PĘcak, Luca Penasa, Vojtech Petracek, Mariusz Piwiński, Stanislav Pospisil, Luca Povolo, Francesco Prelz, Sadiqali Rangwala, Tassilo Rauschendorfer, Bharat Rawat, Benjamin Rienäcker, Volodymyr Rodin, Ole Røhne, Heidi Sandaker, Sushil Sharma, Petr Smolyanskiy, Tomasz Sowiński, Dariusz Tefelski, Theodoros Vafeiadis, Marco Volponi, Carsten Peter Welsch, Michal Zawada, Jakub Zielinski, Nicola Zurlo, and AEḡIS Collaboration. Real-time antiproton annihilation vertexing with submicrometer resolution. *Science Advances*, 11(14):eads1176, 2025.

[52] David L. Morgan and Vernon W. Hughes. Atomic processes involved in matter-antimatter annihilation. *Phys. Rev. D*, 2:1389–1399, Oct 1970.

[53] Wendell Hill and Chi Lee. Light-matter interaction: Atoms and molecules in external fields and nonlinear optics. *Light-Matter Interaction: Atoms and Molecules in External Fields and Nonlinear Optics*, 01 2007.

[54] V. M. Shabaev, A. I. Bondarev, D. A. Glazov, M. Y. Kaygorodov, Y. S. Kozhedub, I. A. Maltsev, A. V. Malyshev, R. V. Popov, I. I. Tupitsyn, and N. A. Zubova. Stringent tests of qed using highly charged ions. *Hyperfine Interactions*, 239(1), November 2018.

[55] V M Shabaev. Hyperfine structure of hydrogen-like ions. *J. Phys. B*, 27(24):5825, dec 1994.

[56] P Indelicato. Qed tests with highly charged ions. *Journal of Physics B: Atomic, Molecular and Optical Physics*, 52(23):232001, November 2019.

[57] Roland B. Lumpay, Jade C. Jusoy, Ruel Apas, and Eulogio Auxtero Jr. The proton radius puzzle and discrepancies in proton structure measurements, 2025.

[58] Markus Steck and Yuri A. Litvinov. Heavy-ion storage rings and their use in precision experiments with highly charged ions. *Progress in Particle and Nuclear Physics*, 115:103811, November 2020.

[59] Bernhard Franzke. The heavy ion storage and cooler ring project esr at gsi. *Nuclear Instruments and Methods in Physics Research Section B: Beam Interactions with Materials and Atoms*, 24-25:18–25, 1987.

[60] R. von Hahn, A. Becker, F. Berg, K. Blaum, C. Breitenfeldt, H. Fadil, F. Fellenberger, M. Froese, S. George, J. Göck, M. Grieser, F. Grussie, E. A. Guerin, O. Heber, P. Herwig, J. Karthein, C. Krantz, H. Kreckel, M. Lange, F. Laux, S. Lohmann, S. Menk, C. Meyer, P. M. Mishra, O. Novotný, A. P. O'Connor, D. A. Orlov, M. L. Rappaport, R. Repnow, S. Saurabh, S. Schippers, C. D. Schröter, D. Schwalm, L. Schweikhard, T. Sieber, A. Shornikov, K. Spruck, S. Sunil Kumar, J. Ullrich, X. Urbain, S. Vogel, P. Wilhelm, A. Wolf, and D. Zajfman. The cryogenic storage ring csr. *Review of Scientific Instruments*, 87(6):063115, 06 2016.

[61] M.A. Levine, R.E. Marrs, J.N. Bardsley, P. Beiersdorfer, C.L. Bennett, M.H. Chen, T. Cowan, D. Dietrich, J.R. Henderson, D.A. Knapp, A. Osterheld, B.M. Penetrante, M.B. Schneider, and J.H. Scofield. The use of an electron beam ion trap in the study of highly charged ions. *Nuclear Instruments and Methods in Physics Research Section B: Beam Interactions with Materials and Atoms*, 43(3):431–440, 1989.

[62] T. Yamazaki, N. Morita, R. S. Hayano, E. Widmann, and J. Eades. Antiprotonic helium. *Phys. Rep.*, 366(4):183 – 329, 2002.

[63] D. Gotta, K. Rashid, B. Fricke, P. Indelicato, and L. M. Simons. X-ray transitions from antiprotonic noble gases. *The European Physical Journal D*, 47(1):11–26, February 2008.

[64] V. M. Shabaev, M. B. Shabaeva, and I. I. Tupitsyn. Hyperfine structure of hydrogenlike and lithiumlike atoms. *Phys. Rev. A*, 52:3686–3690, Nov 1995.

[65] T.J. Mertzimekis, K. Stamou, and A. Psaltis. An online database of nuclear electromagnetic moments. *Nucl. Instrum. Methods Phys. Res. A*, 807:56–60, 2016.

[66] Raymond A. Serway. *Physics for scientists & engineers with modern physics.* Second edition. Philadelphia : Saunders College Pub., 1986, c1983., 1986, c1983. Previously published in 1986 as separate vols. with titles: Physics for scientists & engineers and Physics for scientists & engineers with modern physics.;Text on lining papers.;Includes bibliographical references and index.

[67] S. Agostinelli, J. Allison, K. Amako, J. Apostolakis, H. Araujo, P. Arce, M. Asai, D. Axen, S. Banerjee, G. Barrand, F. Behner, L. Bellagamba, J. Boudreau, L. Broglia, A. Brunengo, H. Burkhardt, S. Chauvie, J. Chuma, R. Chytracek, G. Cooperman, G. Cosmo, P. Degtyarenko, A. Dell'Acqua, G. Depaola, D. Dietrich, R. Enami, A. Feliciello, C. Ferguson, H. Fesefeldt, G. Folger, F. Foppiano, A. Forti, S. Garelli, S. Giani, R. Giannitrapani, D. Gibin, J.J. Gómez Cadenas, I. González, G. Gracia Abril, G. Greeniaus, W. Greiner, V. Grichine, A. Grossheim, S. Guatelli, P. Gumplinger, R. Hamatsu, K. Hashimoto, H. Hasui, A. Heikkinen, A. Howard, V. Ivanchenko, A. Johnson, F.W. Jones, J. Kallenbach, N. Kanaya, M. Kawabata, Y. Kawabata, M. Kawaguti, S. Kelner, P. Kent, A. Kimura, T. Kodama, R. Kokoulin, M. Kossov, H. Kurashige, E. Lamanna, T. Lampén, V. Lara, V. Lefebure, F. Lei, M. Liendl, W. Lockman, F. Longo, S. Magni, M. Maire, E. Medernach, K. Minamimoto, P. Mora de Freitas, Y. Morita, K. Murakami, M. Nagamatu, R. Nartallo, P. Nieminen, T. Nishimura, K. Ohtsubo, M. Okamura, S. O'Neale, Y. Oohata, K. Paech, J. Perl, A. Pfeiffer, M.G. Pia, F. Ranjard, A. Rybin, S. Sadilov, E. Di Salvo, G. Santin, T. Sasaki, N. Savvas, Y. Sawada, S. Scherer, S. Sei, V. Sirotenko, D. Smith, N. Starkov, H. Stoecker, J. Sulkimo, M. Takahata, S. Tanaka, E. Tcherniaev, E. Safai Tehrani, M. Tropeano, P. Truscott, H. Uno, L. Urban, P. Urban, M. Verderi, A. Walkden, W. Wander,

H. Weber, J.P. Wellisch, T. Wenaus, D.C. Williams, D. Wright, T. Yamada, H. Yoshida, and D. Zschiesche. Geant4—a simulation toolkit. *Nucl. Instrum. Methods Phys. Res. A*, 506(3):250–303, July 2003.

[68] J. Allison, K. Amako, J. Apostolakis, H. Araujo, P. Arce Dubois, M. Asai, G. Barrand, R. Capra, S. Chauvie, R. Chytracek, G. A. P. Cirrone, G. Cooperman, G. Cosmo, G. Cuttone, G. G. Daquino, M. Donszelmann, M. Dressel, G. Folger, F. Foppiano, J. Generowicz, V. Grichine, S. Guatelli, P. Gumplinger, A. Heikkinen, I. Hrivnacova, A. Howard, S. Incerti, V. Ivanchenko, T. Johnson, F. Jones, T. Koi, R. Kokoulin, M. Kossov, H. Kurashige, V. Lara, S. Larsson, F. Lei, O. Link, F. Longo, M. Maire, A. Mantero, B. Mascialino, I. McLaren, P. Mendez Lorenzo, K. Minamimoto, K. Murakami, P. Nieminen, L. Pandola, S. Parlati, L. Peralta, J. Perl, A. Pfeiffer, M. G. Pia, A. Ribon, P. Rodrigues, G. Russo, S. Sadilov, G. Santin, T. Sasaki, D. Smith, N. Starkov, S. Tanaka, E. Tcherniaev, B. Tome, A. Trindade, P. Truscott, L. Urban, M. Verderi, A. Walkden, J. P. Wellisch, D. C. Williams, D. Wright, and H. Yoshida. Geant4 developments and applications. *IEEE Trans. Nucl. Sci.*, 53(1):270–278, February 2006.

[69] J. Allison, K. Amako, J. Apostolakis, P. Arce, M. Asai, T. Aso, E. Bagli, A. Bagulya, S. Banerjee, G. Barrand, B.R. Beck, A.G. Bogdanov, D. Brandt, J.M.C. Brown, H. Burkhardt, Ph. Canal, D. Cano-Ott, S. Chauvie, K. Cho, G.A.P. Cirrone, G. Cooperman, M.A. Cortés-Giraldo, G. Cosmo, G. Cuttone, G. Depaola, L. Desorgher, X. Dong, A. Dotti, V.D. Elvira, G. Folger, Z. Francis, A. Galoyan, L. Garnier, M. Gayer, K.L. Genser, V.M. Grichine, S. Guatelli, P. Guèye, P. Gumplinger, A.S. Howard, I. Hřivnáčová, S. Hwang, S. Incerti, A. Ivanchenko, V.N. Ivanchenko, F.W. Jones, S.Y. Jun, P. Kaitaniemi, N. Karakatsanis, M. Karamitros, M. Kelsey, A. Kimura, T. Koi, H. Kurashige, A. Lechner, S.B. Lee, F. Longo, M. Maire, D. Mancusi, A. Mantero, E. Mendoza, B. Morgan, K. Murakami, T. Nikitina, L. Pandola, P. Paprocki, J. Perl, I. Petrović, M.G. Pia, W. Pokorski, J.M. Quesada, M. Raine, M.A. Reis, A. Ribon, A. Ristić Fira, F. Romano, G. Russo, G. Santin, T. Sasaki, D. Sawkey, J.I. Shin, I.I. Strakovsky, A. Taborda, S. Tanaka, B. Tomé, T. Toshito, H.N. Tran, P.R. Truscott, L. Urban, V. Uzhinsky, J.M. Verbeke, M. Verderi, B.L. Wendt, H. Wenzel, D.H. Wright, D.M. Wright, T. Yamashita, J. Yarba, and H. Yoshida. Recent developments in Geant4. *Nucl. Instrum. Methods Phys. Res. A*, 835:186–225, November 2016.

[70] Jacek Bieroń, Charlotte Froese Fischer, and Per Jönsson. Editorial of the special issue "general relativistic atomic structure program—grasp". *Atoms*, 11(6), 2023.

[71] P. Jönsson, G. Gaigalas, J. Bieroń, C. Froese Fischer, and I.P. Grant. New version: Grasp2k relativistic atomic structure package. *Comput. Phys. Commun.*, 184(9):2197–2203, 2013.

[72] P. Jönsson, X. He, C. Froese Fischer, and I.P. Grant. The grasp2k relativistic atomic structure package. *Comput. Phys. Commun.*, 177(7):597–622, 2007.

[73] V. M. Shabaev, M. B. Shabaeva, I. I. Tupitsyn, V. A. Yerokhin, A. N. Artemyev, T. Kühl, M. Tomaselli, and O. M. Zherebtsov. Transition energy and lifetime for the ground-state hyperfine splitting of high-z lithiumlike ions. *Phys. Rev. A*, 57:149–156, Jan 1998.

[74] Pijushpani Bhattacharjee. Cosmic topological defects, highest energy cosmic rays, and the baryon asymmetry of the universe. *Physical Review Letters*, 81(2):260–263, July 1998.

[75] J. Pedregosa-Gutierrez, C. Champenois, Marie Houssin, and Martina Knoop. Anharmonic contributions in real rf linear quadrupole traps, 2010.

[76] James A. Fedchak, Julia K. Scherschligt, Sefer Avdiaj, Daniel S. Barker, Stephen P. Eckel, Ben Bowers, Scott O'Connell, and Perry Henderson. Outgassing rate comparison of seven geometrically similar vacuum chambers of different materials and heat treatments. *Journal of Vacuum Science amp; Technology B, Nanotechnology and Microelectronics: Materials, Processing, Measurement, and Phenomena*, 39(2), February 2021.

[77] European Commission. Common sides of euro coins — economy-finance.ec.europa.eu. `https://economy-finance.ec.europa.eu/euro/euro-coins-and-notes/euro-coins/common-sides-euro-coins_en`. [Accessed 18-07-2025].

[78] Red Pitaya. Red pitaya stemlab. `https://www.redpitaya.com`, 2024. Accessed: 2025-07-19.

[79] Robert L. Byer. Diode laser—pumped solid-state lasers. *Science*, 239(4841):742–747, 1988.

[80] D. A. Church and H. G. Dehmelt. Radiative cooling of an electrodynamically contained proton gas. *Journal of Applied Physics*, 40(9):3421–3424, 08 1969.

[81] G Cerchiari, S Erlewein, P Yzombard, M Zimmermann, and A Kellerbauer. Capture of an external anion beam into a linear paul trap. *Journal of Physics B: Atomic, Molecular and Optical Physics*, 52(15):155003, jul 2019.

[82] William R Leo. *Techniques for nuclear and particle physics experiments: a how-to approach; 2nd ed.* Springer, Berlin, 1994.

[83] Peter J. Mohr, Eite Tiesinga, David B. Newell, and Barry N. Taylor. Codata internationally recommended 2022 values of the fundamental physical constants, 2024-05-08 04:05:00 2024.

[84] Muhammad Raza, Faiz Ahmad, mohd afian Omar, and Ali Muhsan. Defect analysis of 316lss during the powder injection moulding process. *Defect and Diffusion Forum*, 329:35–43, 07 2012.

[85] Rende Steerenberg. Accelerator report: A well-deserved winter break for the accelerator complex, Dec 2024.

A. Extended Candidate Table

Table. A.1 presents an extension of the HCI candidate list from Table 3.1. Here, in between results for the correction factors of the hyperfine splitting wavelength results are shown.

Ion	I	μ/μ_N	A	$\delta \times 10^2$	$\epsilon \times 10^2$	λ_{HF}(µm)
$^{83}Kr^{35+}$	1/2-	0.5910	1.114708	0.8328	0.4939	19.42455
$^{85}Kr^{35+}$	1/2-	0.6320	1.114708	0.8328	0.4939	18.16442
$^{82}Rb^{36+}$	5-	1.5096	1.121909	0.8769	-0.6574	12.51460
$^{85}Sr^{37+}$	1/2-	0.5990	1.129399	0.9236	0.5423	16.10615
$^{87}Sr^{37+}$	1/2-	0.6240	1.129399	0.9236	0.5423	15.46087
$^{85}Y^{38+}$	9/2+	6.2000	1.137188	0.9742	0.2540	2.567061
$^{87}Y^{38+}$	9/2+	6.2400	1.137188	0.9742	0.2550	2.550630
$^{90}Y^{38+}$	7+	5.2800	1.137188	0.9742	0.2389	3.125522
$^{92}Nb^{40+}$	2+	6.1370	1.153701	1.0917	0.8096	1.968983
$^{93}Mo^{41+}$	21/2+	9.9300	1.162446	1.1587	0.4354	1.336406
$^{99}Rh^{44+}$	9/2+	5.6200	1.190779	1.3800	0.3219	1.769000
$^{101}Rh^{44+}$	9/2+	5.4300	1.190779	1.3800	0.3141	1.830757
$^{102}Rh^{44+}$	6+	4.0100	1.190779	1.3800	0.2122	2.540022
$^{106}Ag^{46+}$	6+	3.7040	1.211547	1.5364	0.1453	2.374345
$^{108}Ag^{46+}$	6+	3.5800	1.211547	1.5364	0.1055	2.455607
$^{110}Ag^{46+}$	6+	3.6020	1.211547	1.5364	0.1127	2.440786
$^{110}In^{48+}$	2+	4.3650	1.233957	1.7065	1.0757	1.529835
$^{114}In^{48+}$	5+	4.6460	1.233957	1.7065	0.5796	1.625155
$^{116}Sb^{50+}$	8-	2.5900	1.258147	1.9005	-1.0601	2.587845
$^{118}Sb^{50+}$	8-	2.3200	1.258147	1.9005	-1.3627	2.880392
$^{120}Sb^{50+}$	8-	2.3400	1.258147	1.9005	-1.3379	2.856473
$^{119}Te^{51+}$	11/2-	0.8940	1.270956	2.0077	0.6792	6.946341
$^{121}Te^{51+}$	11/2-	0.8950	1.270956	2.0077	0.6792	6.938580

Table A.1.: The hyperfine splitting wavelength λ_{HF} for ground-state hydrogen-like ion candidates with atomic numbers between Kr and Xe and a half-life above 60 minutes. Here A and δ are the relativistic and nuclear charge distribution correction factors given by Ref. [**?**]. The nuclear magnetization distribution (Bohr-Weisskopf) correction ϵ is given by Eq. 3.3. The calculations are conducted using the nuclear data provided in Ref. [**?**].